

**Numerical study of the liquid ligament formation
from a liquid layer by Faraday instability and
Rayleigh-Taylor instability**

Yikai LI

Doctoral Dissertation

**Numerical study of the liquid ligament formation
from a liquid layer by Faraday instability and
Rayleigh-Taylor instability**

by

Yikai LI

Submitted for the Degree of Doctor of Engineering

October 2014

Graduate School of Aerospace Engineering

Nagoya University

JAPAN

Abstract

In this dissertation, we numerically investigated the large surface deformation from a liquid layer due to the interfacial instabilities caused by the time-dependent and constant inertial forces, which are usually referred to as “Faraday instability” and “Rayleigh-Taylor (RT) instability”, respectively. These instabilities can form a liquid ligament (a large liquid surface deformation that results in disintegrated droplets having outward velocities), which is important for atomization because it is the transition phase to generate droplets. The objectives of this dissertation are to reveal the physics underlying the ligament formation due to the Faraday instability and the RT instability.

Previous investigations explained the mechanism of ligament formation due to the Faraday instability by only using the term “inertia” without detailed elucidation, which does not provide sufficient information on the physics underlying the ligament formation. Based on the numerical solutions of two-dimensional (2D) incompressible Euler equations for a prototype Faraday instability flow, we explored physically how each liquid ligament can be developed to be dynamically free from the motion of bottom substrate. According to the linear theory, the amplified crest, which results from the suction of liquid from the trough portion to the crest portion, is always pulled back to the liquid layer no matter how largely the surface deformation can be developed, and the dynamically freed ligament is never formed. Situation is changed when the nonlinear effect is considered. The impingement of the liquid flow from the trough portions arouses pressure enhancement at the high crest (ligament) root. This pressure enhancement has two major effects. The first one is lowering the capability of sucking liquid from the trough portion, which abates the increase of crest height compared to the linear theory. The second one is causing a local maximum pressure location at the crest root. Thus, the ligament above this location becomes dynamically free from the motion of bottom substrate in the laboratory reference frame. The liquid elements passing through the maximum pressure location elongate the dynamically freed liquid region and cause a slender ligament from the liquid layer.

For industrial application of Faraday instability, the threshold condition for the spray formation is of the main concern. Previous experimental studies on the

ultrasonic atomization have shown that, when spray forms, there exists a predominant surface wave mode from which the drops of the mean diameter following Lang's equation are generated. In this dissertation, we determined this predominant surface wave mode physically and studied the threshold condition for spray formation based on a cell model of the predominant surface wavelength that excludes the effects of the container walls. We defined the condition in which the broken drop holds a null area-averaged vertical velocity in the laboratory reference frame as the criterion for spray formation. The calculation results indicated that spray formation onsets in the sub-harmonic instability region, at a critical dimensionless forcing strength value $\beta_c \sim O(1)$, which is two orders larger than the previous experimental determined threshold condition for the rare drop ejection event. Spray formation due to the Faraday instability can be considered as a process that the liquid layer absorbs energy from the inertial force, and releases it by producing drops leaving the liquid layer. In this study, we demonstrated that for a deep liquid layer, the threshold condition for spray formation is determined only by the forcing strength, and does not depend on the initial liquid layer condition used in the calculations.

The RT instability can be deemed as a limit case of the Faraday instability under the condition that the forcing frequency approaches zero and the forcing displacement approaches infinity. In this case, the constant descent velocity of the trough surface leads to a steady liquid atomization rate. Analytical results revealed two key mechanisms underlying the steadiness: (1) the bulk liquid layer was dynamically freed from the long liquid ligament by the formation of a maximum pressure point at the ligament root, and (2) the inertial force was only effective at the ligament root region to drive outward the liquid concentrating from the trough portion. Analytical expressions were derived for characteristic surface deformation quantities. The velocity and width of the liquid entering the freed liquid ligament at the maximum pressure location mirrored those associated with a vertical jet emanating downwards from an orifice injector under gravity. Thus, the results from laboratory low-speed jet emanation experiments were useful to predict the disintegration behavior of a liquid ligament formed by an RT instability.

Acknowledgements

I feel so lucky and honored to start my academic career in the Aerospace Engineering department of Nagoya University. I have learnt a lot in the past four years. I want to show my sincere thanks to all people who kindly helped me to complete this dissertation.

First, my deepest gratitude is expressed to my supervisors, Prof. Jiro Kasahara and Prof. Akira Umemura, not only for their insightful guidance and enthusiastic encouragements on my doctoral research, but also for their kind assistances in my daily life. Their solid knowledge on fluid dynamics helped me to enhance the understanding on this classical physic field and improve my sense on science. Their rigorous attitude to the science will influence me in my following research career. I have learnt a lot from them on how to start and do a really meaningful scientific study. I also want to thank Associate Professor Hosei Nagano for his generous help in my academic career and daily life in Nagoya University. He gave me a lot of useful advises on the dissertation as a committee member. I also appreciate the constructive suggestions and comments from other two committee members, Professor Akihiro Sasoh and Professor Yasuhiko Sakai.

I also want to thank Dr. Junji Shinjo, who worked for JAXA, for very helpful discussion on the numerical methods on capturing the liquid-gas interface with him. His rich experiences and deep insight into the CLSVOF method greatly helped me to understand the essence of this complicated method and complete the numerical code that is utilized to study the detailed dynamics in this dissertation.

I would also like to express my sincere thanks to the China Scholarship Council (CSC) for their financial support.

Finally, I want to express my gratitude to my family, especially to my wife Yu Jiang. She cannot come to Japan to accompany me due to her work, but she always offers me confidence when I was frustrated by the bottleneck of the research. I may not complete my research without her constant support and encouragement. I also

want to thank my new-born son, who brings me a lot of fun and always reminds me of the responsibility as a father.

Contents

Abstract.....	I
Acknowledgements.....	III
Contents	V
Chapter 1 Introduction	1
1.1 Background	1
1.2 The objective of this research.....	4
1.3 The outline of this dissertation	4
Chapter 2 Literature review	6
2.1 Faraday instability	6
2.1.1 Linear theory of Faraday instability	6
2.1.2 Faraday standing wave patterns.....	7
2.1.3 Large surface deformation due to Faraday instability	8
2.2 Rayleigh-Taylor instability.....	12
Chapter 3 Numerical methods	16
3.1 Physical model	16
3.2 Numerical solver	22
3.2.1 Numerical methods for solving Euler equations	22
3.2.2 Coupled Volume-of-Fluid and Level-set method.....	24
Chapter 4 Mechanism of ligament formation by Faraday instability	34
4.1 Mathieu equation.....	34
4.2 Numerical validation	36
4.3 Dynamics of ligament formation.....	38
4.3.1 Results of the surface evolution.....	39
4.3.2 Destabilizing mechanism at the linear stage.....	41
4.3.3 Ligament structure.....	42
Chapter 5 Threshold condition for spray formation due to Faraday instability.....	57
5.1 Experimental implications.....	57

5.2 Numerical strategy	59
5.3 Threshold condition for spray formation.....	63
5.3.1 Non-atomization case	65
5.3.2 Atomization case	68
5.3.3 Near-critical case	74
5.3.4 Theoretical consideration	76
5.3.5 Three-dimensional modification.....	80
5.3.6 Interpretation of Lang's equation	81
5.4 Effects of the initial disturbance.....	82
Chapter 6 Dynamics of ligament formation due to RT instability.....	85
6.1 Numerical validation	85
6.2 Overall dynamics.....	86
6.3 Characteristic quantities associated with steady flow	91
6.3.1 Constant descending velocity of the trough surface V^*	91
6.3.2 Amplitude of the sinusoidal surface δ_0^*	97
6.3.3 Velocity v_3^* and liquid ligament width $2b^*$ at the maximum pressure location ..	100
6.4 Laboratory low-speed jet experiments bridged to the ligament disintegration due to RT instability	102
Chapter 7 Conclusion.....	104
Reference	107
List of publications	112

Chapter 1

Introduction

1.1 Background

Liquid atomization plays an important role in a wide range of industrial applications. For example, in an automotive engine, especially a diesel engine, the combustion efficiency and emission quality are highly dependent on the fuel spray and atomization characteristics. Other fields where liquid atomization is applied include pharmaceutical emulsification, encapsulation, and ink-jet printing.

Enormous techniques have been used to realize liquid atomization. One practical method is subjecting a body of liquid to a vertical vibration (with displacement $\Delta = \Delta_0 \sin(\Omega t)$, where Δ_0 is the amplitude of the forcing displacement and Ω is the forcing angular frequency) to produce droplets from its surface, which is usually referred to as a Faraday instability (**Faraday, 1831**). If the forcing acceleration amplitude $\Delta_0 \Omega^2$ is small, standing waves (Faraday waves) are often observed on the surface (see Fig. 1-1 (a)); while if the forcing acceleration amplitude is enhanced sufficiently beyond Faraday wave formation, ligaments (or spikes) disintegrating into drops are created from the liquid surface (see Fig. 1-1 (b)). Such technique has been widely applied in various fields to produce aerosols or spray, such as ultrasonic atomization (**Wood and Loomis, 1927; Lang, 1962; Rajan and Pandit, 2001; Donnelly et al., 2004**), ultrasound-modulated two-fluid (UMTF) atomization (**Tsai et al., 1996; Tsai et al., 1997**), vibration-induced drop-atomization (VIDA) (**James et al., 2003a; James et al., 2003b; Vukasinovic et al., 2004, 2007**), surface acoustic wave (SAW) atomization (**Qi et al., 2008; Tan et al., 2010**), and so forth. The increasing importance of liquid atomization by Faraday instability in various industrial processes requires a better understanding of the underlying physical dynamics to further enhance the process. In general, any atomization process can be divided into two sub-processes: ligament (or

spike) formation from the liquid surface, and disintegration of the ligament into drops (The term “ligament” in this study is specifically defined as a large liquid surface deformation that results in disintegrated droplets having outward velocities). The mechanism of the latter process, studied extensively through liquid column disintegration research (Eggers, 1997; Eggers and Villermaux, 2008; Umemura, 2011), does not crucially depend on the way the ligament is formed. The disintegration of the ligament into droplets is not the focus of this study. On the other hand, studies on the detailed dynamics of ligament formation from a liquid layer by a Faraday instability have still been limited.

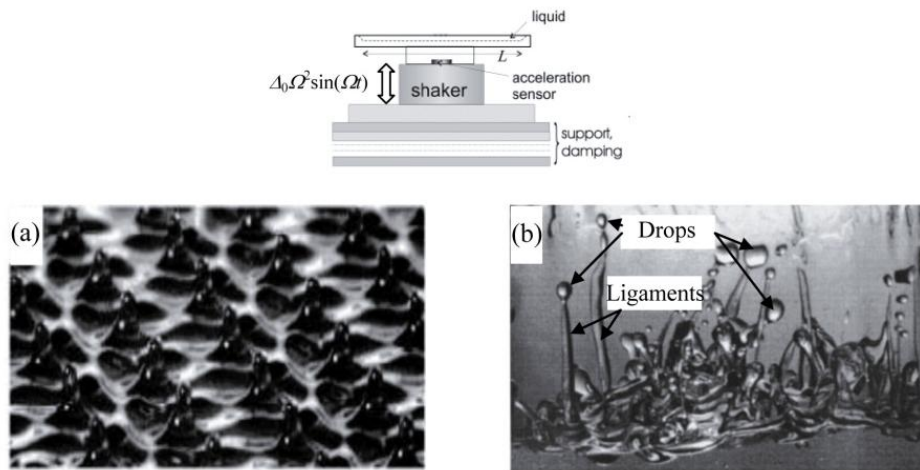


Fig. 1-1 Faraday instability. (a) Formation of the surface standing waves when the forcing acceleration amplitude $\Delta_0 \Omega^2$ is small (Pietschmann et al., 2013). (b) Formation of atomization when the forcing acceleration amplitude $\Delta_0 \Omega^2$ is large (Goodridge et al., 1997).

For industrial application of the atomization due to the Faraday instability, the efficiency of spray formation is the main concern. The threshold condition for spray formation (or steady atomization), in which we are interested in this dissertation, is one of the fundamental characteristics. However, it is not easy to define the threshold condition in a meaningful fashion. The drop ejection considered must occur steadily at a desirable frequency and spacing to satisfy industrial requirements. However, according to descriptions from previous experimental studies, the criteria are defined as “two drops detected within a 10-s period” (Goodridge et al., 1997), “one to about sixteen drops in a 30-s period” (Puthenveetil and Hopfinger, 2009), and “one drop

ejection in 2000 periods of the driving signal” (Vukasinovic et al., 2007). This suggests that these researchers focused on the threshold condition for the event of rare drop ejection, rather than the spray formation composed of vigorous steady drop ejection. Additionally, no universal criterion for drop ejection or spray formation has been suggested to date. Thus, it is necessary to physically define a threshold condition for spray formation that is universal in character.

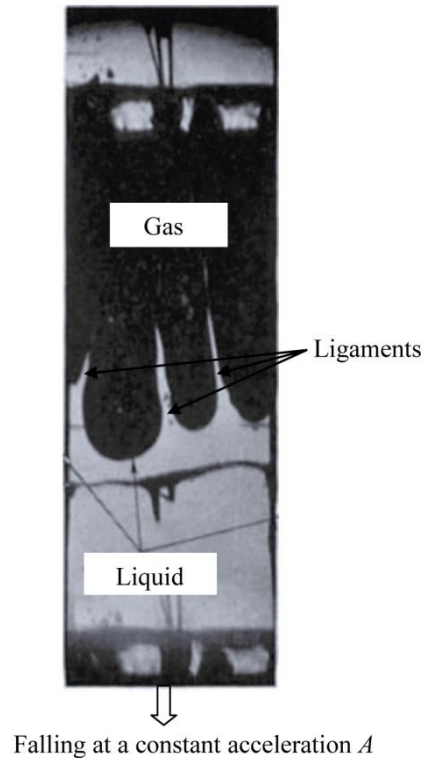


Fig. 1-2 Rayleigh-Taylor instability (Lewis, 1950).

Liquid ligaments can also be created from a liquid layer if a container of liquid falls at a constant acceleration A , which is known as the Rayleigh-Taylor (RT) instability (Rayleigh, 1883; Taylor, 1950) (see Fig. 1-2). In fact, RT instability can be regarded as a Faraday instability in the limit of $\Omega \rightarrow 0$, $\Delta_0 \rightarrow \infty$ and $\Delta_0 \Omega^2 = A = \text{constant}$. RT instability has attracted a lot of academic attentions because it is extensively observed and applied in diverse scientific and industrial fields, including aerophysics (Norman et al., 1981; Arnett et al., 1989), laser fusion (Evans et al., 1982; Lindl et al., 1992), and liquid atomization (Beale and Reitz, 1999; Kong et al., 1999). Revealing the dynamics of RT instability, especially the nonlinear dynamics at the late-time stage

when surface deformation becomes large, is very important for its more extensive application.

1.2 The objective of this research

The nonlinear nature of the atomization phenomenon associated with the Faraday instability and RT instability introduces great complexity into its mathematical treatment. Moreover, due to its inherently small spatiotemporal scales, it is difficult to determine the underlying atomization mechanism solely by experiments. Recent improvements to computer capacity and numerical schemes allow information to be extracted from detailed flow-field data, which are difficult to measure experimentally.

This dissertation addresses three problems proposed in §1.1 by numerical calculations. The objectives in this research are:

- (1) to understand the physical mechanisms of how the inertial effects produce large surface deformation that is dynamically free from the motion of the bottom substrate in Faraday instability by fully analyzing the detailed velocity and pressure fields;
- (2) to determine a threshold acceleration amplitude for spray formation due to Faraday instability based on the physical modeling;
- (3) to illustrate the nonlinear dynamics at the late-time stage of the liquid spike formation due to RT instability by fully analyzing the detailed velocity and pressure fields.

1.3 The outline of this dissertation

The content of this dissertation is organized as follows:

Chapter 2 shows the comprehensive reviews of the previous literatures on the subjects associated with the present study, with focus on the mechanism of the Faraday instability, the threshold condition for drop ejection due to Faraday instability and the dynamics of the RT instability.

Chapter 3 proposes the physical model considered in this dissertation, reviews the numerical methods for capturing the liquid/gas interface, and introduces the detailed numerical methods utilized in the present calculation. We emphasize the conduction of the coupled level-set and volume-of-fluid (CLSVOF).

Chapter 4 introduces the dynamics of the Faraday instability in the linear regime, which is governed by the Mathieu equation. Then, we present the validation of the performance of the numerical code by comparing with other numerical works on Faraday instability. Finally, based on the detailed information on the pressure and velocity fields, we quantitatively demonstrate the detailed mechanisms of the ligament formation from a liquid layer due to Faraday instability.

Chapter 5 discusses the threshold condition for spray formation due to Faraday instability. After briefly reviewing the previous experimental studies on ultrasonic atomization, we propose a novel numerical approach to determine the threshold forcing strength for spray formation. Three conditions are discussed to gain physical insights into the dynamical variation with the forcing strength. The effects of initial disturbance are also discussed in this chapter.

Chapter 6 demonstrates the detailed dynamics associated with the ligament formation due to the RT instability, with the focus on the steady dynamics at the late-time stage. First, we validate the code by comparing with other's numerical works on the RT instability. Second, we conduct an analysis on the characteristic quantities associated with the steady flow at the late-time stage. Finally, we bridge the ligament disintegration due to RT instability to the laboratory low-speed jet experiments by these analytical characteristic quantities.

Chapter 7 summarizes the whole dissertation and provides the future research perspectives.

Chapter 2

Literature review

2.1 Faraday instability

Faraday instability problem originates from the observation of surface waves on ink, water, alcohol, turpentine, milk, and white of egg covering a horizontal plate subjected to a vertical vibration by **Faraday (1831)**. He found that the surface waves oscillate with one half frequency of the vertical vibration. Since then, a lot of scientific attentions have been attracted on this Faraday instability, which are reviewed in this section.

2.1.1 Linear theory of Faraday instability

Benjamin and Ursell (1954) carried out a systematical theoretical analysis of a Faraday instability in the linear regime for ideal fluids. They considered a vessel containing a heavy liquid of density ρ_1 and depth y_0 vibrating vertically with constant frequency Ω and amplitude Δ_0 . Based on the linearized governing Eulerian equations of motion and boundary conditions, they derived a standard Mathieu equation to govern the development of the amplitude of the initially imposed infinitesimal surface disturbance. Whether the free surface is stable or not is dependent on two parameters X and Y , which are going to be defined as Eq. (4-2) in Chapter 4. Taking X as the abscissa and Y the ordinate, they obtained an instability chart, which divided the whole X - Y plane into stable and unstable regions. According to their theory, surface deformation with sub-harmonic, harmonic, or higher-order oscillations, with respect to the forcing frequency, is excitable when the ratio of the surface deformation frequency to the forcing frequency equals to $1/2$, 1 , or $n/2$, where $n = 3, 4, \dots$

In the linear theory for inviscid fluids, the various surface responses to the vertical

vibration (*i.e.*, sub-harmonic, harmonic, or higher-order oscillations) are excited at an even opportunity, because the leftmost point of each unstable response (corresponding to the onset of each instability) occurs at vanishing forcing amplitude. This contradicts the experimental observations, in which the sub-harmonic response always dominates others. Other than former treatment of liquid viscosity, that is, simply adding a linear damping term into Mathieu equation to emulate viscous effect (**Eisenmenger, 1959; Miles, 1967**), whose results disagreed with the experimental one, **Kumar and Tuckerman (1994)** and **Kumar (1996)** theoretically studied the effect of viscosity on Faraday instability using linear stability analysis starting from Navier-Stokes (NS) equations. They attributed this contradiction to the presence of the small viscous dissipation in experiments, which moves the leftmost point away from zero for all responses. They argued that the experimental observed surface response is always sub-harmonic because the leftmost point of the sub-harmonic response moves least. They derived an approximate threshold forcing acceleration amplitude which is in good agreement with experimental results.

In addition to uncontaminated free surfaces, **Kumar and Matar (2004)** analyzed the formation of Faraday waves at a surfactant-covered surface by applying linear stability analysis and Floquet theory to the linearized NS equations. They found that the existence of surfactant would either enhance or lower the threshold vibration amplitude required stimulating the Faraday waves depending on the Marangoni number, which is defined as the ratio of surface-tension gradient force to viscous force.

2.1.2 Faraday standing wave patterns

Linear theory only validates when the surface deformation is small. Nonlinear effects become dominant when the surface deformation is comparable with the wavelength. Early efforts made to the nonlinear effects on the Faraday instability, which usually incorporated terms of higher orders, were reviewed by **Miles and Henderson (1990)**

One striking nonlinear behavior due to Faraday instability is the formation of the

surface standing wave patterns, which has attracted considerable attentions recently. Various patterns of Faraday standing waves, for example, parallel stripe patterns, square pattern and hexagonal patterns, can be observed when the forcing amplitude exceeds some critical value. In a series of theoretical studies by **Zhang and Viñals (1996, 1997a, b, 1998)** and **Chen and Viñals (1997)**, a standing wave amplitude equation from the NS equations of gradient form was derived to predict surface standing wave patterns. They attained a chart of selected patterns as a function of the viscosity of the liquid and the angular forcing frequency, which agrees well with the observation on a large aspect ratio experiment involving fluids of various viscosities by **Kudrolli and Gollub (1996)**. This theoretical work was further confirmed quantitatively by the subsequent experiment investigation carried out by **Westra et al. (2003)**, who devised a simple model that can explain quantitatively the change of the patterns. From a weakly nonlinear analysis, **Mancebo and Vega (2006)** derived three types of Ginzburg-Landau-like amplitude equations depending on the ratio between wavelength, depth and the viscous length. **Perinet et al. (2009)** studied the dynamics of Faraday patterns for two incompressible and immiscible viscous fluids by three-dimensional (3D) numerical calculations. They successfully simulated the square and hexagonal surface patterns. The calculation results agree well with the experiments implemented by **Kityk et al. (2005)**.

2.1.3 Large surface deformation due to Faraday instability

When the forcing acceleration amplitude is enhanced sufficiently beyond Faraday wave formation, spikes disintegrating into droplets are created from the liquid surface. One typical application of such a technique is the so-called “ultrasonic atomization”, the forcing frequency of which is on the order of 10 kHz to 1 MHz. Experimental research on the ultrasonic atomization was first conducted by **Lang (1962)**, who derived a correlation between the median droplet diameter and the forcing frequency in the frequency range of 10 to 800 kHz. **Rajan and Pandit (2001)** studied the effects of the liquid properties including the flow rate, viscosity, density, and surface tension, and

the ultrasonic properties including the forcing displacement amplitude and frequency to predict the droplet size. **Donnelly et al. (2004)** used ultrasonic atomization to produce liquid aerosols with the droplet size in the order of micrometer. They found the relationship between average droplet size and forcing frequency follows an inviscid scaling law proposed by **Lang (1962)**. **Al-Sueimani et al. (1999)**, **Yule and Al-Suleimani (2000)** and **Al-Suleimani and Yule (2002)** investigated the disorder in surface standing waves using high-speed imaging techniques to explain the random ejection locations and the range of droplet sizes generated by ultrasonic atomization. They claimed that the Froude number (inertial force/gravitational force) does not affect the droplet size or droplet formation process. Besides the liquid layer, a parent liquid drop resting on a vertically vibrating horizontal diaphragm into a spray (VIDA) has also received a lot of attentions recently. **James et al. (2003a)** devised a simple mathematical model of the VIDA process to explain the basic physics of the system. **James et al. (2003b)** numerically investigated the effects of the system parameters (Reynolds number (inertial force/viscous force), the dimensionless forcing acceleration amplitude (inertial force/capillary force), and the Bond number (gravitational force/capillary force)) on the drop ejection dynamics (the volume and velocity of the ejected drop and the time of ejection) in VIDA. **Vukasinovic et al. (2004)** experimentally measured the mean diameter of the droplets in VIDA, which is dependent on the forcing frequency to the $-2/3$ power. This dependence is consistent with that in ultrasonic atomization. **Vukasinovic et al. (2007)** experimentally studied the mechanism of free surface breakup in VIDA at forcing frequencies on the order of 1 kHz. They established the dependence of the breakup time and the unbroken spike length on the capillary number (viscous force/capillary force).

However, these previous studies have focused mainly on the dynamics or mechanisms of droplet formation. Studies of the detailed dynamics of spike formation from a liquid layer by a Faraday instability have been limited. Thus far, it has been established that the inertial effect plays an essential role in ligament formation. To quantify the condition for spray formation by a Faraday instability, we must reveal the

physical mechanism of how the inertial effects produce large surface deformation that is dynamically free from the motion of the bottom substrate by fully analyzing the detailed velocity and pressure fields.

Due to the short time and spatial scales in Faraday instability regime, it is difficult to divulge its underlying physics fully only by experiments. Then, numerical techniques, which can provide detailed information on velocity and pressure fields, are often introduced to facilitate investigations. **Chen (2002)** numerically studied the nonlinear dynamics of the Faraday waves, with a focus on the interaction between different modes. **Murakami and Chikano (2001)** and **Ubal et al. (2003)** investigated the effects of viscosity and liquid depth on two-dimensional (2D) Faraday waves, respectively. **Wright et al. (2000)** numerically simulated the 2D Faraday waves in inviscid condition by means of boundary-integral method and vortex-sheet method. The temporal period tripling, observed in experiment, was captured successfully by their simulation. A certain mass of liquid spike penetrating into the gas phase was also simulated by **Wright et al. (2000)** until the droplet at the spike tip is going to be pinched off, which is failed to be simulated by their numerical scheme. Similar numerical study was done by **Takagi and Matsumoto (2011)** recently with phase-field method. **James et al. (2003b)** simulated the VIDA process by an axi-symmetric volume-of-fluid (VOF) method, which can capture the pinch-off of the droplet at the spike tip. 3D simulation of Faraday waves was carried out by **Perinet et al. (2009)**. In this dissertation, we conducted a numerical calculation to obtain the detailed velocity and pressure fields, which we analyzed to study the fundamental dynamics of the ligament formation from the liquid layer due to Faraday instability.

The threshold condition for rare drop ejection due to Faraday instability has received very little attention until recently. **Goodridge et al. (1996)**, **Goodridge et al. (1997)** and **Goodridge et al. (1999)** first experimentally studied the threshold conditions for rare droplet ejection by a Faraday instability at low frequencies below 100 Hz. The threshold forcing acceleration amplitude is dependent on the surface tension and forcing frequency for low-viscosity liquids, and on the viscosity and

forcing frequency for high-viscosity liquids. **Vukasinovic et al. (2007)** measured the threshold condition for rare drop ejection in VIDA experiments, which showed the same dependence of the threshold forcing acceleration on the surface tension and the forcing frequency as that in Goodridges' experiments for low-viscosity liquids, except that the prefactor is larger (see Eq. (5-1) in Chapter 5). **Puthenveetil and Hopfinger (2009)** experimentally investigated the evolution from the wave patterns formation to the wave-breaking in a forcing frequency range 25–100 Hz. They distinguished two thresholds for the onsets of wave pattern and rare drop ejection. However, for industrial application of the Faraday instability to ultrasonic atomisation, the spray formation (instead of rare drop ejection) efficiency is the main concern. The threshold condition for spray formation (or steady atomisation), in which we are interested in this dissertation, is one of the fundamental characteristics of ultrasonic atomisation. The drop ejection considered must occur steadily at the desirable frequency and spacing to satisfy industrial requirements. According to descriptions from past experimental studies shown above, the criteria are defined as “two drops detected within a 10-s period” (**Goodridge et al., 1997**), “one to about sixteen drops in a 30-s period” (**Puthenveetil and Hopfinger, 2009**), and “one drop ejection in 2000 periods of the driving signal” (**Vukasinovic et al., 2007**). This suggests that these researchers concentrated on the threshold condition for the event of rare drop ejection, rather than the spray formation composed of vigorous steady drop ejection. In addition, the experimentally determined threshold conditions seem to be dependent on the experimental setup as indicated by different threshold values in different experimental conductions, *e.g.*, the different prefactors in the threshold function of forcing frequency (Eq. (5-1) in Chapter 5) obtained by **Goodridge et al. (1997)** and **Vukasinovic et al. (2007)**. Thus, it is necessary to physically define a threshold condition for spray formation that has a universal (not experiment-dependent) character. We will look for a rational numerical approach to this problem based on our physical insights into the past experimental results and try to find the threshold condition for spray formation numerically in this dissertation.

2.2 Rayleigh-Taylor instability

The theoretical study on the RT instability originates from the work by **Taylor (1950)**, who derived a linear solution to the development of a sinusoidal disturbance (single Fourier mode) initially imposed on the interface. Neglecting the surface tension and viscosity, he found that the initial disturbance grows exponentially with time until it reaches a magnitude which is no longer small compared with the wavelength λ . The linear growth rate is expressed as $\alpha = \sqrt{kAa_t}$, where $k = 2\pi/\lambda$ is the wave number, A is the effective acceleration, and $a_t = (\rho_2 - \rho_1)/(\rho_2 + \rho_1)$ (ρ_2 and ρ_1 are the densities of heavier fluid and lighter fluid, respectively) is the Atwood number. The extended linear theory including the effects of surface tension and viscosity was reported by **Bellman and Pennington (1954)** and **Piriz et al. (2006)**. Surface tension has a stabilizing effect on the RT instability, which reforms the growth rate to

$$\alpha = \sqrt{kAa_t - \frac{\sigma k^3}{\rho_2 + \rho_1}}, \quad (2-1)$$

where σ is the coefficient of surface tension. Equation (2-1) indicates that there exists a cutoff wave number above which the initial disturbance cannot be grown. On the other hand, viscosity has a damping effect on the growth rate. When the surface tension is absent, the growth rate considering viscosity is the solution to the quadratic equation (**Piriz et al., 2006**)

$$\alpha^2 + \left(\frac{\mu_1 + \mu_2}{\rho_2} \right) (1 + a_t) k^2 \alpha - a_t k A = 0, \quad (2-2)$$

where μ_2 and μ_1 are the dynamical viscosity coefficients of the heavier and lighter fluids, respectively. Generalization of the linear theory to include other physical effects *e.g.*, compressibility, density gradients, and so forth, was reviewed by **Sharp (1984)**.

When the exponentially growing surface deformation amplitude is not small

compared with the wavelength, linear theory is no longer valid and nonlinear effect becomes dominant. **Lewis (1950)** conducted a series of RT instability experiments in a liquid-gas system, where the Atwood number approaches unity, to validate Taylor's linear theory. He observed that the linear theory is validated until the amplitude reaches about 0.4λ and that, at the late-time developing stage, the round-ended gas columns (bubbles) penetrate into the liquid of higher density at a constant velocity, which is proportional to \sqrt{Ar} , where r is the radius of curvature of the tip of the gas column. This nonlinear saturation of the bubble penetration velocity aroused great interests of the following researchers. **Layzer (1955)**, **Garabedian (1957)** and **Birkhoff and Carter (1957)** theoretically studied a symmetrical bubble rising under gravity in a vertical tube with parallel walls, which is similar to the bubble behavior at the late-time stage in the RT instability in the case $a_t \approx 1$, based on an approximate potential flow model. The constant bubble rising velocity is proportional to \sqrt{gD} , where g is the gravitational acceleration and D is the distance between two parallel walls. **Alon et al. (1995)**, **Goncharov (2002)** and **Sohn (2003)** extended the similar analysis to the RT instability at arbitrary Atwood number for the nonlinear bubble evolution, and expressed the constant bubble rising velocity as

$$V = \sqrt{\frac{2a_t}{1+a_t} \frac{A}{C \cdot k}}, \quad (2-3)$$

where $C = 3$ and $C = 1$ for the 2D and 3D configurations, respectively. Alternatively, **Oron et al. (2001)** developed a simple drag-buoyancy model, which is based on the 2D and 3D drag and added mass coefficients obtained from the Layzer model, to investigate the late-time nonlinear evolution. This model yields the same constant

bubble rising velocity as the potential flow model. **Waddell et al. (2001)** experimentally studied the 2D RT instability at low Atwood number with a single-mode initial disturbance. They observed that, when the two fluid densities are similar, velocities of the gas bubble (of lower density) and the liquid spike (of higher density) both approach constant values, which agree with the theoretical predictions by **Oron et al. (2001)** and **Goncharov (2002)**. **Wilkinson and Jacobs (2007)** conducted an experimental study on the single-mode 3D RT instability for a low Atwood number ($a_t = 0.15$). They showed that the measured amplitude only agree with the linear theory until the amplitude reaches about 0.16λ . Besides the single-mode instability, experimental efforts on the multi-mode RT instability, initiated by a random disturbance, can be found in **Read (1984)**, **Dalziel et al. (1999)**, **Ramaprabhu and Andrews (2004)**, **Dimonte et al. (2005)**, **Andrews and Dalziel (2010)** and **Banerjee et al. (2010)**.

Because of the difficulty in controlling the initial disturbance amplitude in experiments, numerical simulations are adopted to study the RT instability. **Baker et al. (1980)** simulated a 2D single-mode RT instability to large amplitudes in inviscid, incompressible flows by a vortex technique. The calculated constant velocity at the bubble tip at the late-time stage is in agreement with the prediction derived by **Birkhoff and Carter (1957)**. **Baker et al. (1980)** also presented the simulation results at various Atwood numbers. **Baker et al. (1987)** numerically studied the effect of the liquid layer thickness on the bubble motion, which cannot be neglected when the thickness becomes thinner than about half a wavelength. **Ramaprabhu and Dimonte (2005)**, **Ramaprabhu et al. (2006)** and **Ramaprabhu et al. (2012)** investigated a single-mode RT interface behavior at different Atwood number ranging from 0.005 to 1 using 3D numerical simulations. They found that the asymptotic radius of curvature at the bubble tip is independent of the Atwood number. For low and moderate Atwood number, due to the secondary Kelvin-Helmholtz (KH) instability on the bubble-spike interface, the velocity at the bubble tip is no longer constant but accelerated as the bubble penetration depth exceeds the diameter of bubbles. **Youngs (1984)** used a 2D

code to simulate the turbulent mixing due to RT instability by imposing an initial disturbance consisting of many different modes on the surface. **Ramaprabhu et al. (2005)** numerically studied the effect of initial conditions on the growth rate of turbulent RT mixing by solving 3D incompressible Euler equations with numerical dissipation.

The previous theoretical, experimental and numerical investigations on the nonlinear dynamics of the RT instability have focused mainly on the gas bubble behaviors, especially on the constant bubble rising velocity. However, for the application of RT instability to the liquid atomization field, the liquid spike behaviors are of more interest. In the problem of liquid atomization by RT instability, in which the Atwood number is large, the developed liquid spike at the late-time stage approaches free-fall, which can be considered as a liquid jet emanating from an orifice injector under normal gravity and disintegrating into droplets (**Schulkes, 1994; Umemura, 2011**). The theory on the jet disintegration process has been investigated extensively (**Eggers, 1997; Lin, 2003; Eggers and Villermaux, 2008; Shinjo and Umemura, 2010; Umemura, 2011**). In order to link the jet theory with the RT spike, the position which is analogous to the orifice injector exit, the liquid velocity and width at that position (analogous to the jet emanating velocity and diameter at the orifice injector exit) must be identified physically. To the best of our knowledge, there are few studies on bridging the two fundamental studies on interfacial instability and low-speed jet disintegration to characterize the atomization from a liquid surface. Thus, in this dissertation (Chapter 6), we conducted a numerical calculation for a single-mode RT instability at large Atwood number, with an attempt at the analytical expressions for the quantities characterizing the liquid spike from a liquid layer based on the detailed information on the velocity and pressure fields.

Chapter 3

Numerical methods

In this chapter, we first proposed the physical model considered in this dissertation, including the governing equations, calculation domain, boundary conditions, and initial conditions, *etc.*. Then, we specified the numerical methods utilized to solve the governing Euler equations for incompressible fluids and to capture the liquid/gas interface. Some test calculation cases for validation of the numerical methods and programming codes are also presented in this chapter.

3.1 Physical model

As shown in Fig. 3-1, we considered a liquid layer (of density ρ_l) above which a gas layer (of density ρ_g) overlays, resting horizontally on a substrate. For a Faraday instability, the substrate is subject to a vertical vibration of standard sinusoidal displacement $\Delta_0 \sin(\Omega t)$, where Δ_0 is the forcing displacement amplitude and Ω is the forcing angular frequency. For an RT instability, the substrate moves downward with a time-independent acceleration of $A + g$, where g is the gravity acceleration.

In this dissertation, we considered a 2D problem. The difference and the sameness between 2D and 3D considerations will be discussed in corresponding chapters (Chapter 4 and Chapter 5). **Wright et al. (2000)** and **Takagi and Matsumoto (2011)** showed that 2D calculation captures the characteristic nonlinear dynamics of a Faraday instability, *i.e.*, large surface deformation from the liquid layer. **Baker et al. (1980)** also captured the major dynamics associated with a RT instability by a 2D calculation.

Additional assumptions made for simplicity are as follows. Consistent with Fig. 3-1, the effects of viscosity are ignored for both the studies on the Faraday instability and RT instability. For the Faraday instability, the viscous damping effect suppresses

the breakup (Goodridge et al., 1997; James et al., 2003b; Vukasinovic et al., 2004). However, if the forcing frequency satisfies the condition $4\nu_1^2(\rho_1/\sigma)^{4/3}\Omega^{2/3} \ll 1$, where ν_1 is the liquid kinematic viscosity and σ is the surface tension coefficient, the vibrating liquid can be considered to be in an inviscid regime (Eisenmenger, 1959). Even in the practical ultrasonic atomization, for which a low-viscosity liquid is usually used to make the atomization process effective, this condition is usually satisfied. For example, we can estimate $4\nu_1^2(\rho_1/\sigma)^{4/3}\Omega^{2/3} = 0.07$ for a distilled water layer at a forcing frequency of $f = 2\pi/\Omega = 2$ MHz, which approximates one experimental condition carried out by Donnelly et al. (2004). For the RT instability, Eq. (2-2) indicates that the viscous damping effect is negligible if $k^3\nu_1^2 \ll A$. Thus, the calculation results based on the inviscid assumption are valid in the range $k^3\nu_1^2/A \ll 1$. Furthermore, for the Faraday instability, capillary effects dominate over gravitational effects when another condition $\Omega > \Omega_* = g^{3/4}(\rho_1/\sigma)^{1/4}$ (Donnelly et al., 2004) is satisfied. Again, the distilled water layer example yields $\Omega_* = 60.8$ rad/s (*i.e.*, $f_* = 9.7$ Hz). As a result, it is reasonable to neglect the gravity when the forcing frequency is larger than $f_b = 10$ Hz for distilled water.

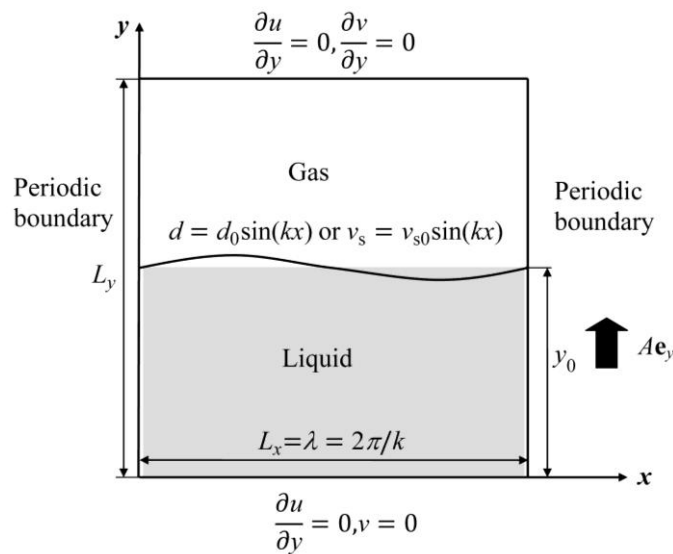


Fig. 3-1 Schematic illustration of the calculation domain, boundary conditions and initial condition.

The fluids in all the problems studied in this dissertation are incompressible and in the reference frame attached to the moving substrate, the motions are governed by the Euler equations, *i.e.*,

$$\begin{cases} \nabla \cdot \mathbf{u} = 0 \\ \rho(\phi) \left[\frac{\partial \mathbf{u}}{\partial t} + (\mathbf{u} \cdot \nabla) \mathbf{u} \right] = -\nabla p + \rho(\phi) A \mathbf{e}_y + \mathbf{F}_s \end{cases} \quad (3-1)$$

where \mathbf{u} is the velocity vector, whose vertical component is the one referring to the substrate, p is the pressure, \mathbf{e}_y is the unit vertical vector, A (=constant for the RT instability, and $=\Delta_0 \Omega^2 \sin(\Omega t)$ for the Faraday instability) is the effective inertial acceleration imposed on the fluids, and \mathbf{F}_s is the body force vector expressing the surface tension force, which was evaluated by the continuum surface force (CSF) method (**Brackbill et al., 1992**)

$$\mathbf{F}_s = \sigma \kappa \nabla H_\varepsilon(\phi). \quad (3-2)$$

The surface tension force was transformed into the volume force and scattered in a region around interface with a constant thickness ε in this dissertation. The effect of this thickness ε is shown in Fig. 3-2, which shows that ε does not significantly affect the major dynamics associated with the Faraday instability in the range $\Delta x < \varepsilon < 4\Delta x$ ($\Delta x = \lambda/64$). We used $\varepsilon = 3\Delta x$ for all calculations. $\kappa = -\nabla \cdot \mathbf{n} = -\nabla \cdot (\nabla \phi / |\nabla \phi|)$ is the curvature of the interface, where ϕ is the level-set (LS) function, which will be discussed in detail in §3.2.2; \mathbf{n} is the unit normal vector to the liquid/gas interface, and H_ε is the smoothed Heaviside function with thickness ε

$$H_\varepsilon(\phi) = \begin{cases} 0, & \phi < -\varepsilon \\ \frac{1}{2} \left[1 + \frac{\phi}{\varepsilon} + \frac{1}{\pi} \sin\left(\pi \frac{\phi}{\varepsilon}\right) \right], & |\phi| \leq \varepsilon \\ 1, & \phi > \varepsilon \end{cases} \quad (3-3)$$

$\rho(\phi)$ is the smoothed density function in each cell defined by

$$\rho(\phi) = \rho_l \cdot H_\varepsilon(\phi) + \rho_g \cdot [1 - H_\varepsilon(\phi)]. \quad (3-4)$$

The liquid-to-gas density ratio was taken as $\rho_l/\rho_g = 50$ for all the calculation cases to retain numerical stability. This density ratio is considerably smaller than the usual water-air system ($\rho_l/\rho_g = 850$), but it is the Atwood number $a_t = (\rho_2 - \rho_1)/(\rho_2 + \rho_1)$ that is used to evaluate the density ratio effects on the Faraday instability or RT instability. The Atwood number in the two cases are 0.96 and 0.99, respectively, which are very close to unity. **James et al. (2003b)** have studied the effects of density ratio on the major dynamics in VIDA. They showed that the drop ejection volume and drop ejection time are almost independent of the density ratio ρ_l/ρ_g in the range from ∞ to 50. In this density ratio range, the dynamical variation in the RT instability is little as well (**Ramaprabhu and Andrews, 2004; Ramaprabhu and Dimonte, 2005**). This indicates that the dynamics obtained from the present numerical calculations with $\rho_l/\rho_g = 50$ can be applied to the usual water-air system.

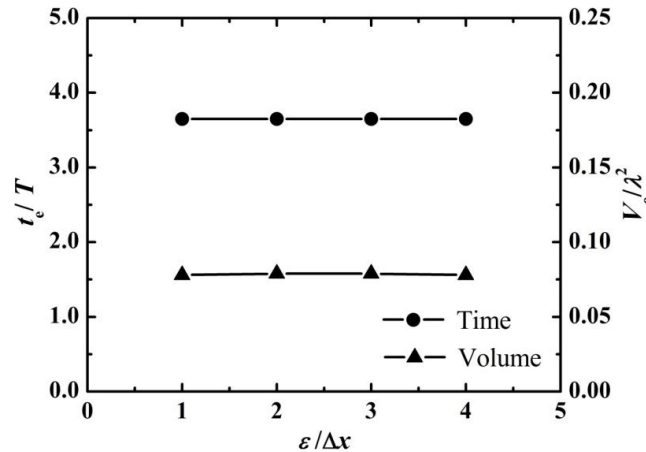


Fig. 3-2 Effects of the thickness of the interfacial transition region, ε , on the major dynamics associated with the Faraday instability. t_e is the first drop ejection time and V_e is the first drop ejection volume. $T=2\pi/\Omega$ is the forcing period.

The equations (3-1) were solved with the boundary conditions specified in Fig. 3-1. In the horizontal direction, a cyclic condition was imposed at the left and right boundaries. The top edge of the calculation domain was set as a free boundary. In the Faraday or RT instability, the major dynamics of interest influenced by the liquid surface deformation are only limited to a depth of $1/k$ from the surface. It is extremely time-consuming and unnecessary to simulate the entire liquid depth for our purpose in the present study. In fact, the liquid located deeper than the surface deformation influence depth ($> 1/k$) moves with the vibrating bottom substrate essentially, and thus has the same effect as the bottom substrate. Then, unless otherwise stated (*e.g.*, in §4.3.3 below), the liquid depth was set to be $y_0 = \lambda > 1/k$, which made the simulation more realizable, and set the bottom boundary of the cell model as a slip wall. The calculation domain spanned one wavelength horizontally ($L_x = \lambda$) and two and a half wavelengths vertically ($L_y = 2.5\lambda$).

Initially, both the liquid and the gas phases were set to be stagnant except for the interface which was disturbed to initiate the instability. In this study, the initial disturbance was introduced as the imposition of a vertical surface velocity distribution $v_s = v_{s0} \sin(kx)$, where v_{s0} is a small value compared to the amplitude of vibration velocity. This definition of disturbance is equivalent to the imposition of an initial surface displacement distribution $d = d_0 \sin(kx)$ and it is easier for numerical conduction in this study. Unless otherwise specified, the flow movement is described in the frame of reference moving with the vibrating substrate hereafter.

The governing equations were discretized on a uniform, staggered grid. The effects of the grid resolution ($\Delta x = \Delta y$) were evaluated by comparing the numerical results for different grid resolutions, which are shown in Fig. 3-3 and Fig. 3-4. For the Faraday instability, as shown in Fig. 3-3, we compared the first drop ejection time t_e or the first drop ejection volume V_e for the atomization case discussed in Chapter 5. The grid resolution finer than $\lambda/32$ had little effects on the essential dynamics associated with the Faraday instability. For the RT instability, as shown in Fig. 3-4, we compared the constant descending velocity of the trough surface V and the constant

amplitude of the sinusoidal trough surface δ_0 for a large effective acceleration case ($A^* = 8.8\pi^3$ discussed in Chapter 6). The result showed that the grid resolution finer than $\lambda/48$ has little effect on the major dynamics of RT instability. The grid resolution in the present study was set to be $\Delta x = \Delta y = \lambda/64$, which is considered to be fine enough to capture the dynamics correctly.

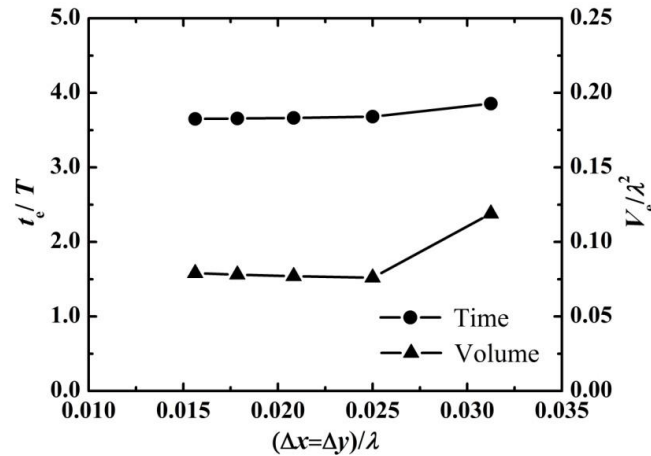


Fig. 3-3 Effects of the grid resolution on the major dynamics associated with the Faraday instability.

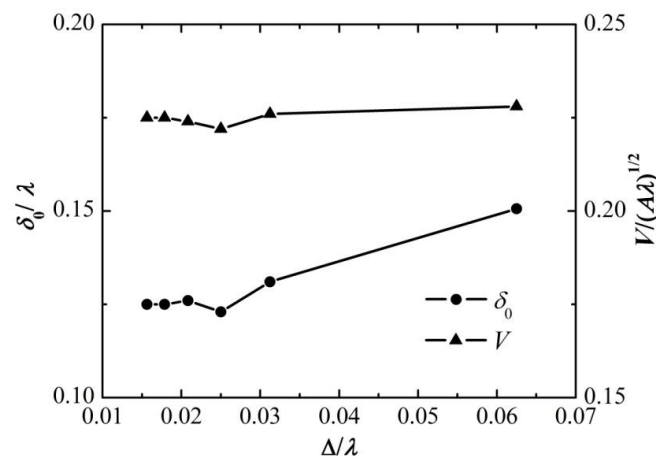


Fig. 3-4 Effects of the grid resolution on the major dynamics associated with the RT instability.

The time step Δt at each calculation instant was adapted by two restrictions to ensure stable numerical results, *i.e.*, materials (*e.g.*, the free surface) and the capillary

waves formed by the surface tension cannot travel a distance more than one cell size within one time step. Then, we have (Nichols et al., 1980)

$$\Delta t = \min \left[C_r \frac{\Delta x}{|u_{\max}|}, C_r \frac{\Delta y}{|v_{\max}|}, \sqrt{\frac{\min(\rho_l, \rho_g)}{4\sigma} \min(\Delta x, \Delta y)^3} \right], \quad (3-5)$$

where C_r , the Courant number, was set to be 0.25 in our calculations; u_{\max} and v_{\max} are the maximum values of the horizontal and vertical velocities at each calculation instant, respectively.

3.2 Numerical solver

3.2.1 Numerical methods for solving Euler equations

As mentioned above, a uniform and staggered mesh (see Fig. 3-5) was used to discretize the governing equations. The velocity vector was stored at the cell edge, while the pressure and density were stored at the cell center, as shown. This grid configuration is suitable for the "marker-and-cell (MAC)" method (Harlow and Welch, 1965) used to solve the temporal evolution of the pressure and velocity fields.

At first, neglecting the pressure gradient term, an explicit second-order upwind scheme for discretion of the convective terms was employed to advance the intermediate velocities (with the superscript *) from those at the previous instant (the $(n-1)$ -th instant). For the u -control volume,

$$u_{i,j}^* = u_{i,j}^{n-1} - \Delta t \cdot \left(u_{i,j}^{n-1} \cdot \frac{\chi \cdot 4u_{i+\chi,j}^{n-1} - \chi \cdot 3u_{i,j}^{n-1} - \chi \cdot u_{i+2\chi,j}^{n-1}}{2\Delta x} + v_{u,i,j}^{n-1} \cdot \frac{\psi \cdot 4u_{i,j+\psi}^{n-1} - \psi \cdot 3u_{i,j}^{n-1} - \psi \cdot u_{i,j+2\psi}^{n-1}}{2\Delta y} \right) + \Delta t \cdot \frac{\sigma \kappa}{\rho_{u,i,j}^{n-1}} \cdot \frac{H_\varepsilon(\phi_{i+1,j}^{n-1}) - H_\varepsilon(\phi_{i,j}^{n-1})}{\Delta x}, \quad (3-6)$$

where the superscript at the right hand side denotes the time index and the subscript denotes the cell index;

$$v_{u\ i,j}^{n-1} = (v_{i,j}^{n-1} + v_{i+1,j}^{n-1} + v_{i,j-1}^{n-1} + v_{i+1,j-1}^{n-1})/4 \quad ,$$

$\rho_{u\ i,j}^{n-1} = (\rho_{i,j}^{n-1} + \rho_{i+1,j}^{n-1})/2$, and

$$\chi = -\text{sgn}(u_{i,j}^{n-1}) = \begin{cases} 1, & u_{i,j}^{n-1} < 0 \\ -1, & u_{i,j}^{n-1} \geq 0 \end{cases} \quad \text{and} \quad \psi = -\text{sgn}(v_{u\ i,j}^{n-1}) = \begin{cases} 1, & v_{u\ i,j}^{n-1} < 0 \\ -1, & v_{u\ i,j}^{n-1} \geq 0 \end{cases} \quad (3-7)$$

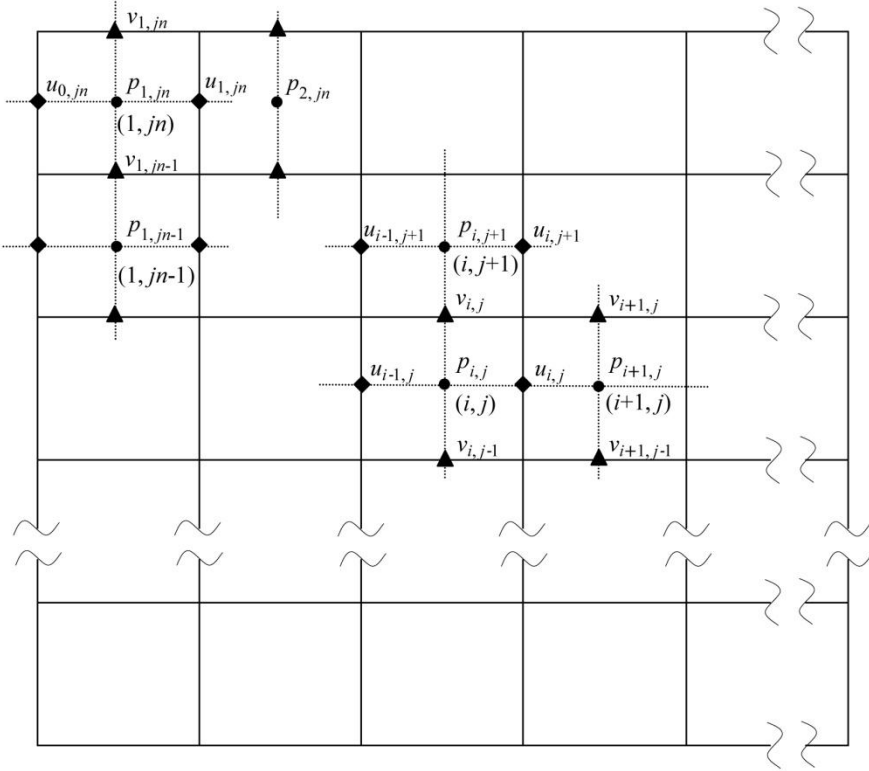


Fig. 3-5 Staggered mesh used in this dissertation.

Similarly, for the v -control volume,

$$v_{i,j}^{\circ} = v_{i,j}^{n-1} - \Delta t \cdot \left(u_{v\ i,j}^{n-1} \cdot \frac{\varpi \cdot 4v_{i+\varpi,j}^{n-1} - \varpi \cdot 3v_{i,j}^{n-1} - \varpi \cdot v_{i+2\varpi,j}^{n-1}}{2\Delta x} + v_{i,j}^{n-1} \cdot \frac{t \cdot 4v_{i,j+t}^{n-1} - t \cdot 3v_{i,j}^{n-1} - t \cdot v_{i,j+2t}^{n-1}}{2\Delta y} \right) + \Delta t \cdot \frac{\sigma\kappa}{\rho_{v\ i,j}^{n-1}} \cdot \frac{H_{\varepsilon}(\phi_{i,j+1}^{n-1}) - H_{\varepsilon}(\phi_{i,j}^{n-1})}{\Delta y}, \quad (3-8)$$

where $u_{v\ i,j}^{n-1} = (u_{i,j}^{n-1} + u_{i,j+1}^{n-1} + u_{i-1,j}^{n-1} + u_{i-1,j+1}^{n-1})/4$, $\rho_{v\ i,j}^{n-1} = (\rho_{i,j}^{n-1} + \rho_{i,j+1}^{n-1})/2$, and

$$\varpi = -\text{sgn}(u_{v\ i,j}^{n-1}) = \begin{cases} 1, & u_{v\ i,j}^{n-1} < 0 \\ -1, & u_{v\ i,j}^{n-1} \geq 0 \end{cases} \quad \text{and} \quad t = -\text{sgn}(v_{i,j}^{n-1}) = \begin{cases} 1, & v_{i,j}^{n-1} < 0 \\ -1, & v_{i,j}^{n-1} \geq 0 \end{cases} \quad (3-9)$$

Generally, these intermediate velocities did not satisfy the continuum equation due to the pressure change. The velocities at the present instant (n -th instant) derived from the intermediate velocities

$$u_{i,j}^n = u_{i,j}^\circ - \frac{\Delta t}{\rho_{ui,j}^{n-1}} \cdot \left(\frac{p_{i+1,j}^n - p_{i,j}^n}{\Delta x} \right) \quad \text{and} \quad v_{i,j}^n = v_{i,j}^\circ - \frac{\Delta t}{\rho_{vi,j}^{n-1}} \cdot \left(\frac{p_{i,j+1}^n - p_{i,j}^n}{\Delta y} \right) \quad (3-10)$$

should satisfy the continuum equation

$$\frac{u_{i,j}^n - u_{i-1,j}^n}{\Delta x} + \frac{v_{i,j}^n - v_{i,j-1}^n}{\Delta y} = 0 \quad (3-11)$$

Then, a discrete Poisson equation for pressure with the divergence of the intermediate velocity as the source term was derived by substituting Eq. (3-10) into Eq. (3-11),

$$a_1 p_{i+1,j}^n + a_2 p_{i-1,j}^n + a_3 p_{i,j+1}^n + a_4 p_{i,j-1}^n - a_5 p_{i,j}^n = d_{i,j}^\circ, \quad (3-12)$$

where $a_1 = \Delta t / (\rho_{ui,j}^{n-1} \cdot \Delta x)$, $a_2 = \Delta t / (\rho_{ui-1,j}^{n-1} \cdot \Delta x)$, $a_3 = \Delta t / (\rho_{vi,j}^{n-1} \cdot \Delta y)$,
 $a_4 = \Delta t / (\rho_{vi,j-1}^{n-1} \cdot \Delta y)$, $a_5 = a_1 + a_2 + a_3 + a_4$ and $d_{i,j}^\circ = (u_{i,j}^\circ - u_{i-1,j}^\circ) / \Delta x$
 $+ (v_{i,j}^\circ - v_{i,j-1}^\circ) / \Delta y$. The solution of this Poisson equation determined the velocity field at the present instant by Eq. (3-10). The discrete Poisson equation was solved by the traditional Gauss-Seidel iteration method, and the convergence criterion was set as the residual of 10^{-10} .

3.2.2 Coupled Volume-of-Fluid and Level-set method

The essential part of the simulation on the Faraday and RT instabilities is capturing the liquid/gas interface. There are various numerical methods to capture the liquid/gas interface. Besides the moving-grid or adaptive-grid methods, which have been particularly successful for the study of the motion of small amplitude waves and weakly deformed bubbles (**Scardovelli and Zaleski, 1999**), the fixed-grid methods have been widely used for direct numerical simulation of free-surface and interfacial flow. One fixed-grid method is to mark the surface particles initially and trace them as time elapses, which is called ‘‘surface-marker method’’ (**Glimm et al., 1986**;

Tryggvason and Unverdi, 1990). One important advantage of the surface-marker method is that the interface can be represented by the high-order interpolation polynomials, which may improve the accuracy of the curvature evaluation.

The surface-marker method is a Lagrangian-type method, which is required to track each surface particle through the entire calculation. For two-phase flow, the volume-of-fluid method (VOF), which is easy to describe and program, is more widely used in simulating the interface-associated problems. The basic idea of the VOF method is as follows. First, we define a function F whose value is unity in the cell occupied by one fluid and zero by the other. For the cell containing the interface (referred to as the interface cell), which is occupied by both fluids, F is a value between zero and unity ($0 < F < 1$). Second, F is convected by the calculated velocity field

$$\frac{\partial F}{\partial t} + (\mathbf{u} \cdot \nabla) F = 0. \quad (3-13)$$

Third, after the convection, the interface in each interface cell is reconstructed by a polynomial function (usually is a straight line segment) according to the F -value. **Hirt and Nichols (1981)** proposed a simple line interface calculation (SLIC) method to reconstruct the interface in the interface cell. In such SLIC method, which is only first-order accurate, the reconstructed interface is one or two lines aligned with the cell edges. To improve the reconstruction accuracy, a linear approximation to the interface has been used (**Ashgriz and Poo, 1991; Rider and Kothe, 1998; Garrioch and Baliga, 2006**), which results in a piecewise-linear interface calculation (PLIC) method. **Pilliod Jr and Puckett (2004)** introduced two second-order accurate interface reconstruction algorithms based on the PLIC method. Due to the discontinuity essence of VOF function F , Eq. (3-13) is not appropriated to be discretized by traditional numerical schemes but geometrical treatment. The usual method to convect F is so-called “split convection algorithm” (**Pilliod Jr and Puckett, 2004**), in which the convection in different directions is treated independently. This convection algorithm has been proven to be able to obtain satisfactory results for

many interfacial problems except for the problem of unstable displacements in porous media, in which an “unsplit convection algorithm” is preferable to use (**Bell et al., 1988**).

As another method usually used to capture the interface in the fixed grid, the level-set (LS) method was developed by **Sussman et al. (1994)**. In the LS method, a LS function ϕ , which is defined as the signed distance from any point to the interface, is employed to track the interface. Thus, the interface is implicitly depicted by the contour line $\phi = 0$. The basic idea of the LS method is as follows. First, we assign a signed value of LS function ϕ for each cell as the initial condition. Second, the LS function ϕ is convected by the calculated velocity field

$$\frac{\partial \phi}{\partial t} + (\mathbf{u} \cdot \nabla) \phi = 0. \quad (3-14)$$

The numerical treatment of Eq. (3-14) after some time may result in that ϕ becomes irregular and is no longer a distance function (*i.e.*, $|\nabla \phi| \neq 1$). Thus, finally, instead of the reconstruction process in the VOF method, an iterative re-initialization process is employed to retain ϕ a distance function (**Sussman et al., 1994**)

$$\frac{\partial \phi}{\partial \tilde{t}} = \text{sgn}(\phi^\circ)(1 - |\nabla \phi|), \quad (3-15)$$

where ϕ° is the LS value after convection \tilde{t} is a virtual time. Different from the discontinuity property of the VOF function F , ϕ is a continuous function across the interface. Thus, Eq. (3-14) can be treated by the conventional schemes for the convection of velocities, for example, the essential non-oscillation (ENO) scheme (**Sussman and Fatemi, 1999; Son and Hur, 2002**), *etc.*.

The LS method has merits in evaluating curvature due to the continuity nature of ϕ ; however, it usually loses conservation of volume in the re-initialization step required to keep its distance property. Although **Sussman and Fatemi (1999)** proposed a constraint in the re-initialization process to improve its performance in volume conservation, the results were still unsatisfactory. The VOF method is

inherently a volume-conserving method, but its poor behavior in evaluating curvature due to its step-like property around interfaces limits its application. The coupled level-set volume-of-fluid (CLSVOF) method (**Sussman and Puckett, 2000; Son and Hur, 2002; Sussman, 2003; Van der Pijl et al., 2005; M énard et al., 2007; Sun and Tao, 2010**), taking advantages of both methods, has been applied extensively recently with regard to multi-phase calculation. The major difference between these CLSVOF methods is the detailed implement of coupling. In this dissertation, we adopted the mass-conserving level-set (MCLS) method (**Van der Pijl et al., 2005**) to capture the interface to study the Faraday and RT instabilities, the detailed procedures are presented as follows.

1. *VOF function F derived from ϕ* F and ϕ are both defined at the cell center. The value of F is obtained by an explicit function of ϕ .

$$F_{i,j}(\phi_{i,j}, \nabla \phi_{i,j}) = \begin{cases} 0, & \phi_{i,j} \leq -\phi_{\max i,j} \\ \frac{1}{2} \frac{(\phi_{\max i,j} + \phi_{i,j})^2}{(\phi_{\max i,j}^2 - \phi_{i,j}^2)}, & -\phi_{\max i,j} < \phi_{i,j} < -\phi_{\text{mid } i,j} \\ \frac{1}{2} + \frac{\phi_{i,j}}{(\phi_{\max i,j} + \phi_{\text{mid } i,j})}, & -\phi_{\text{mid } i,j} < \phi_{i,j} < \phi_{\text{mid } i,j} \\ 1 - \frac{1}{2} \frac{(\phi_{\max i,j} - \phi_{i,j})^2}{(\phi_{\max i,j}^2 - \phi_{i,j}^2)}, & \phi_{\text{mid } i,j} < \phi_{i,j} < \phi_{\max i,j} \\ 1, & \phi_{i,j} \geq \phi_{\max i,j} \end{cases}, \quad (3-16)$$

where

$$\phi_{\max i,j} = \frac{1}{2} \left(\left| \Delta y \frac{\partial \phi}{\partial y} \right|_{i,j} + \left| \Delta x \frac{\partial \phi}{\partial x} \right|_{i,j} \right), \quad \phi_{\text{mid } i,j} = \frac{1}{2} \left| \Delta y \frac{\partial \phi}{\partial y} \right|_{i,j} - \left| \Delta x \frac{\partial \phi}{\partial x} \right|_{i,j}, \quad (3-17)$$

which are approximated by central differencing.

2. *Convection of LS function ϕ* . After the velocity field is determined at the n -th instant as described in the last section, the LS function ϕ^{n-1} is convected by this velocity field according to Eq. (3-14), which can be solved by traditional schemes. In this dissertation, we adopted the second order ENO scheme (**Sussman and Fatemi, 1999; Son and Hur, 2002**). For incompressible fluids, which are the focuses in this dissertation, Eq. (3-14) can be expressed as the conservative form

$$\frac{\partial \phi}{\partial t} + \nabla \cdot (\mathbf{u}\phi) = 0. \quad (3-18)$$

Then, the x -component of the convective term $\partial(u\phi)/\partial x$ discretized by the ENO scheme is described as

$$\frac{\partial(u\phi)}{\partial x} = \frac{(u\phi)_{i+1/2,j} - (u\phi)_{i-1/2,j}}{\Delta x} = \frac{u_{i,j}\phi_{i+1/2,j} - u_{i-1,j}\phi_{i-1/2,j}}{\Delta x}, \quad (3-19)$$

where the subscripts $(i+1/2, j)$ and $(i-1/2, j)$ represent the right and left edges of the cell (i, j) , respectively. Take the value of ϕ at the left cell edge $\phi_{i-1/2,j}$ for example,

$$\phi_{i-1/2,j} = \begin{cases} \phi_{i-1,j} + \frac{1}{2} \min \text{mod}(\phi_{i,j} - \phi_{i-1,j}, \phi_{i-1,j} - \phi_{i-2,j}), & \text{if } u_{i-1,j} > 0 \\ \phi_{i,j} - \frac{1}{2} \min \text{mod}(\phi_{i,j} - \phi_{i-1,j}, \phi_{i+1,j} - \phi_{i,j}), & \text{otherwise} \end{cases}, \quad (3-20)$$

with

$$\min \text{mod}(a, b) = \begin{cases} a, & \text{if } |a| \leq |b| \\ b, & \text{otherwise} \end{cases}. \quad (3-21)$$

The discrete y -component of the convective term $\partial(v\phi)/\partial y$ has a similar form to Eqs. (3-19) and (3-20), *i.e.*,

$$\frac{\partial(v\phi)}{\partial y} = \frac{(v\phi)_{i,j+1/2} - (v\phi)_{i,j-1/2}}{\Delta y} = \frac{v_{i,j}\phi_{i,j+1/2} - v_{i,j-1}\phi_{i,j-1/2}}{\Delta y}, \quad (3-22)$$

and

$$\phi_{i,j-1/2} = \begin{cases} \phi_{i,j-1} + \frac{1}{2} \min \text{mod}(\phi_{i,j} - \phi_{i,j-1}, \phi_{i,j-1} - \phi_{i,j-2}), & \text{if } v_{i,j-1} > 0 \\ \phi_{i,j} - \frac{1}{2} \min \text{mod}(\phi_{i,j} - \phi_{i,j-1}, \phi_{i,j+1} - \phi_{i,j}), & \text{otherwise} \end{cases}, \quad (3-23)$$

where the subscripts $(i, j+1/2)$ and $(i, j-1/2)$ represent the top and bottom edges of the cell (i, j) , respectively. The unsteady term was discretized by a second order Runge-Kutta scheme, and then we got the first intermediate LS function $\phi^{n,\circ}$ after convection.

3. *Re-initialization of LS function ϕ .* Keeping ϕ a distance function closing to the interface is very important for accurately capturing the interface and evaluating the

surface tension force. Though the LS function ϕ is a signed distance function initially, it does not necessarily correspond to a distance function anymore after it is convected through a non-uniform flow (Van der Pijl et al., 2005). Thus, the re-initialization is employed to correct $\phi^{n,\circ}$ to be a distance function. Equation (3-15) can also be written in the form of

$$\frac{\partial \phi}{\partial \tilde{t}} + \vec{w} \cdot \nabla \phi = \text{sgn}(\phi^{\circ}), \quad (3-24)$$

where

$$\vec{w} = \frac{\nabla \phi}{|\nabla \phi|} \text{sgn}(\phi^{\circ}), \quad (3-25)$$

can be seen as the property propagation velocity having magnitude one and pointing away from the zero level set. As the distance property is only needed to retain in the region closing to interface ($=m\Delta x$, where m is an integer), we can just solve Eq. (3-24) for $\tilde{t} = 0, \dots, m\Delta x$. Eq. (3-24) has the form of a convection equation with velocity \vec{w} , so we used the second ENO scheme along with the second order Runge-Kutta scheme, as described above, to discretize the convective term and unsteady term, respectively. Note that in this MCLS method, after re-initialization, we didn't obtain the LS function at the new instant ϕ^n but the second intermediate LS function $\phi^{n,\circ}$, which requires to be corrected further to satisfy the mass conservation.

4. *Convection of VOF function F.* The VOF function at the $(n-1)$ -th instant F^{n-1} is determined by Eq. (3-16). F^n after convection during a time step Δt is found by considering the flux of fluid that flows through a boundary of a computational cell. As mentioned above, due to the discontinuity essence of VOF function, Eq. (3-13) cannot be discretized by traditional numerical schemes but geometrical treatment. Thus, F^n can be specified as

$$F_{i,j}^n = F_{i,j}^{n-1} - \frac{1}{\Delta x \Delta y} (\text{FLR}_{i,j} - \text{FLL}_{i,j} + \text{FLT}_{i,j} - \text{FLB}_{i,j}), \quad (3-26)$$

where $FLR_{i,j}$, $FLL_{i,j}$, $FLT_{i,j}$, and $FLB_{i,j}$ are the fluxes passing through the right, left, top and bottom edges of cell (i, j) , respectively. In the following, we will take an example of how to conduct calculation of flux through the left edge of the cell, and the others are calculated in the similar way. In order to include upwind property in the discrete convection equation of F , the flux through left edge can be considered the contribution from both neighbors, namely, FLL^+ and FLL^- , respectively. $FLL^+ \neq 0$ when $FLL^- = 0$ and vice versa. In this way, the flux can be written as

$$FLL_{i,j} = FLL_{i,j}^+ + FLL_{i,j}^-, \quad (3-27)$$

where the fluxes FLL^+ and FLL^- are computed by

$$FLL_{i,j}^+ = \Delta x \Delta y \int_{\xi=\frac{1}{2}-v^+}^{\frac{1}{2}} \int_{\eta=-\frac{1}{2}}^{\frac{1}{2}} H(\phi_L + D_{xL}\xi + D_{yL}\eta) d\xi d\eta, \quad (3-28)$$

and

$$FLL_{i,j}^- = -\Delta x \Delta y \int_{\xi=-\frac{1}{2}}^{\frac{1}{2}-v^-} \int_{\eta=-\frac{1}{2}}^{\frac{1}{2}} H(\phi_R + D_{xR}\xi + D_{yR}\eta) d\xi d\eta, \quad (3-29)$$

Where H is the Heaviside function, $\xi = (x - x_i) / \Delta x$, $\eta = (y - y_j) / \Delta y$, and

$$v^+ = \frac{\max(u_{i-1,j}, 0)\Delta t}{\Delta x}, v^- = \frac{\min(u_{i-1,j}, 0)\Delta t}{\Delta x}, \quad (3-30)$$

$$\phi_L = \phi_{i-1,j}, \phi_R = \phi_{i,j}, \quad (3-31)$$

and

$$D_{xL} = \Delta x \left. \frac{\partial \phi}{\partial x} \right|_{i-1,j}, D_{yL} = \Delta y \left. \frac{\partial \phi}{\partial y} \right|_{i-1,j}, D_{xR} = \Delta x \left. \frac{\partial \phi}{\partial x} \right|_{i,j}, D_{yR} = \Delta y \left. \frac{\partial \phi}{\partial y} \right|_{i,j} \quad (3-32)$$

With some scaling, these fluxes become

$$\begin{aligned} FLL_{i,j}^+ &= v^+ \Delta x \Delta y \cdot F_{i,j} \left(\phi_L + \frac{1}{2} (1 - v^+) D_{xL}, \left(\frac{1}{\Delta x} v^+ D_{xL}, \frac{1}{\Delta y} D_{yL} \right) \right) \\ FLL_{i,j}^- &= v^- \Delta x \Delta y \cdot F_{i,j} \left(\phi_R - \frac{1}{2} (1 + v^-) D_{xR}, \left(-\frac{1}{\Delta x} v^- D_{xR}, \frac{1}{\Delta y} D_{yR} \right) \right) \end{aligned} \quad (3-33)$$

This scaling of variables makes the convection of VOF rather straightforward, due to the function is given in Eq. (3-16). The other fluxes are obtained in the same way.

After obtaining the fluxes around four edges, in order to attain the VOF function at new time step, we will conduct a flux-splitting method due to its simplicity and realizability to 3D configuration.

$$\begin{aligned}
F_{i,j}^{\circ} &= \frac{F_{i,j}^{n-1} - \frac{1}{\Delta x \Delta y} (\text{FLR}_{i,j} - \text{FLL}_{i,j})}{1 - \frac{\Delta t}{\Delta x} (u_{i,j} - u_{i-1,j})} \\
F_{i,j}^{\circ\circ} &= \frac{F_{i,j}^{\circ} - \frac{1}{\Delta x \Delta y} (\text{FLT}_{i,j} - \text{FLB}_{i,j})}{1 - \frac{\Delta t}{\Delta y} (v_{i,j} - v_{i,j-1})} \\
F_{i,j}^n &= F_{i,j}^{\circ\circ} - \Delta t \left(F_{i,j}^{\circ} \frac{u_{i,j} - u_{i-1,j}}{\Delta x} + F_{i,j}^{\circ\circ} \frac{v_{i,j} - v_{i,j-1}}{\Delta y} \right)
\end{aligned} \tag{3-34}$$

It should be noticed that due to the geometric treatment to convection of VOF (Eq. (3-26)), the mass is conserved. However, due to the numerical errors, the overshoot or undershoot of the VOF value at new time step $F_{i,j}^n$ may still occur, which results in the unphysical value of $F_{i,j}^n$, namely, $F_{i,j}^n < 0$ or $F_{i,j}^n > 1$. In this dissertation, we will simply truncate the F -value at each cell, which only arise mass error of the order 10^{-4} in general (**Van der Pijl et al., 2005**). This truncation treatment is also adopted by other researchers in their VOF or CLSVOF calculations (**Nichols et al., 1980; Hirt and Nichols, 1981; Sussman and Puckett, 2000; Van der Pijl et al., 2005**).

5. *Iteration of inverse function for mass conservation.* When coupling the LS with VOF to conserve the mass, the inverse function of Eq. (3-16), $G_{i,j}(F_{i,j}, \nabla \phi_{i,j})$, is needed after LS convection and re-initialization and VOF convection. In other words, we needed to find $\phi_{i,j}^n$, which is the correction of the LS function after re-initialization $\phi_{i,j}^{n,\circ\circ}$, to satisfy

$$\max \left\{ \left| F_{i,j} \left(\phi_{i,j}^n, \nabla \phi_{i,j}^n \right) - F_{i,j}^n \right| \right\} \leq \varepsilon_0, \tag{3-35}$$

where ε_0 is some tolerance. $\phi_{i,j}^n$ can be determined by the following iteration. First, substitute the initial guess $\phi_{i,j}^{n,0} = \phi_{i,j}^{n,\infty}$ into Eq. (3-16) and if

$$\max \left\{ \left| F_{i,j} \left(\phi_{i,j}^{n,0}, \nabla \phi_{i,j}^{n,0} \right) - F_{i,j}^n \right| \right\} \leq \varepsilon_0, \quad (3-36)$$

the iteration is ceased and $\phi_{i,j}^n = \phi_{i,j}^{n,\infty}$. If Eq. (3-36) is not satisfied, then let

$$\phi_{i,j}^{n,p} = G_{i,j} \left(F_{i,j}^n, \nabla \phi_{i,j}^{n,p-1} \right), (p = 1, 2, \dots), \quad (3-37)$$

where

$$G_{i,j} \left(F_{i,j}, \nabla \phi_{i,j} \right) = \begin{cases} -\phi_{\max}, & F_{i,j} \leq 0 \\ \sqrt{2F_{i,j} \left(\phi_{\max i,j}^2 - \phi_{i,j}^2 \right)} - \phi_{\max}, & 0 < F_{i,j} < F_{\text{mid}} \\ \left(F_{i,j} - 0.5 \right) \left(\phi_{\max i,j} + \phi_{\text{mid } i,j} \right), & F_{\text{mid}} \leq F_{i,j} \leq 1 - F_{\text{mid}}, \\ -\sqrt{2 \left(1 - F_{i,j} \right) \left(\phi_{\max i,j}^2 - \phi_{i,j}^2 \right)} + \phi_{\max}, & 0 < F_{i,j} < F_{\text{mid}} \\ \phi_{\max}, & F_{i,j} \geq 1 \end{cases} \quad (3-38)$$

and

$$F_{\text{mid}} = \frac{1}{2} \frac{\phi_{\max} + 3\phi_{\text{mid}}}{\phi_{\max} + \phi_{\text{mid}}}. \quad (3-39)$$

The iteration is repeated until

$$\max \left\{ \left| F_{i,j} \left(\phi_{i,j}^{n,p}, \nabla \phi_{i,j}^{n,p} \right) - F_{i,j}^n \right| \right\} \leq \varepsilon_0 \quad (3-40)$$

is satisfied. Then, $\phi_{i,j}^n = \phi_{i,j}^{n,p}$. In this dissertation, we set the tolerance $\varepsilon_0 = 10^{-8}$. The whole logic of the algorithm of MCLS is shown in Fig. 3-6.

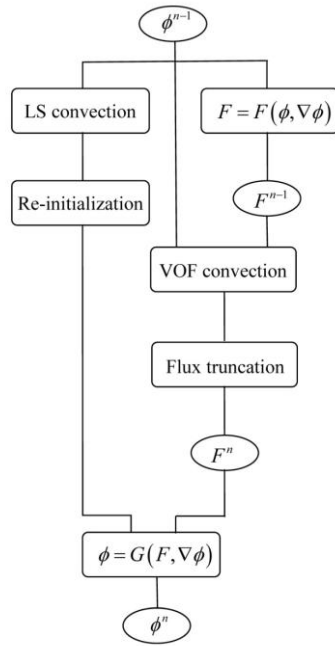


Fig. 3-6 Flow chart of the procedures of MCLS method.

Chapter 4

Mechanism of ligament formation by Faraday instability

In this chapter, the basic mechanism of the ligament formation from a liquid layer due to Faraday instability is demonstrated based on the detailed information on the pressure and velocity fields. We first concisely review the linear theory derived by **Benjamin and Ursell (1954)** in the inviscid approximation to introduce the system parameters mentioned in Chapter 2. Then, we validate the codes utilizing the numerical methods described in Chapter 3 by comparing the linear theory and other's numerical works on Faraday instability under the same conditions. Finally, we present the detailed dynamics associated with the large surface deformation (ligament formation).

4.1 Mathieu equation

Consider a liquid layer resting horizontally on a substrate subject to a vertical vibration of standard sinusoidal displacement $\Delta_0 \sin(\Omega t)$, where Δ_0 is the amplitude of the vibration displacement and Ω is the angular frequency. Any surface deformation can be expressed by a Fourier series in the horizontal coordinate x . Each Fourier component $\delta(t) \sin(kx)$ is independent of others in the linear regime. In the linear regime, the amplitude $\delta(t)$ obeys the Mathieu equation

$$\frac{d^2 \delta}{d\tau^2} = (X \sin \tau - Y) \cdot \delta, \quad (4-1)$$

where $\tau = \Omega t$. The linear stability of the liquid layer is determined by two parameters X and Y defined as

$$X = k \Delta_0 \tanh(ky_0) \text{ and } Y = \left(\frac{\omega}{\Omega} \right)^2 = \frac{\sigma k^3 \tanh(ky_0)}{\rho_l \Omega^2}, \quad (4-2)$$

where y_0 is the depth of the liquid layer, σ is the surface tension coefficient and ρ_1 is the liquid density. Physically, X represents the destabilizing inertial effect, while Y represents the stabilizing capillary effect. For each parameter pair (X, Y) , we obtain a solution of the surface deformation amplitude $\delta(t)$, from the behavior of which we can find whether the motion of free surface is stable or not and the response of surface oscillation is sub-harmonic, harmonic or higher-order harmonic. The instability conditions derived from this linear theory are charted in Fig. 4-1 as the hatched regions.

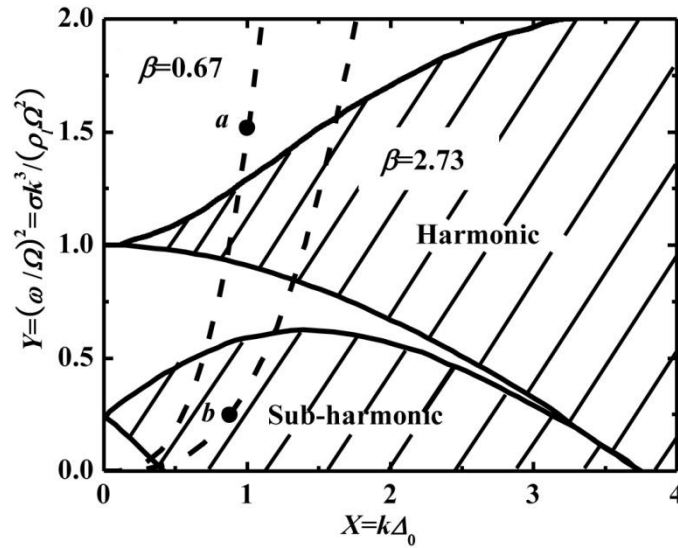


Fig. 4-1 Instability regions (hatched regions) for the Mathieu equation. Whether the surface waves are stable or not depends on the parameter pair (X, Y) . In the harmonic regime, the resulting surface wave frequency is equal to the vibration frequency Ω , while in the sub-harmonic regime, the resulting surface wave frequency is equal to one half the vibration frequency Ω . Each dashed curve $Y = X^3 / \beta$ corresponds to one vibration strength characterized by the dimensionless parameter $\beta = \rho_1 \Delta_0^3 \Omega^2 / \sigma$. The two symbols labeled as “a” and “b” correspond to the parameter pairs $(X=1, Y=1.5)$ and $(X=0.88, Y=0.25)$, respectively, which are the cases used for numerical validation conducted in §4.2.

An experiment with certain values of vibration displacement amplitude and frequency (Δ_0, Ω) can be demonstrated as a cubic curve in Fig. 4-1 by eliminating k from Eq. (4-2). Under the assumption $\tanh(ky_0) \rightarrow 1$, the curve is expressed as

$$Y = X^3 \left(\frac{\sigma}{\rho_1 \Delta_0^3 \Omega^2} \right) = \frac{X^3}{\beta}, \quad (4-3)$$

where $\beta = \rho_1 \Delta_0^3 \Omega^2 / \sigma$ is the cube of the dimensionless forcing acceleration amplitude in conventional terminology, which characterizes the vibration strength. All the unstable wave-numbers that can lead to the ligament formation under this vibration strength ought to be located on this curve in the instability regions. The ultrasonic atomization experiments have shown that the mean diameter of atomized droplets is related to the frequency according to $d_m \cong 0.34\lambda \sim c(1/\Omega)^{2/3}$ (**Lang, 1962; Donnelly et al., 2004**), where c is a constant when liquid properties are specified. This indicates that there exists one predominant wavelength $\lambda = 2\pi/k$ of the surface deformation for each vibration strength. Therefore, it is enough if we conduct a typical single wave-number calculation for a certain Weber number as a prototype to illustrate the basic dynamics. The appropriate calculation domain to be used is illustrated in Fig. 3-1 for 2D configuration.

4.2 Numerical validation

To validate the performances of our numerical code utilizing the methods described above on simulating the major dynamics associated with the Faraday instability, we compare the numerical results with the linear theory which is valid when the surface deformation is small compared with the wavelength and with others' numerical works under the same conditions.

We first conducted a linear regime calculation to be compared with the linear prediction (**Benjamin and Ursell, 1954**). When the initial disturbance imposed on the surface is small and the parameter pair (X, Y) is located in a stable region, the amplitude of the surface deformation is retained within a small magnitude (**Wright et al., 2000**). We considered the case $(X=1, Y=1.5)$ and $y_0 = \lambda$, corresponding to the real physical conditions: $\rho_1 = 1000 \text{ kg/m}^3$, $\rho_g = 20 \text{ kg/m}^3$, $\sigma = 0.072 \text{ N/m}$, $\Omega = 6.28 \times 10^6 \text{ rad/s}$ ($f = 1 \text{ MHz}$), $\lambda = 6.71 \text{ }\mu\text{m}$, $\Delta_0 = 1.07 \text{ }\mu\text{m}$ and $\beta = 0.67$, which is denoted by the label "a" in Fig. 4-1. Fig. 4-2 presents the temporal evolution of the calculated surface displacement at $x = \lambda/4$ by open circles. The time is normalized by the vibration period $T = 2\pi/\Omega$ and the surface displacement is normalized by the wavelength λ . The solid line shows the solution of Eq. (4-1), which was numerically integrated by the

fourth-order Runge-Kutta method. It can be seen from Fig. 4-2 that the calculation result agrees satisfactorily with the linear prediction. The small deviation comes from the evaluation error of the surface position in the CLSVOF, in which the interface is implicitly defined as the null LS function $\phi=0$ in the grid system of mesh size $\lambda/64$. Further refining the mesh size diminished the deviation.

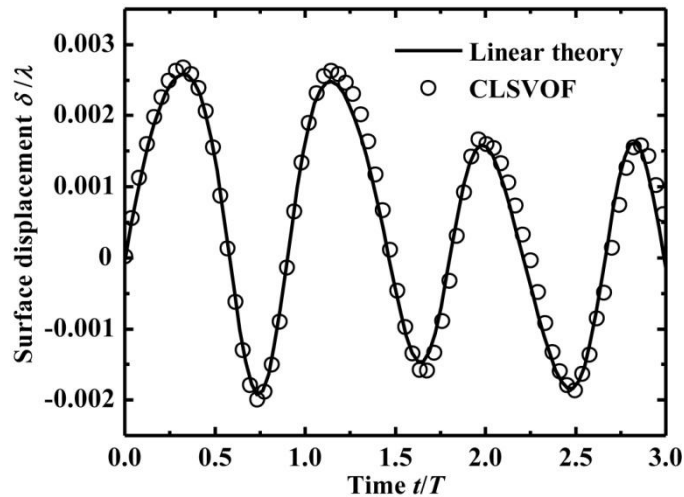


Fig. 4-2 Temporal evolution of the surface displacement at $x=\lambda/4$ obtained by the CLSVOF calculation (open circles) in comparison with the solution of Mathieu equation (solid curve) for the case ($X=1, Y=1.5$) represented by the label “a” in Fig. 4-1.

Our objective in this chapter is the mechanism of the ligament formation, which is typically accompanied by large surface deformation. Thus, the validation of code for the large surface deformation is necessitated. Since we only consider one wavelength for each calculation, direct comparison with experimental results is difficult. We treated the case ($X=0.88, Y=0.25$), and $y_0 = \lambda$, denoted by the label “b” in Fig. 4-1, which was also simulated by **Wright et al. (2000)** with the vortex-sheet method in two dimensions, except that their vibration phase is $3T/4$ advanced than mine. We compared our simulated result with theirs. The physical conditions are $\rho_l = 1000 \text{ kg/m}^3$, $\rho_g = 20 \text{ kg/m}^3$, $\sigma = 0.072 \text{ N/m}$, $\Omega = 6.28 \times 10^6 \text{ rad/s}$ ($f=1 \text{ MHz}$), $\lambda = 12.19 \text{ }\mu\text{m}$, $\Delta_0 = 1.71 \text{ }\mu\text{m}$ and $\beta = 2.73$. Fig. 4-3 (a) presents the temporal evolution of the surface displacement at $x=3\lambda/4$, where ligament is eventually formed. The surface deformation response is sub-harmonic and the overall tendency is the same in both calculations. It can be seen that the calculation results by CLSVOF accord with the

results of **Wright et al. (2000)** well quantitatively if the vibration phase is shifted as shown in Fig. 4-3 (b). The deviation observed near the calculation end is due to the failure of numerical calculation in the vortex-sheet simulation when breakup occurs (**Wright et al., 2000**).

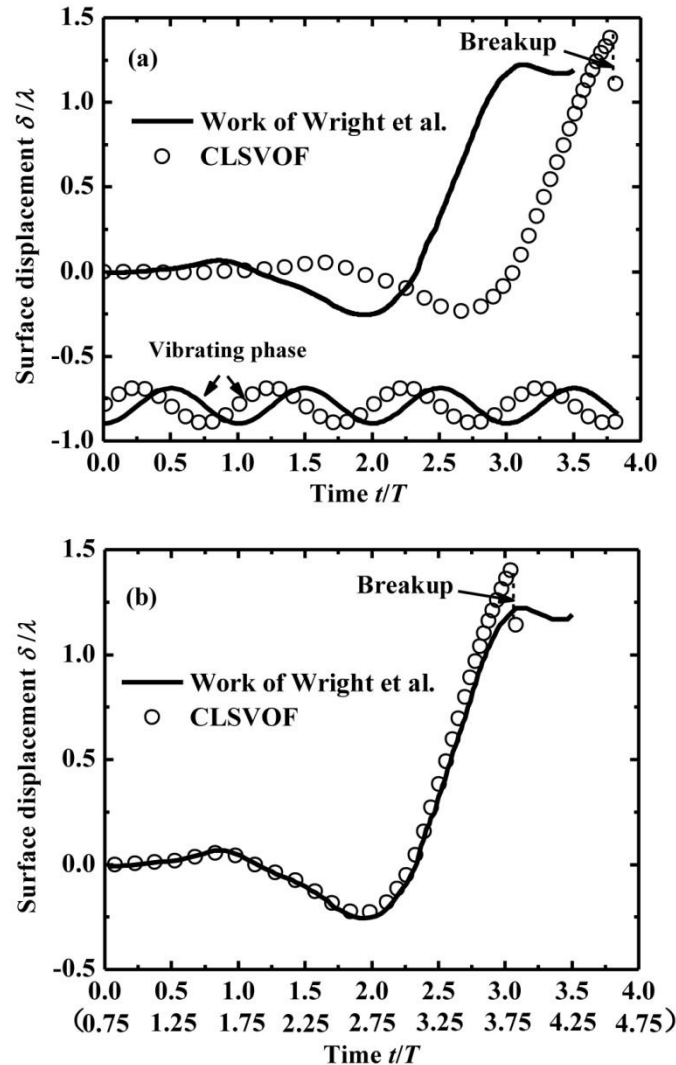


Fig. 4-3 Temporal evolution of the surface displacement at $x=3\lambda/4$ obtained by the CLSVOF calculation (open circle) in comparison with the simulation results of (**Wright et al., 2000**) (solid curve) for the case ($X=0.88, Y=0.25$) represented by the label “*b*” in Fig. 4-1. Panel (b) is the same comparison as (a) by shifting the vibration phase. The tick labels in the parenthesis denote the time in the CLSVOF calculation.

4.3 Dynamics of ligament formation

Although most of the past numerical calculations focused on the surface deformation, it is more important to study the liquid-phase flow field in detail to figure out the physical dynamics underlying the ligament formation. Ultrasonic

atomization experiments have shown that the frequency of the excited surface wave is equal to one half the vibration frequency (**Lang, 1962; Donnelly et al., 2004**). Therefore, we are especially interested in a typical ligament formation process appearing in the sub-harmonic instability condition in Fig. 4-1. As a prototype case, we considered the case ($X=0.9, Y=0.3$), and $y_0 = \lambda$, corresponding to the real physical conditions: $\rho_l = 1000 \text{ kg/m}^3$, $\rho_g = 20 \text{ kg/m}^3$, $\sigma = 0.072 \text{ N/m}$, $\Omega = 1.27 \times 10^7 \text{ rad/s}$ ($f = 2 \text{ MHz}$), $\lambda = 7.20 \text{ }\mu\text{m}$, $\Delta_0 = 1.04 \text{ }\mu\text{m}$ and $\beta = 2.47$. The initial disturbance on the surface is imposed as $v_s = v_{s0} \sin(kx)$ with the amplitude $v_{s0} = 0.03\Delta_0\Omega$. This situation is close to the experimental observation by **Donnelly et al. (2004)**, in which the mean diameter of produced aerosol for water is $2.61 \text{ }\mu\text{m}$ ($= (0.35 \pm 0.03)\lambda$) at $f = 1.95 \text{ MHz}$. The calculation conditions including the case of harmonic instability and very large vibration amplitude were also treated in this study. They showed the common flow structure in the process of ligament formation. Therefore, the detailed dynamics of the ligament formation are mainly discussed based on the above-mentioned prototype.

For convenience, the “destabilizing phase” will be called when the factor at the right hand side of Eq. (4-1) $(X \sin \tau - Y) > 0$, because the destabilizing effect due to the positive inertial force overwhelms the stabilizing effect due to the capillarity, and “stabilizing phase” will be called when $(X \sin \tau - Y) < 0$. For the prototype case with parameter pair ($X=0.9, Y=0.3$), the destabilizing phase refers to a period $(0.055+n)T < t < (0.445+n)T$, where $n = 0, 1, 2, \dots$

4.3.1 Results of the surface evolution

Fig. 4-4 shows the evolving liquid surface shapes and the liquid velocity vectors viewed in the laboratory reference frame. The calculation starts at the instant when the bottom substrate moves upward from the middle position and ends when the ligament disintegrates at its tip ($t=3.65T$). During the initial stage until $t=2.0T$, the surface deformation that is initiated by the small surface disturbance at $t=0$ increases but its magnitude is small, thus the evolution of the surface deformation is consistent with the linear theory, as can be seen in Fig. 4-5, which presents the temporal evolutions of the surface displacement at $x=3\lambda/4$ obtained by the linear theory and the CLSVOF calculation.

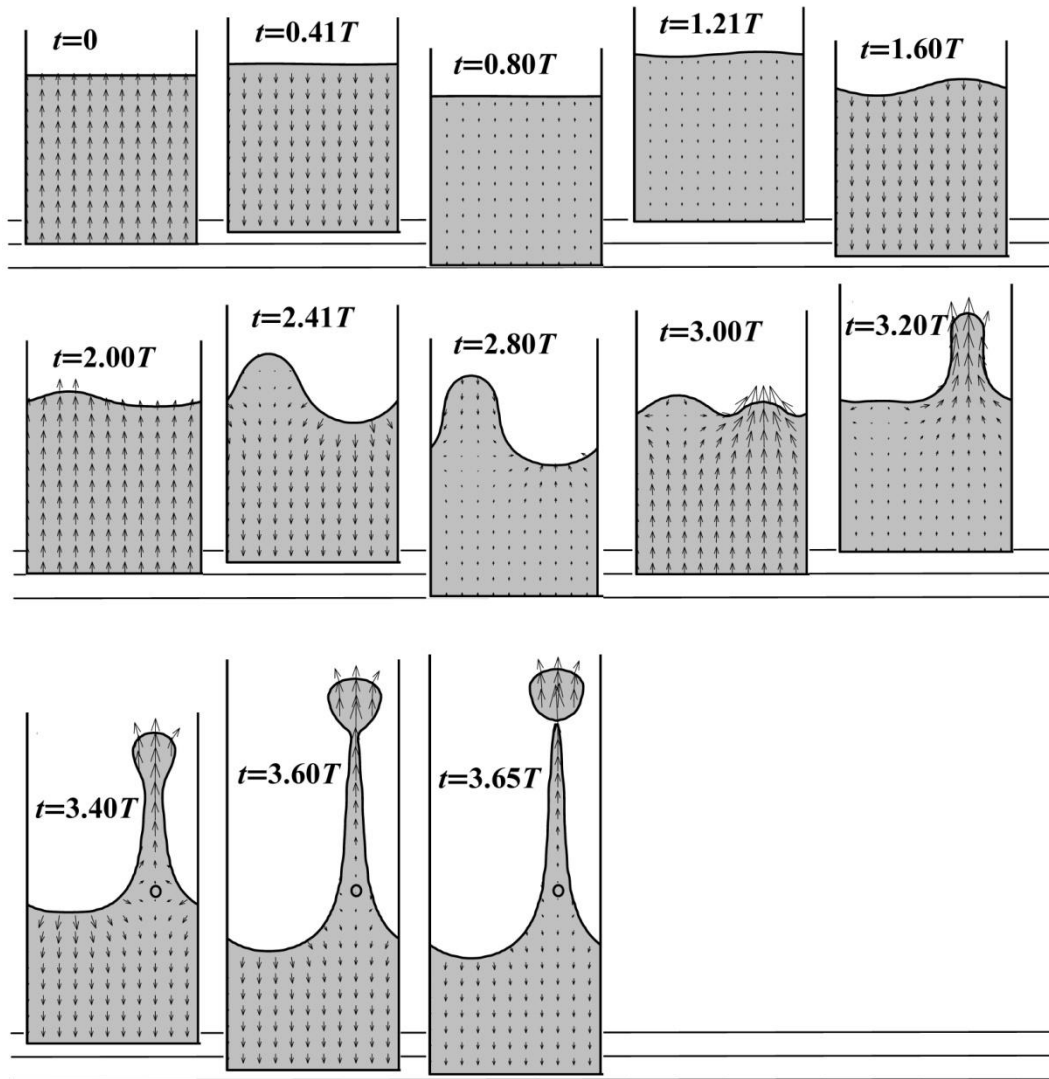


Fig. 4-4 Temporal evolution of the liquid surface shapes and the velocity vectors viewed in the laboratory reference frame for the case ($X=0.9$, $Y=0.3$) and $y_0 = \lambda$. The gray region represents the liquid while the white represents the gas. The velocity vectors are shown every six cells in both x - and y -direction for clarity. The three horizontal lines drawn in each row of figures denote the top limit position, middle position and bottom limit position of the vibrating substrate. The open circle shown after $t=3.40T$ denotes the instantaneous stationary point where the velocity vanishes in the laboratory reference frame.

After $t=2.0T$, the surface deformation becomes large, and the nonlinearity deviates the calculation result from the linear theory. The calculated increase of the surface displacement is abated and delayed compared with the linear prediction (see Fig. 4-5). Moreover, according to the linear theory, the direction of surface deformation continues to alternate periodically as time elapses no matter how large the amplitude is. However, in the calculation, the ligament disintegrating into droplet is formed. The

broken droplet moves outward and never falls back because it holds a large outward vertical velocity in the laboratory reference frame as shown at $t=3.65T$ in Fig. 4-4. In the following sections, we will discuss the detailed dynamics during the ligament forming process, especially the nonlinear effects that result in the slender freed ligament.

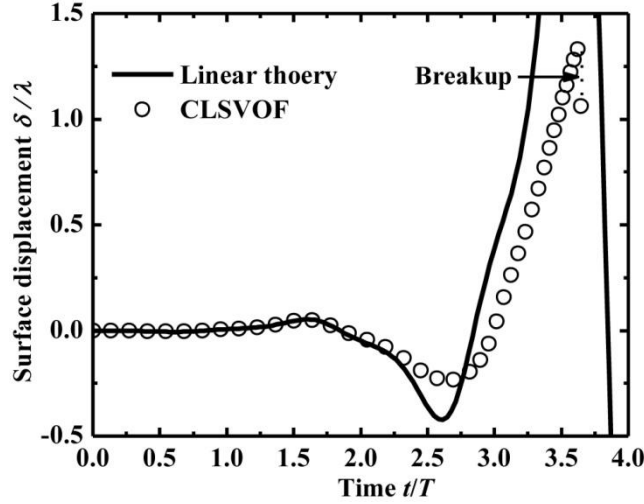


Fig. 4-5 Temporal evolution of the surface displacement at $x=3\lambda/4$ obtained by the CLSVOF calculation (open circles) in comparison with the solution of Mathieu equation (solid curve) for the case ($X=0.9, Y=0.3$) and $y_0 = \lambda$.

4.3.2 Destabilizing mechanism at the linear stage

The dynamics of the liquid layer during the destabilizing phase of the linear stage are easily understood qualitatively. Consider that the liquid layer has a simple step-like surface shape, as shown in Fig. 4-6, in which the crest and trough portions are periodically repeated at wavelength intervals of $2\pi/k$ along the substrate. When the inertial force is directed upward (destabilizing phase), the pressure in the crest portion becomes lower than that in the trough portion at the same level. This pressure difference due to surface deformation exists only in the region near the surface. Thus, the region influenced by periodic surface deformation is, by phase mixing, restricted to a limited distance of $\sim 1/k$ from the surface. If the liquid layer is thick enough ($> 1/k$), then the pressure at the bottom should be uniform for the crest (p_R) and trough portions (p_L), *i.e.*, $p_R = p_L < 0$. The pressure difference near the surface induces liquid flow from the trough portion to the crest portion during every

destabilizing phase. If this pressure difference is large enough to overcome the restoring capillary force, then the surface deformation will be enhanced, which strengthens the flow from the trough to the crest. This is the mechanism of linear instability, which dominates in the initial stage when the surface deformation is small.

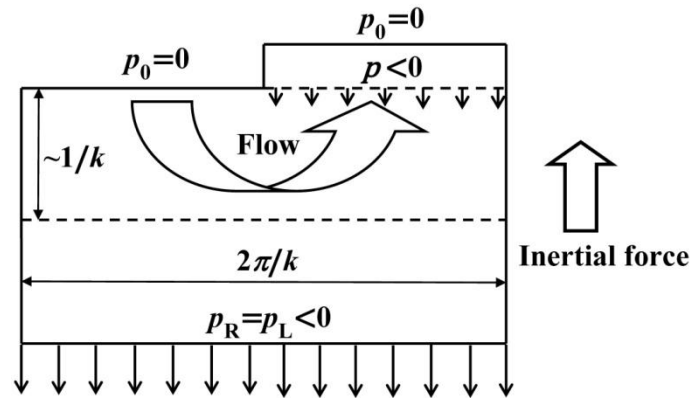


Fig. 4-6 A simple physical model for the linear instability mechanism of the Faraday wave. The surface shape changes periodically at an interval of $2\pi/k$ along the substrate. The arrows represent the pressure distribution.

4.3.3 Ligament structure

For the purpose of the present study, we have to understand well that a ligament formed from the surface is a result of the nonlinear effect. This can be achieved by examining the dynamic structure of the largely deformed liquid layer in detail. Fig. 4-7 shows the pressure and vertical velocity distributions along the trough center line and the crest center line during the time span when the liquid surface deforms largely. Considering the flow structure difference, we divide the crest portion into three regions I, II and III as shown in Fig. 4-8. In the following text we will discuss the dynamics in these three regions in detail.

Region I: in the vicinity of the bottom substrate

For the thick layer case ($y_0 = \lambda > 1/k$), since the flow associated with the surface deformation is restricted within a limited distance from the surface, the magnitude of the velocity relative to the bottom substrate is small in Region I, and the linear theory should be recovered. According to the linear theory, the y -dependence of the vertical velocity follows $v(y) \propto \sinh(ky)$. Thus, between the bottom substrate and the surface,

there exists a region where $v(y)$ obeys the exponential law $v(y) \propto \exp(ky)$ or $\lg[v(y)] \propto k \lg e \cdot y$ if the liquid layer is thick enough.

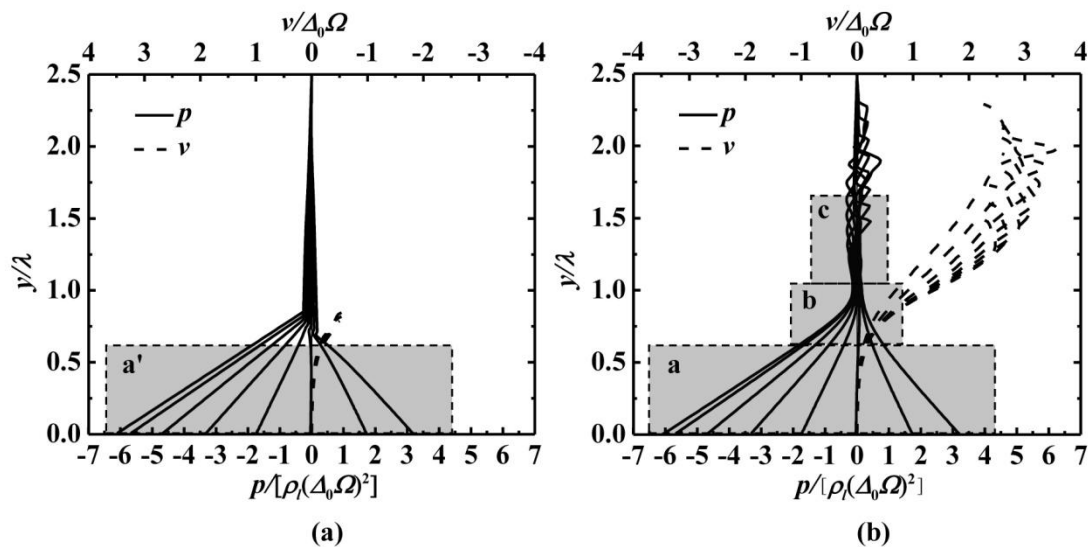


Fig. 4-7 Pressure and vertical velocity distributions along (a) the trough center line and (b) the crest center line during the time span from $t=3.25T$ to $t=3.60T$ when the liquid surface deforms largely. The enlargements of the pressure distributions enclosed by the dashed rectangles will be shown in Fig. 4-8.

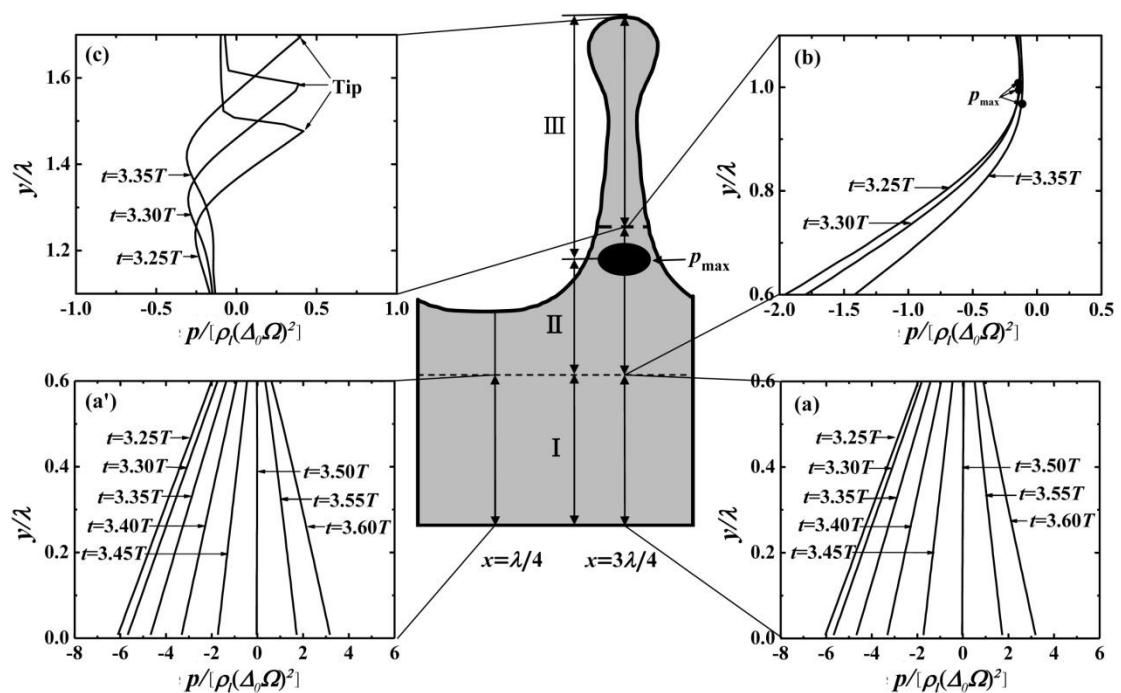


Fig. 4-8 Division of the ligament structure into Regions I, II and III and the enlargements of the pressure distributions in Fig. 4-7. Panels (a'), (a), (b) and (c) correspond to the dashed rectangles a', a, b and c in Fig. 4-7, respectively.

Fig. 4-9 depicts the vertical velocity distribution at $t=3.00T$, $t=3.25T$ and $t=3.50T$ at

$x=3\lambda/4$ where the center line of the crest portion is located. The three instants in Fig. 4-9 are all in the ligament forming process accompanied with large surface deformation. The abscissa is on a logarithmic scale. The straight line with slope $k \lg e$ is also drawn for reference. The numerical results in the region where the linearization assumption is valid agree well with the linear prediction. It is confirmed that, even though the surface deformation is large, there still exists a layer on the bottom substrate, where the linear theory dominates, so far as the liquid layer is thick enough. This layer has no significant effect on the dynamics of ligament formation. However, the thickness of Region I becomes thinner as time elapses, because the nonlinear effects spread to the lower portion of the liquid layer as the trough surface moves down.

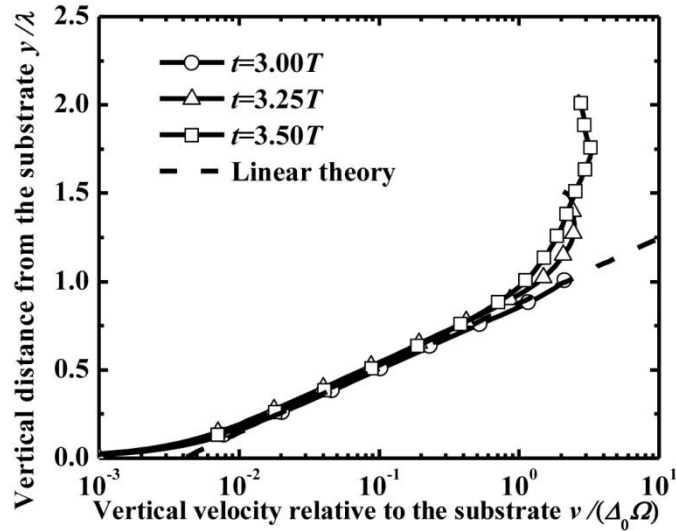


Fig. 4-9 Distribution of the vertical velocity relative to the bottom substrate along the crest center line ($x=3\lambda/4$) at three instants. The velocity is relative to the bottom substrate. The dashed line represents the exponential distribution derived from linear theory.

Region II: in the vicinity of the ligament root

In Region II, a local maximum pressure location is formed as shown in Fig. 4-8 (b), which is important for ligament formation. We first consider a thin layer case ($y_0 = \lambda/4$) which is more convenient to explore the dynamics. Later, an extended analysis to the thick layer case ($y_0 = \lambda$) will be presented.

a. *Thin layer case*

In the thin layer case, the horizontal slip velocity allowable on the substrate surface may take a value comparable to the horizontal surface velocity component in magnitude, so that we can easily identify the two stagnation point locations B and C on the bottom substrate as illustrated in Fig. 4-10. The temporal evolutions of these stagnation point locations are shown in Fig. 4-11, indicating that the location of the streamline trace ABCDE is fixed in space to a good degree.

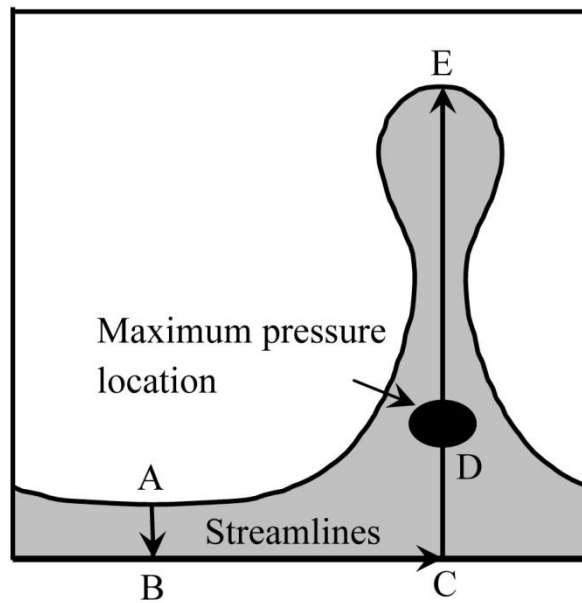


Fig. 4-10 Streamline passing through two stagnation points B and C in the thin layer case $y_0 = \lambda/4$. The location of streamline ABCDE is fixed in space as shown in Fig. 4-11.

In the vicinity of point C, the velocity can be evaluated as

$$u = -E(t) \cdot (x - 0.75\lambda), v = E(t) \cdot y, \quad (4-4)$$

where $E(t)$ is the strain rate. Substituting Eq. (4-4) into Euler equations around point C we obtain

$$\rho_1 \left(\frac{dE}{dt} + E^2 \right) y = -\frac{\partial p}{\partial y} + \rho_1 A, \quad (4-5)$$

and

$$\rho_1 \left(\frac{dE}{dt} + E^2 \right) (x - 0.75\lambda) = -\frac{\partial p}{\partial x}, \quad (4-6)$$

where $A = A_0 \Omega^2 \sin(\Omega t)$. Integrating Eq. (4-5) with respect to y from point C leads to

$$P(y, t) = p_C(t) + \rho_1 A y - \frac{1}{2} \rho_1 \left(\frac{dE}{dt} + E^2 \right) y^2, \quad (4-7)$$

where $P(y, t)$ is the instantaneous pressure on the crest center line and $p_C(t)$ is the pressure at the stagnation point C. Similarly, integrating Eq. (4-6) with respect to x leads to

$$p(x, y, t) = P(y, t) - \frac{1}{2} \rho_1 \left(E^2 - \frac{dE}{dt} \right) (x - 0.75\lambda)^2. \quad (4-8)$$

Therefore, the pressure in the vicinity of point C is

$$p(x, y, t) = p_C(t) + \rho_1 A y + \frac{1}{2} \rho_1 \frac{dE}{dt} \left[(x - 0.75\lambda)^2 - y^2 \right] - \frac{1}{2} \rho_1 E^2 \left[(x - 0.75\lambda)^2 + y^2 \right]. \quad (4-9)$$

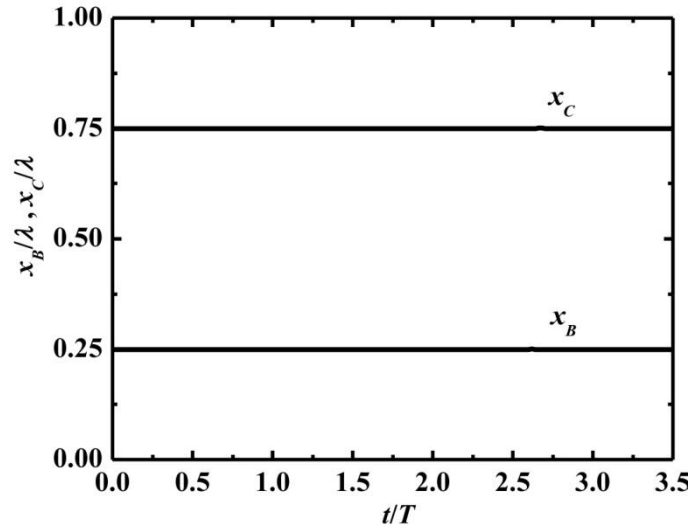


Fig. 4-11 Temporal evolutions of the left (B) and right (C) stagnation point locations for the thin layer case $y_0 = \lambda / 4$.

From the third and fourth terms on the right hand side of Eq. (4-9), we can distinguish two types of stagnation-point flow as shown in Fig. 4-12. The streamlines in the two types are the same, but the pressure distributions are totally different. The

linear solution for which E^2 takes a negligibly small value provides us the stagnation-point flow of type A only (depicted in Fig. 4-12 (a) and called “linear stagnation-point flow”). The isobaric lines obtained from the third term on the right hand side of Eq. (4-9) are hyperbolic curves. In the destabilizing phase, the decrease in pressure at the crest root (located above the point C), whose magnitude is proportional to the crest height, sucks the surrounding liquid and increases the crest height. The increased crest height further lowers the crest root pressure. This is the mechanism causing the linear instability discussed in §4.3.2, which dominates at the early stage of crest development.

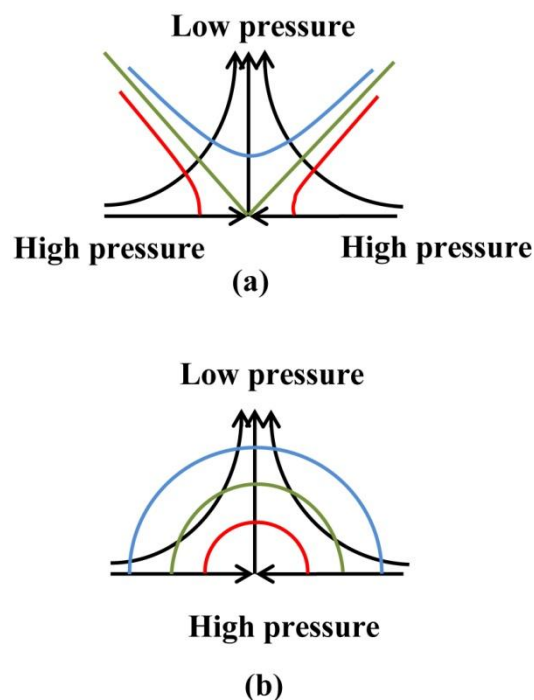


Fig. 4-12 Two types of stagnation-point flow around point C in Fig. 4-10: (a) linear stagnation-point flow and (b) nonlinear stagnation-point flow. The streamlines represented by arrowed lines are the same in both types, but the isobaric lines are hyperbolic curves for (a) and concentric circles for (b).

However, the nonlinear effect (contribution of the convective terms in Eqs. (4-5) and (4-6)) is not negligible when the magnitude of flow velocity is increased. Then, the stagnation-point flow of type B (depicted in Fig. 4-12 (b) and called “nonlinear stagnation point flow”) becomes dominant gradually. As a result, the pressure at the crest root tends to increase and suppresses the suction effect, which changes the exponential crest-height increase with time in the linear regime to the almost linear crest-height increase with time in the nonlinear regime, as seen in Fig. 4-5. The

mechanism of ligament formation can be understood as the pressure enhancement caused by the stagnation-point flow of type B, which is going to be discussed.

At $x=0.75\lambda$, Eq. (4-9) can be written as

$$p(x, y, t)\Big|_{x=0.75\lambda} = p_C(t) + \rho_1 A y - \frac{1}{2} \rho_1 \left(E^2 + \frac{dE}{dt} \right) y^2. \quad (4-10)$$

Along the crest center line, the pressure gradient $\partial p/\partial y$ is given by

$$\frac{\partial p(x, y, t)}{\partial y}\Big|_{x=0.75\lambda} = \rho_1 A - \rho_1 \left(E^2 + \frac{dE}{dt} \right) y. \quad (4-11)$$

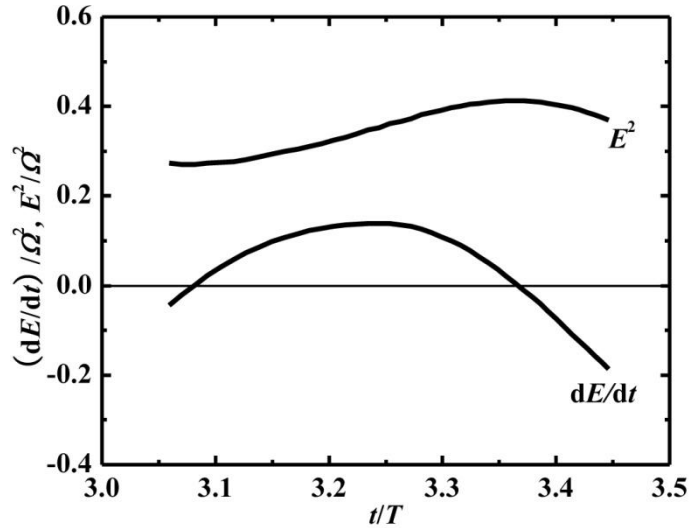


Fig. 4-13 Temporal evolutions of E^2 and dE/dt during the destabilizing phase from $t=3.055T$ to $t=3.445T$.

Fig. 4-13 shows the temporal evolutions of dE/dt and E^2 during the destabilizing phase from $t=3.055T$ to $t=3.445T$. From Eq. (4-11) it can be seen that, once both g' and $(E^2 + dE/dt)$ become positive, there appears a position y_D (corresponding to point D in Fig. 4-10) where the pressure is maximized. y_D is given by

$$y_D = \frac{A}{E^2 + \frac{dE}{dt}}. \quad (4-12)$$

At the early stage of destabilizing phase, y_D calculated from Eq. (4-12) is larger than the crest height due to dE/dt and E^2 being small. Thus, this local maximum pressure

location does not emerge at the early stage of destabilizing phase. When y_D becomes smaller than the crest height, the maximized pressure location can be observed. Fig. 4-14 compares the value of y_D evaluated from Eq. (4-12) with that from the simulation results after the maximum pressure location emerges, which shows a good consistence between them.

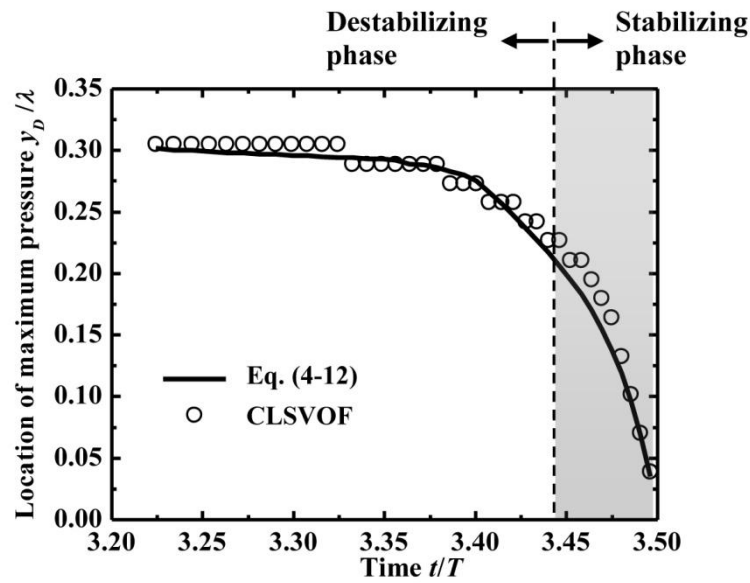


Fig. 4-14 Local maximum pressure location y_D evaluated from Eq. (4-12) in comparison with the simulation results in the thin layer case ($y_0 = \lambda/4$). The existence of the maximum pressure locations in the gray region indicates that the ligament keeps developing at the early stage of the next stabilizing phase.

The local maximum pressure location emerging at the crest root indicates that the pressure gradient vanishes there ($\partial p / \partial y = 0$). This means that the liquid between point D and the tip is dynamically free from the motion of the bottom substrate in the laboratory reference frame. In other words, the freed liquid region may have a chance to be released from the recovering motion of the liquid layer in the next stabilizing phase and exhibits a totally different behavior from the amplified crest described by the linear theory, in which no dynamically freed region from the substrate can be formed and the crest is always pulled back. As time elapses, the maximum pressure location moves downwards (see Fig. 4-14) and the new liquid elements passing through the maximum pressure location and entering the freed region will further

enlarge the freed liquid region and result in a slender liquid ligament. This describes the essential feature of how the ligament is formed and defines the necessary condition for the ligament formation as the emergence of the local maximum pressure location.

b. Thick layer case

In the thick layer case ($y_0 = \lambda$), the streamline coincident with the bottom substrate is not useful to characterize the Faraday wave flow because it is located outside of the region where the liquid flow is effectively associated with the surface deformation. However, similar arguments to those in the thin layer case can be made as follows.

Fig. 4-15 shows the distributions of the velocity gradient $\partial v/\partial y$ and the pressure along the crest center line. It can be seen that the velocity gradient maximizes at a location $y_v(t)$ around the crest root, where the pressure may be enhanced greatly due to the collision of liquid flowing from both sides. This pressure enhancement can be demonstrated in the following way. We set the numerical data attained at $t=3.40T$ as the initial condition but the inertial force to be zero. After one time step, we obtain the pressure distribution as shown in Fig. 4-16, which excludes the effect of inertial force and is totally determined by the instantaneous liquid flow at that instant. It is apparent that the pressure enhancement at the crest root is caused by the impinging flow which significantly contributes to the convection terms.

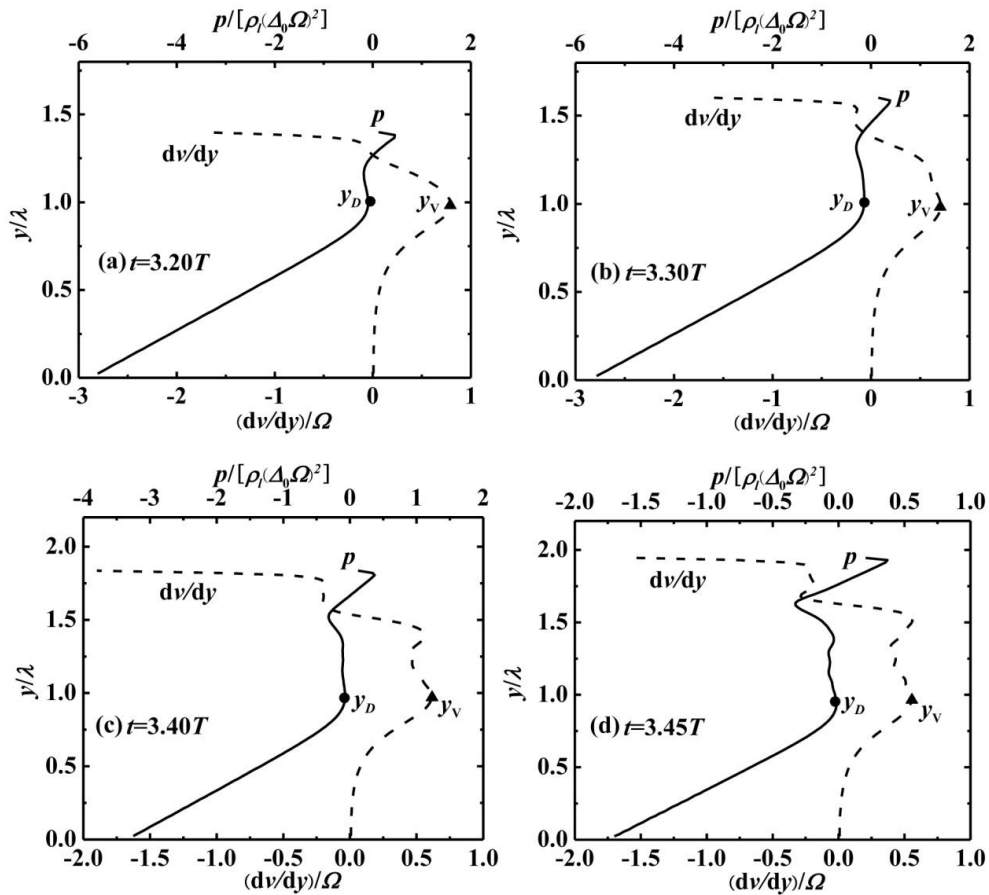


Fig. 4-15 Distributions of the velocity gradient $\partial v / \partial y$ (dashed lines) and pressure (solid lines) along the crest center line at (a) $t=3.20T$, (b) $t=3.30T$, (c) $t=3.40T$, and (d) $t=3.45T$. The maximum pressure location y_D is always near the maximum velocity gradient location y_V .

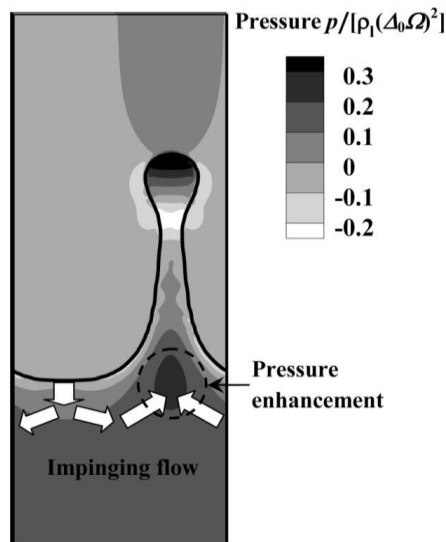


Fig. 4-16 Pressure distribution caused by an instantaneous flow. This figure is obtained by an artificial calculation to explain that the pressure enhancement at the crest root (dashed circle) is caused by the impinging flow (white arrows) from the neighboring trough portion.

From Fig. 4-15 we can see that the maximum pressure is always located around $y_v(t)$. Using the continuity equation, the horizontal velocity in the vicinity of $x = 0.75\lambda$ can be expressed as

$$u(x, y, t) = -\frac{\partial v}{\partial y}\bigg|_{x=0.75\lambda} (x - 0.75\lambda). \quad (4-13)$$

Furthermore, in the vicinity of $y_v(t)$ where $\partial v/\partial y$ maximizes, the vertical velocity gradient and velocity are expressed as $E(t) = \partial v/\partial y|_{x=0.75\lambda, y=y_v(t)}$ and $v = v_Y + E \cdot (y - y_v)$, respectively, where $v_Y(t) = v|_{x=0.75\lambda, y=y_v(t)}$. Then similar to the derivation of Eq. (4-9), we can derive the expression of pressure around $y_v(t)$ as

$$p(x, y, t) = p_Y(t) + \rho_1(y - y_v) \left[A - \left(\frac{dv_Y}{dt} - E \frac{dy_v}{dt} + E v_Y \right) \right] + \frac{1}{2} \rho_1 \frac{dE}{dt} \left[(x - 0.75\lambda)^2 - (y - y_v)^2 \right] - \frac{1}{2} \rho_1 E^2 \left[(x - 0.75\lambda)^2 + (y - y_v)^2 \right], \quad (4-14)$$

where $p_Y(t) = p|_{x=0.75\lambda, y=y_v(t)}$.

Equation (4-14) is different from Eq. (4-9) by an addition of the second term on the right hand side. The location of maximum pressure can be formulated as

$$y_D = \frac{A - \left(\frac{dv_Y}{dt} - E \frac{dy_v}{dt} + E v_Y \right)}{E^2 + \frac{dE}{dt}} + y_v. \quad (4-15)$$

Considering that the free ligament is formed by the collision of the liquid flowing at a high speed from both sides, the physics described here may apply to the splash formation problem treated by **Josserand and Zaleski (2003)**, in which no such detailed considerations mentioning the delivery of a liquid sheet from the colliding liquid body have been provided by far.

Region III: freed ligament region

The detailed development of the ligament region above the local maximum

pressure location (Region III) can be more easily understood by expressing the vertical velocity distribution along the crest center line viewed in the laboratory reference frame (v_a) for the thick layer case ($y_0 = \lambda$) as shown in Fig. 4-17, in which the abscissa y now stands for the distance measured from the position of the substrate before the start of vibration. The instantaneous location of the local maximum pressure at the ligament root is indicated by a filled circle on each curve. Thus, the ligament dynamically freed from the substrate is the region on the right side of the circle. The maximum pressure location emerges at $t=3.20T$ and moves downwards and disappears after $t=3.50T$.

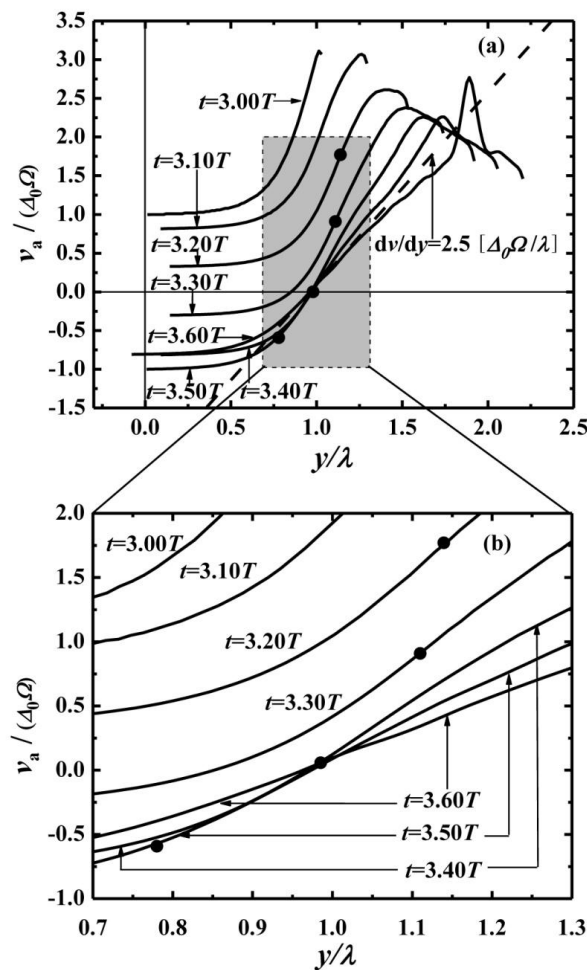


Fig. 4-17 Temporal change in vertical velocity distribution along the crest center line ($x=3\lambda/4$) observed in the laboratory reference frame for the period from $t=3.00T$ to $t=3.60T$, during which ligament is formed. The abscissa y represents the distance from the initial location of the substrate surface. For clarity, the gray region in (a) is enlarged as shown in (b). The filled circle indicates the maximum pressure location at each instant, which moves down as time elapses and disappears after $t=3.50T$. The vertical velocity in the freed ligament region can be approximated by a dashed straight line with a temporally decreasing slope.

All the ligament liquid elements above the maximum pressure location keep their vertical velocities in the laboratory reference frame. For example, the stationary point where $v_a=0$, indicated by the open circle in Fig. 4-4, retains its position fixed after $t=3.40T$ (see Fig. 4-4 or Fig. 4-17). This is because, for the freed ligament whose ratio of thickness to length is small, the pressure relaxes to a uniform value consistent with the surrounding gas pressure ($\partial p/\partial y \cong 0$, see Fig. 4-8 (c)), except for the ligament tip where the effect of contraction by surface tension is significant. Since an upper ligament element moves faster than a lower one, the upper ligament element becomes thinner than the lower element as time goes by. As a result, the freed ligament takes a quasi-trapezoidal shape narrowing upward. It is notable that the vertical velocity along the freed liquid region (except the tip portion) increases approximately linearly as indicated by the dashed straight line in Fig. 4-17. The slope of vertical velocity $\partial v/\partial y$ decreases with time. Standing at the location where velocity vanishes, this ligament development process can be described by a simple model explained below.

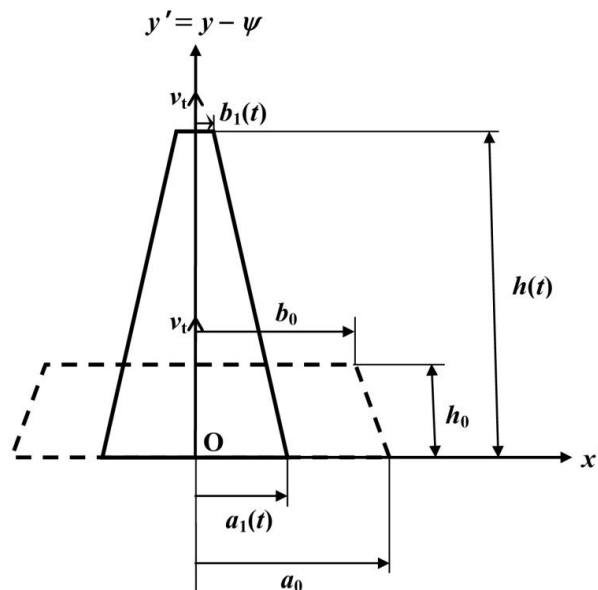


Fig. 4-18 A model of a freed ligament development. The initial shape is denoted as the dashed lines. The bottom corresponds to the stationary point ($v_a=0$) as noted by the open circle in Fig. 4-4.

Fig. 4-18 is the schematic of a ligament development model viewed in the laboratory reference frame, which can be recognized as an approximation of the liquid region above the stationary point $y = \psi$ (i.e., $y' = 0$ in Fig. 4-18) but excluding the ligament

tip. An upper liquid mass moves upwards with a different vertical velocity along the vertical axis y without any external force applied. The vertical velocity at the stationary point is zero, while the velocity at the top of this region is $v_t = dh(t)/dt = \text{const}$, where $h(t)$ is the height from the stationary point to the top. $h(t)$ can be expressed by $h(t) = h_0 + v_t t$, where h_0 is the initial height of liquid mass. Since v_a gradually changes from 0 at $y' = 0$ to v_t at $y' = h(t)$ at each time, we assume that $\partial v_a / \partial y = v_t / h(t)$, consistent with the observation in Fig. 4-17 that the vertical velocity in the freed ligament portion is approximated by a straight broken line with a temporally decreasing slope. Then, applying the continuity equation to the whole region $0 < y' < h(t)$ leads to $db_1/dt = -b_1 v_t / h$, $da_1/dt = -a_1 v_t / h$, that is, $b_1 = b_0 h_0 / (h_0 + v_t t) = b_0 h_0 / h$ and $a_1 = a_0 h_0 / (h_0 + v_t t) = a_0 h_0 / h$, which naturally conserves the area of the quasi-trapezoidal shape of ligament: $(a_1 + b_1)h = (a_0 + b_0)h_0$. The gradient of the ligament thickness distribution along the center line is expressed by

$$\frac{b_1 - a_1}{h} = \frac{(b_0 - a_0)h_0}{(h_0 + v_t t)^2}. \quad (4-16)$$

The gradient magnitude decreases as time elapses. According to the assumption $b_0 < a_0$, this means the left and right surfaces of the freed ligament tend to move toward the center, which results in a ligament of slender shape.

In the 3D case, a significant difference appears in the ligament behavior due to the presence of circumferential surface tension. However, the freed ligament formed by an axi-symmetric flow about the ligament centerline has the same formation mechanism as the 2D case. In particular, Eqs. (4-10)–(4-12) and (4-15) hold as they stand because the radially concentrating flow produced in the liquid layer only modifies the radial strain rate (equals to half the axial strain rate E). The dependence of the order of magnitude of the axial strain rate E on the forcing parameters is unchanged. Only the numerical value of the non-dimensionalized E will be modified. At the stage when the freed ligament develops, variation in the local ligament radius along the ligament is moderate. Therefore, the liquid passing the maximum pressure base tends to relax its pressure to a value determined by the local ligament radius r , *i.e.*, $\sigma/r(y)$, instead of the surrounding gas pressure (zero). Correspondingly, the maximum pressure at the

ligament base must be increased to a larger value. The breakup behavior of the freed liquid ligament is similar to that of an orifice liquid jet accelerated downward by gravity. **Umemura (2011)** identified how the unstable waves responsible for breakups are produced in an accelerating water jet. In the present 2D prototype calculations, the equivalent jet issue speed and acceleration rate are not large. In a similar jet issue condition, the 3D ligament will disintegrate into droplets in a drip-like mode, for which the circumferential surface tension plays a secondary role, as captured in the present 2D calculations. For the case when a long ligament forms, replacing the 2D ligament width by the 3D ligament cross-sectional area, Eq. (4-16) may be used to characterize a baseline ligament for the instability analysis of a 3D ligament.

Chapter 5

Threshold condition for spray formation due to Faraday instability

In this chapter, as an extension of Chapter 4, we discuss the threshold condition for spray formation due to Faraday instability. First, we consider the implications derived from the previous experiments to simplify the problem of threshold condition. The existence of a predominant surface wave mode in the Faraday instability can greatly reduce the calculation burdens. Then, we determine the predominant surface wave mode for each forcing strength β based on the Mathieu equation as described in Chapter 4. Finally, we define a physical critical condition for the spray formation due to Faraday instability and present the detailed characteristic features for different forcing strength. The determined threshold forcing strength β_c in this dissertation is $\sim O(1)$, which is found to be two orders larger than the previous studies on the threshold value for rare drop ejections. This threshold condition is proven to be independent of the initial surface disturbance.

5.1 Experimental implications

According to the previous experiments on the rare drop ejection from a liquid layer due to Faraday instability (**Goodridge et al., 1997; Goodridge et al., 1999; Vukasinovic et al., 2007; Puthenveetil and Hopfinger, 2009**), a typical approach for determining the threshold condition is to fix the forcing angular frequency Ω and gradually increase the forcing displacement amplitude Δ_0 from zero until the concerning phenomenon, *e.g.*, two drops detected within a ten-second-period, can be observed. The same procedure is repeated at other forcing frequencies to obtain the threshold forcing amplitude Δ_d as a function of Ω . Alternatively, the threshold forcing acceleration amplitude $A_d = \Delta_d \Omega^2$ can be expressed as a function of Ω . For the inviscid liquid case, recent experimental results have shown that

$$A_d = c \cdot \left(\frac{\sigma}{\rho_l} \right)^{\frac{1}{3}} \Omega^{\frac{4}{3}} \quad (5-1)$$

with $c = 0.261$ (Goodridge et al., 1997; Goodridge et al., 1999; Puthenveetil and Hopfinger, 2009) or $c = 0.345$ (Vukasinovic et al., 2007). The dimensionless parameter $\beta = \rho_l \Delta_0^3 \Omega^2 / \sigma$ (the cube of the dimensionless forcing acceleration amplitude in conventional terminology) at the threshold condition for rare drop ejection is $\beta_d = c^3 = 0.018$ or 0.041 . Note that, according to studies into surface-wave pattern selection, these values belong to the regime where a standing wave is believed to be formed. 2D calculations carried out by Ubal et al. (2003) for all sub-harmonically unstable waves showed that a standing wave pattern is realized until $\beta = 0.2 \sim 0.9$ for a layer of water forced at a forcing frequency of 29 kHz under normal gravity, although the calculations were terminated with a much smaller number of the forcing cycles ($\sim O(100)$) than that necessary for drop ejection ($\sim O(1000)$) in the experiments.

For industrial application, we are more interested in the spray formation, in which controllable sizes of drops can be generated steadily and vigorously. Obviously, the rare drop ejection studied in the previous experiments as discussed above is not suitable for these applications, and therefore nor are the threshold conditions described above. More useful information, for our purpose, is provided by the ultrasonic atomization experiments. It is well known that the drops produced at a given forcing frequency Ω have a very narrow size distribution that is essentially independent of Δ_0 (Lang, 1962; Rajan and Pandit, 2001). For a sufficiently deep liquid layer, the mean drop diameter d_m decreases with increasing forcing frequency according to the Lang's equation, *i.e.*,

$$d_m = l \cdot \lambda_0 = l \cdot 2\pi \left(\frac{\sigma}{\rho_l} \right)^{\frac{1}{3}} \left(\frac{2}{\Omega} \right)^{\frac{2}{3}} \quad (5-2)$$

where $l = 0.35 \pm 0.03$. The last equality in Eq. (5-2) is due to the use of the Kelvin's expression $\lambda_0 = 2\pi/k_0 = 2\pi(\sigma/\rho_l)^{1/3} (2/\Omega)^{2/3}$ (Kelvin, 1871), which denotes the wavelength of the 'forcing-free' surface wave oscillating at a frequency of $\Omega/2$. Therefore, λ_0 should be generally different from the wavelength of a predominant Faraday wave realized at the forcing frequency Ω . Nevertheless, Lang's equation, which correlates the atomized drop diameter with the forcing frequency and is

validated by previously reported ultrasonic atomization experiments, indicates the presence of a predominant Faraday wave in each experimental realization. In fact, if drops are produced via the disintegration of liquid ligaments formed from the surface waves that result from the Faraday instability and are independent of the effects of the container walls, then the conventional mode selection concept leads us to an idea that there exists a predominant surface wave from which a ligament disintegrating into drops is formed periodically to generate the spray. Hence, the remaining theoretical question is how to identify the predominant surface wavelength that appears in spray formation, and how to develop an approach to finding the threshold condition.

5.2 Numerical strategy

Before discussing on how to identify the predominant surface wave, we present the calculation domain in the present numerical study. The most straightforward way to numerically determine the threshold condition for spray formation by a Faraday instability is to perform simulations that can capture all excitable wavelengths with sufficient spatial and temporal resolution for a large horizontal extension of a liquid layer. However, this is not practical. The above-mentioned spray formation from the predominant surface wave means that if a drop is formed at a place, there must be other (infinite number of) places where similar drops are formed. Therefore, we consider the dynamics developing in a cell model spanning one predominant surface wavelength horizontally (see Fig. 3-1). The threshold condition for repeated drop formation in such a cell model should correspond to the threshold condition for spray formation from the entire liquid layer.

In the following, 2D configuration is considered for theoretical and numerical simplicity. From Chapter 4 we can see that the main dynamics essential for the formation of liquid ligament disintegrating into drops from a vertically vibrating liquid layer can be captured by 2D calculations. The difference and sameness between 2D and 3D configurations will be briefly discussed in §5.3.5 after presenting 2D calculation results.

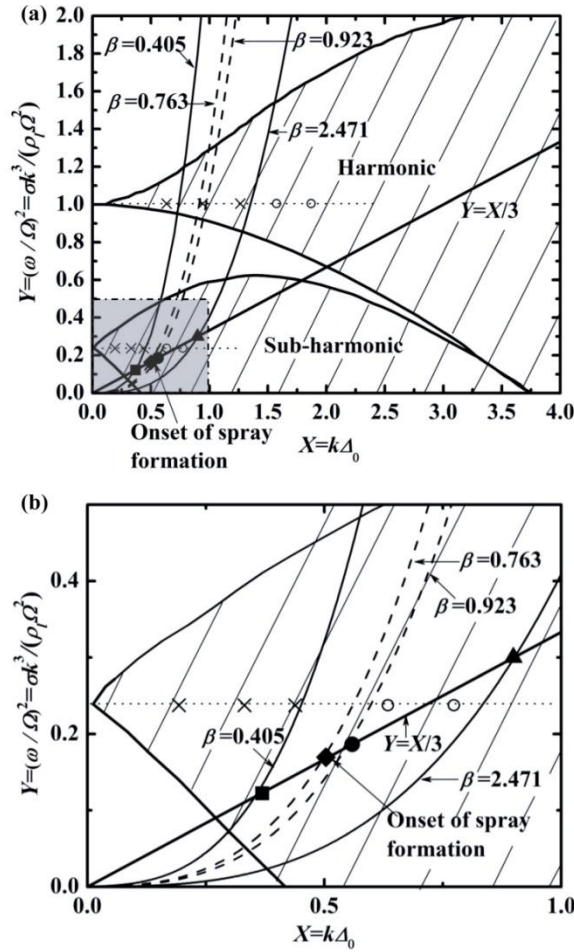


Fig. 5-1 The instability regions (hatched regions) for the Mathieu equation and the numerical strategy for determining the threshold condition for spray formation. Panel (b) is the enlargement of the shadowed square region in Panel (a). Each cubic curve represents one experimental condition characterized by the dimensionless forcing strength $\beta = \rho_1 \Delta_0^3 \Omega^2 / \sigma$. The points on the solid straight line $Y = X/3$ correspond to the predominating surface wave numbers at different values of β . The filled square is the non-atomization case discussed in §5.3.1. The filled triangle is the atomization case discussed in §5.3.2. The filled diamond and the filled circle are the near-critical cases discussed in §5.3.3. The filled diamond represents the onset of spray formation in the present study. The cases other than those on the straight line $Y = X/3$, represented by the cross symbols and open circles, are also simulated by fixing $Y = 0.25$ and 1 and changing the values of X . The cross symbols stand for the calculation cases at which no break-up occurs while the open circles for those at which break-up occurs.

Our numerical strategy for determining the threshold condition for spray formation is based on a 2D Faraday instability theory. As discussed in Chapter 4, when the surface deformation is small, the amplitude δ of the surface deformation $\delta(t)\sin(kx)$ in the cell model obeys the Mathieu equation (Eq. (4-1)). Whether the surface wave is stable or not is determined by two parameters, X and Y as defined by

Eq. (4-2). In this chapter, we considered the case $\tanh(ky_0) \rightarrow 1$ to eliminate the effects of the liquid depth y_0 . The surface waves, whose corresponding parameter pair (X, Y) lies in an instability region in Fig. 5-1, are able to increase their amplitudes up to certain values and eventually reach standing-wave, break-up states at a nonlinear stage. Thus, the realization for each experimental condition (Δ_0, Ω) can be depicted as a cubic curve (Eq. (4-3))

$$Y = X^3 \left(\frac{\sigma}{\rho_1 A_0^3 \Omega^2} \right) = \frac{X^3}{\beta}. \quad (5-3)$$

This equation demonstrates that the possible linear surface waves emerging in an experimental realization are characterized by the single dimensionless parameter $\beta = \rho_1 A_0^3 \Omega^2 / \sigma$ associated with the experimental forcing condition (Δ_0, Ω) . For this reason, β is called the dimensionless forcing strength hereafter. The wave numbers excitable at a given value of β are located on the cubic curve in the instability region.

The results of ultrasonic atomization experiments imply that, as discussed above, for each forcing strength β , we only need to calculate one case corresponding to the predominant surface wave number k_m if k_m can be determined rationally. We describe an approach to determine k_m in the following.

The expression

$$\alpha^2 = X \sin \tau - Y = k A_0 \sin \tau - \frac{\sigma k^3}{\rho_1 \Omega^2}. \quad (5-4)$$

defines the square growth rate. The magnitude of the growth rate is dependent on the wave number k and dimensionless time τ for a given experimental condition (Δ_0, Ω) . If the amplified surface wave reaches a nonlinear stage during this period, the subsequent surface deformation no longer obeys the Mathieu equation. Therefore, the magnitude of Eq. (5-4) provides an indicator describing how fast the linear surface wave evolution undergoes a transition into a nonlinear evolution, such as the formation of a steady standing wave or a liquid ligament dynamically free from the motion of the bulk liquid layer. The destabilizing phase duration (when $\alpha^2 > 0$) $T_{de}(k) = \pi - 2 \arcsin \left[\sigma k^2 / (\rho_1 A_0 \Omega^2) \right]$ and the amplitude of the squared growth rate $\alpha_{am}^2(k) = k A_0 \sin \tau - \sigma k^3 / (\rho_1 \Omega^2)$ (see Fig. 5-2) are the two factors that influence the

growth of the surface wave amplitude. $T_{de}(k)$ is a decreasing function of k , whereas $\alpha_{am}^2(k)$ assumes its peak value at $k = k_m$. For a sufficiently large forcing strength β , even though $\alpha_{am}(k)$ for the other wave numbers $k \neq k_m$ is small, if the destabilizing phase persists, the total accumulated enhancement of the surface wave amplitude may become large enough to form a liquid ligament and subsequent break-up. However, in this study, we intend to find the minimum forcing strength under which spray formation can be initiated. It is obvious that a liquid ligament disintegrating into drops begins to be formed in a destabilizing phase. Therefore, we are interested in the surface wave number k_m that maximizes the value of $\alpha_{am}(k)$ in each experimental realization. The wave number k_m satisfying this condition is given by

$$k_m^2 = \frac{1}{3} \frac{\rho_1 A_0 \Omega^2}{\sigma}. \quad (5-5)$$

The surface waves whose wave numbers are close to this value have the largest growth rate of their amplitudes. For such surface waves, we have

$$Y = \frac{1}{3} X, \quad (5-6)$$

which is depicted as the solid thick straight line in Fig. 5-1. Each point on the straight line $Y = X/3$ corresponds to the predominant surface wave mode for a forcing strength β . The problem is then reduced to finding the critical forcing strength β_c for spray formation by simulating the cases in which the wavelengths of the cell model are specified by the points (X, Y) on this line ($Y = X/3$) in the instability region.

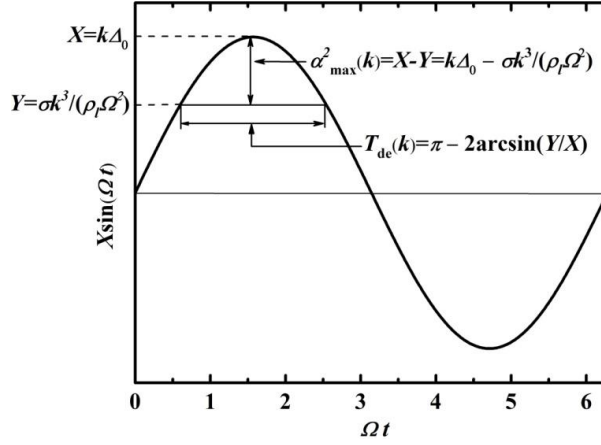


Fig. 5-2 Illustration of the destabilizing phase duration, T_{de} , and the maximum value of growth rate, α_{max} .

5.3 Threshold condition for spray formation

To conduct calculations based on the cell model, it is convenient to normalize the coordinates (x, y) by the cell width $\lambda = 2\pi/k$ and time t by the forcing frequency Ω such that $(\tilde{x}, \tilde{y}) = (x, y)/\lambda$ and $\tilde{t} = \Omega t$. Mathematically, any quantity can be used to make the velocity dimensionless. However, the reference velocity $\lambda\Omega$ is physically not appropriate to use for the normalization of the velocity because the velocity field produced by the inertial force $\rho\Delta_0\Omega^2$ must depend on the forcing displacement amplitude Δ_0 as well. We non-dimensionalized the velocity and pressure fields as $(\tilde{u}, \tilde{v}) = (u, v)/(\Delta_0\Omega)$ and $\tilde{p} = p/(\rho\Delta_0\Omega^2\lambda)$. Then, the governing equations (3-1) can be transformed to the following dimensionless form.

$$\begin{cases} \tilde{\nabla} \cdot \tilde{\mathbf{u}} = 0 \\ \frac{\partial \tilde{\mathbf{u}}}{\partial \tilde{t}} + \frac{X}{2\pi} (\tilde{\mathbf{u}} \cdot \tilde{\nabla}) \tilde{\mathbf{u}} = -\tilde{\nabla} p + \sin \tilde{t} \mathbf{e}_y - \frac{Y}{(2\pi)^2 X} \tilde{\nabla} \cdot \mathbf{n} \tilde{\nabla} \mathbf{H} \end{cases} \quad (5-7)$$

where the parameters X and Y are defined in Eq. (4-2). The boundary conditions do not contain any parameter.

Given an experimental condition (Δ_0, Ω) , which are the only controllable variables for a given infinitely extended deep liquid layer, the value of the dimensionless forcing strength β is determined. We consider a series of experiments increasing the β -value from a small value and examine how the surface deformation

feature changes with β . According to the familiar selection concept, it is considered that the fastest growing disturbance mode prevails in each experimental condition. Therefore, according to the numerical strategy described in the previous section, we calculated the evolution of a linear wave mode on the line $Y = X/3$ in Fig. 5-1 for each experimental condition characterized by the β -value. In this case, the parameters X and Y in Eq. (5-7) take the values $X = \sqrt{\beta/3}$ and $Y = \sqrt{\beta/3^3}$. Therefore, Eq. (5-7) is rewritten as

$$\begin{cases} \tilde{\nabla} \cdot \tilde{\mathbf{u}} = 0 \\ \frac{\partial \tilde{\mathbf{u}}}{\partial \tilde{t}} + \frac{\sqrt{\beta}}{2\sqrt{3}\pi} (\tilde{\mathbf{u}} \cdot \tilde{\nabla}) \tilde{\mathbf{u}} = -\tilde{\nabla} p + \sin \tilde{t} \tilde{\mathbf{e}}_y - \frac{1}{(2\sqrt{3}\pi)^2} \tilde{\nabla} \cdot \mathbf{n} \tilde{\nabla} H, \end{cases} \quad (5-8)$$

This indicates that the predominant Faraday instability realized in each experimental condition is determined by the β -value only. At small β -value, the above equation describes a linear wave evolution. For a relatively large β -value, all terms become comparable in the liquid phase and the convective term may contribute to the surface deformation. Note that Eq. (5-8) is not a dimensionless equation system accounting for the flow structure that the surface deformation influence is confined within a thin layer on the interface. Therefore, the condition $\beta \sim 12\pi^2 \sim 100$, derived by simply equating $\sqrt{\beta}/(2\sqrt{3}\pi)$ to unity in Eq. (5-8), does not express the balance between the unsteady and convective terms in the numerically calculated flow.

Six typical cases, *i.e.*, ($X = 0.3675, Y = 0.1225$), ($X = 0.4564, Y = 0.1521$), ($X = 0.5043, Y = 0.1681$), ($X = 0.5547, Y = 0.1849$), ($X = 0.6075, Y = 0.2025$) and ($X = 0.9075, Y = 0.3025$), corresponding to the dimensionless forcing strengths $\beta = 0.405, 0.625, 0.763, 0.923, 1.107$ and 2.471 , respectively, were simulated to determine the threshold condition for spray formation. It is difficult to define a criterion for spray formation. In the present study, we considered that the threshold condition for spray formation from the entire liquid layer is equivalent to the one for repeated drop formation in the cell model of the predominant surface wavelength. A disintegrating ligament may form in the destabilizing phase, even under a relatively small forcing strength so far as time elapses long enough. However, the broken drop will not have an outward velocity in the laboratory reference frame. Then, the drop falls back and coalesces with the liquid layer. Therefore, spray is not formed under such condition.

Further enhancement of the forcing strength increases the vertical velocity of the broken drop. In this dissertation, we didn't consider the effects of viscosity and gravity. Whether the broken drop rises away from or falls back to coalesce with the liquid layer depends only on its center-of-mass velocity at the time when the break-up occurs. As the criterion for spray formation, we adopted the condition in which the broken drop holds a null area-averaged vertical velocity in the laboratory reference frame at the break-up instant. According to this definition, the calculation results showed that spray formation onsets when the dimensionless forcing strength β reaches a critical value around $\beta_c = 0.763 \sim O(1)$.

Besides the predominant surface wave mode cases, we calculated other cases that are not located on the straight line $Y = X/3$ as well. The calculation results showed that broken drops of outward area-averaged vertical velocity are only formed in the cases located to the right of the cubic curve $Y = X^3/\beta_c$, which validates that the critical dimensionless forcing strength value for spray formation is $\beta_c = 0.763$.

In the following, we will explain the calculation results. We describe the dynamic change in the Faraday instability as a function of β , and then identify the threshold value of β .

5.3.1 Non-atomization case

The solid line in Fig. 5-3 (a) shows the temporal evolution of the surface displacement at $x = \lambda/4$ for the case ($X = 0.3675$, $Y = 0.1225$) (filled square in Fig. 5-1, $\beta = 0.405$). The solution of the Mathieu equation with the same parameters and initial conditions as calculated by the fourth-order Runge-Kutta method is also presented by the dashed line in Fig. 5-3 (a). Though this parameter pair lies in the instability region, atomization does not occur. The amplitude of the surface displacement eventually achieves a steady value around 0.17λ . This state is considered to be the realization of a Faraday standing-wave. In the early stage when the surface displacement is small, the calculation result agrees well with the linear solution. Deviation of the calculation results from the linear solution arises when higher modes of the surface deformation become significant, as shown in Fig. 5-3 (b), in which the temporal evolutions of the first three spatial modes obtained by the Fourier decomposition of the surface deformation are shown. In the standing-wave regime, the amplitude of the surface

displacement oscillates slightly from one period to another, tending to be saturated rather than amplified. Fig. 5-3 (c) shows the surface shapes at typical instants (indicated by the filled circles in Fig. 5-3 (a)) in two different surface deformation cycles. When the Faraday standing-wave state is reached, the same surface deformation is repeated in different cycles.

We have assumed that the flow is inviscid in this dissertation. Therefore, the standing-wave state corresponds to the zero net work performed on the liquid layer by the inertial force during one period of the surface deformation cycle. Fig. 5-4 (a) shows the temporal evolution of the work rate performed by the inertial force ($\rho_1 \iint A_b \Omega^2 \sin(\Omega t) \cdot v_r dx dy$, where v_r is the vertical velocity referring to the vibrating bottom substrate) on the liquid layer. In the early stage, the work rate is mostly positive because of the liquid layer flow resonating with the inertial force oscillation (linear instability). As a result, the amplitude of the surface displacement grows rapidly as time elapses. When the surface deformation becomes relatively large, nonlinear effects gradually become more dominant, which delays the recovering of the surface crest or trough to the neutral surface position, because the liquid flowing at a large velocity tend to keep the same velocity by inertia. As such, a phase difference is created between the liquid layer flow and the inertial force ($\rho_1 A_b \Omega^2 \sin(\Omega t)$), as shown in Fig. 5-4 (b), in which the temporal evolutions of the surface displacement at $x = \lambda/4$ and the inertial work rate are displayed for one period of the surface deformation cycle in the standing-wave regime (from $t = 20.3T$ to $t = 22.3T$). This phase difference increases the negative work rate and thus decreases the growth rate of the amplitude of the surface displacement. From $t = 20.5T$ to $t = 21T$, at which the inertial force takes a negative value, the following two behaviors are observed. The liquid first flows towards the crest. Because most of the liquid moves upward, the work rate, which is the product of the inertial force and vertical velocity, is negative. The liquid flow then changes its direction after about $t = 20.75T$, resulting in a positive work rate. Similar behaviors occur repeatedly, resulting in zero net work over the course of one surface deformation cycle.

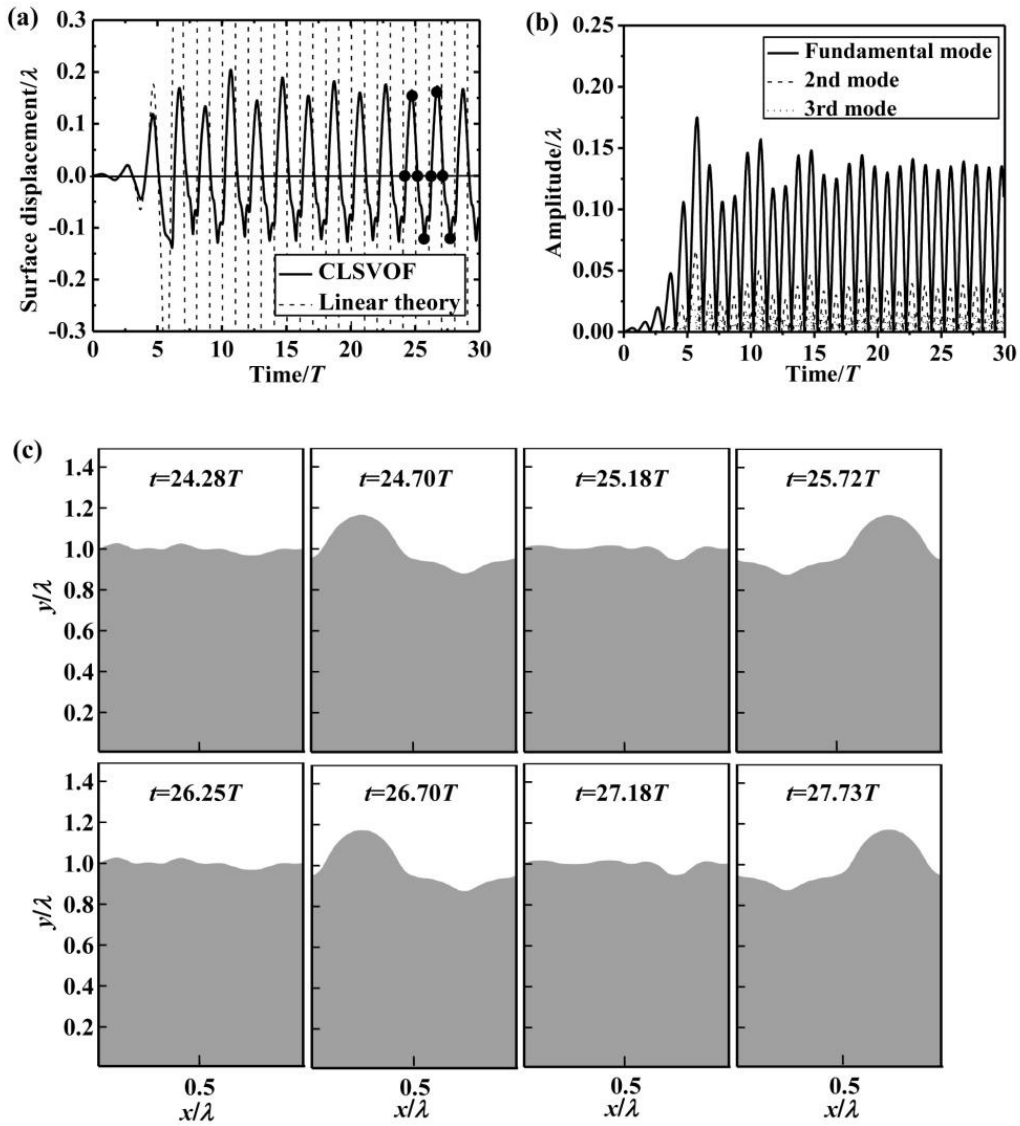


Fig. 5-3 Calculation results for the case ($X = 0.3675$, $Y = 0.1225$) (filled square in Fig. 5-1, $\beta = 0.405$), at which Faraday standing-wave is formed. (a) Temporal evolution of the surface displacement at $x = \lambda/4$. The dashed line is the solution to the Mathieu equation with the same parameters and initial conditions. (b) Temporal evolutions of the first three spatial modes. (c) Comparison of the surface shapes at the instants in two different cycles, which are indicated by the filled circles in panel (a).

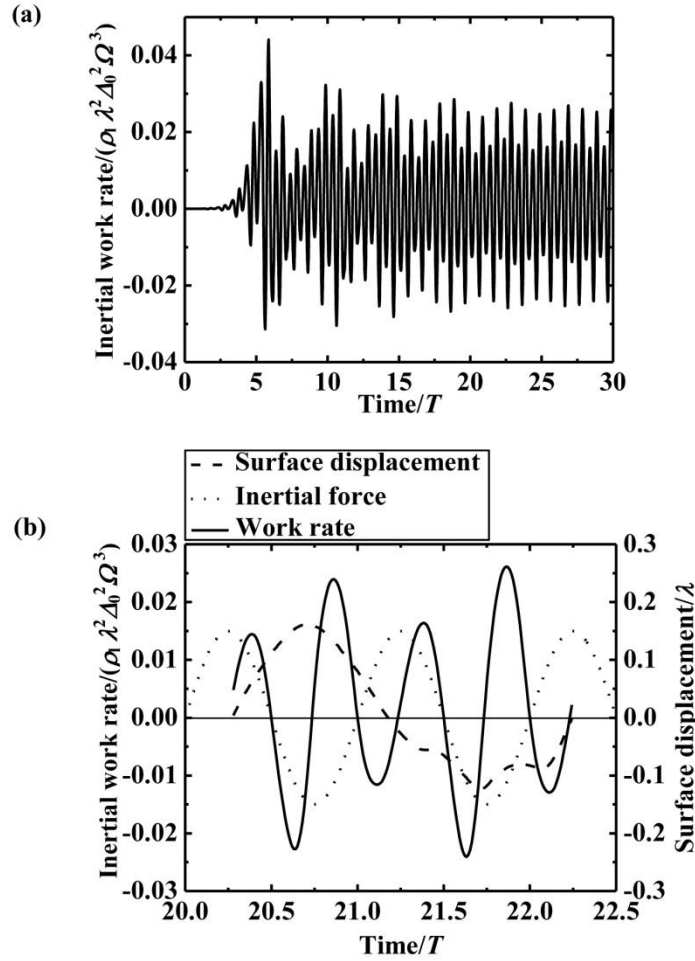


Fig. 5-4 Work performed on the liquid layer by the inertial force for the case ($X = 0.3675$, $Y = 0.1225$). (a) Temporal evolution of the work rate. (b) Enlargement of (a) from $t = 20.3T$ to $t = 22.3T$, along with the temporal evolutions of the surface displacement at $x = \lambda/4$ and the inertial force.

5.3.2 Atomization case

Fig. 5-5 shows the temporal evolution of the surface height at $x = 3\lambda/4$ for the case ($X = 0.9075$, $Y = 0.3025$) (filled triangle in Fig. 5-1, $\beta = 2.471$). This is also the prototype case used to discuss the basic dynamics of the ligament formation in Chapter 4. In this case, due to the strong forcing, a free ligament is formed and its first break-up occurs at a relatively early stage. Initially, when the surface deformation is small, the calculation result agrees with the solution to the Mathieu equation (dashed line). Large surface deformation occurs at the same frequency as the linear solution, which is consistent with experimental observations that drops are formed from the sub-harmonically oscillating liquid surface. Because the period of the resulting

unstable liquid layer flow is fixed by the forcing frequency, the increased forcing strength amplifies the magnitude of the liquid velocity. As a result, the convective term becomes more effective. We have studied the detailed dynamics of ligament formation in Chapter 4. Its essence is illustrated in Fig. 5-6. By inertial force, the impinging of the liquid continuously flowing from the neighboring trough portions increases the pressure at the crest root. This nonlinear flow delays the phase of surface displacement from the linear solution. If this pressure is larger than the capillary pressure, then the crest can grow to be a long ligament whose pressure relaxes to the surrounding uniform gas pressure. Thus, the enhanced pressure at the ligament root takes the form of a local maximum pressure location. This means that the liquid ligament above this location becomes dynamically free from the motion of the vibrating bottom substrate. As a result, the liquid flowing from the trough portions and passing the local maximum pressure location moves upward freely and extends the ligament length. Thus, the created liquid ligament behaves like a low-speed water jet issuing vertically downward from an orifice under gravity, and tends to disintegrate into drops (Stone et al., 1986; Stone and Leal, 1989; Schulkes, 1994; Umemura, 2011).

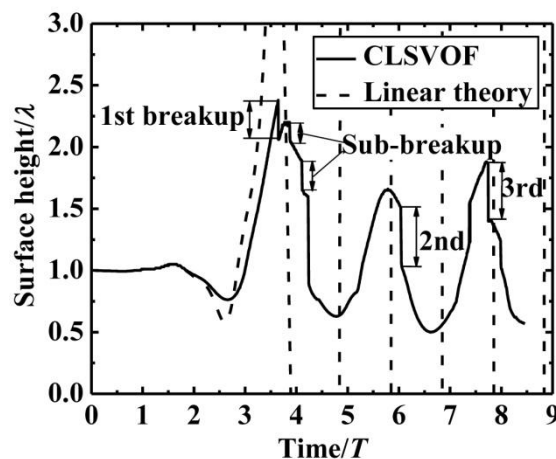


Fig. 5-5 Temporal evolution of the surface height at $x = 3\lambda/4$ for the case ($X = 0.9075$, $Y = 0.3025$) (filled triangle in Fig. 5-1, $\beta = 2.471$), in which break-up occurs continuously as indicated by the abrupt descents. The dashed line is the solution to the Mathieu equation with the same parameters and initial conditions.

Each break-up of a liquid ligament is expressed by an abrupt descent of the surface height in Fig. 5-5. The first break-up of a ligament, resulting in an outward moving drop, occurs at $t = 3.65T$, followed by two sub-break-ups of the same

ligament, resulting in drops moving towards and coalescing with the liquid layer (If the forcing strength is increased further, multiple drops having outward velocities may form from a ligament). After these break-ups, the free ligament disappears in the following stabilizing phase. Because the resulting relatively flattened surface state is similar to the initial surface state of the liquid layer, but with finite amplitude, similar repeatable events occur (steady atomization). Fig. 5-5 indicates the occurrence of the second and third break-ups over subsequent time periods.

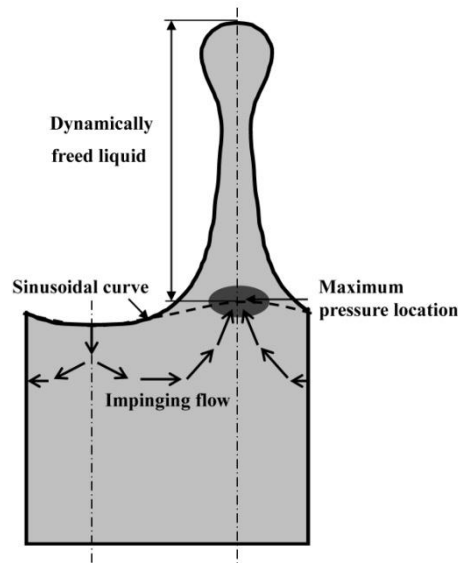


Fig. 5-6 Essential dynamics of the liquid ligament formation by a Faraday instability.

As seen in Fig. 4-17, which shows the vertical velocity distribution along the crest centerline ($x = 3\lambda/4$) in the laboratory reference frame before the first breakup occurs, the velocity in the broken drop region is positive just before the breakup time ($t=3.60T$), indicating that the broken drop holds an outward velocity in average. Fig. 5-7 (a) and (b) show the vertical velocity distributions at the second and third break-up instants. The velocity is viewed in the laboratory reference frame. It is clear that the vertical velocity in the drop region viewed in the laboratory reference frame is positive except at the tip recessed by surface tension. The broken drops having positive area-averaged velocities rise away and never fall back to the liquid layer. Therefore, once a break-up occurs at the tip of a ligament, the liquid layer loses the mass and energy that the broken drops possess. This means that the spray formation by a Faraday instability is a process that the liquid layer absorbs energy from the inertial force and then releases it partially by producing drops leaving the liquid layer.

In particular, a steady atomization state is realized when the energy gain becomes equal to the energy loss on a time average. Fig. 5-8 (a) and (b) display the temporal evolutions of the inertial work rate and its time integration $(\rho_1 \int_0^t [\iint \Delta_0 \Omega^2 \sin(\Omega t) \cdot v_r dx dy] dt)$, plotted as the thick line in Fig. 5-8 (b)). The thin solid line in Fig. 5-8 (b) shows the energy possessed by the liquid layer, which is obtained by subtracting the surface and kinetic energy possessed by the broken drops (downward arrows) from the inertial work (thick solid line). The energy possessed by the liquid layer just after each break-up remains at an almost constant level (horizontal dashed line connecting three arrow tips in Fig. 5-8 (b)). The energy absorbed by the liquid layer from the inertial force between two break-ups is utilized to release the next broken drop. This indicates the broken drops are formed repeatedly.

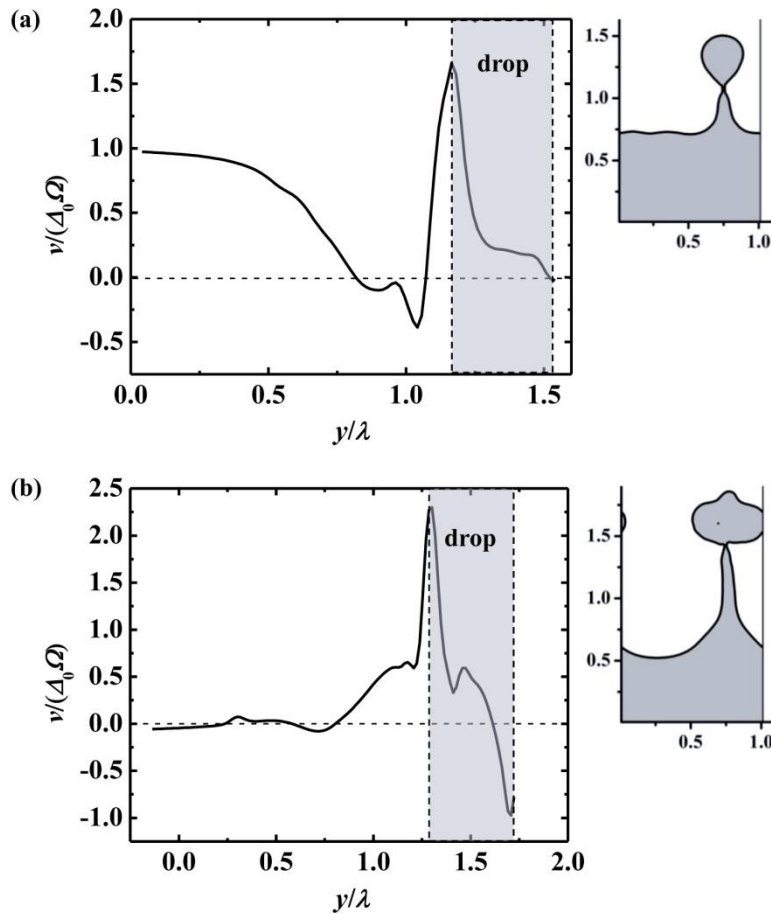


Fig. 5-7 Vertical velocity distribution along the crest centerline ($x = 3\lambda/4$) for the case ($X = 0.9075, Y = 0.3025$) at (a) $t = 6.04T$ and (b) $t = 7.74T$, corresponding to the second and third break-ups in Fig. 5-5, respectively. The velocity is viewed in the laboratory reference frame. The insets are the surface shapes at the corresponding instants.

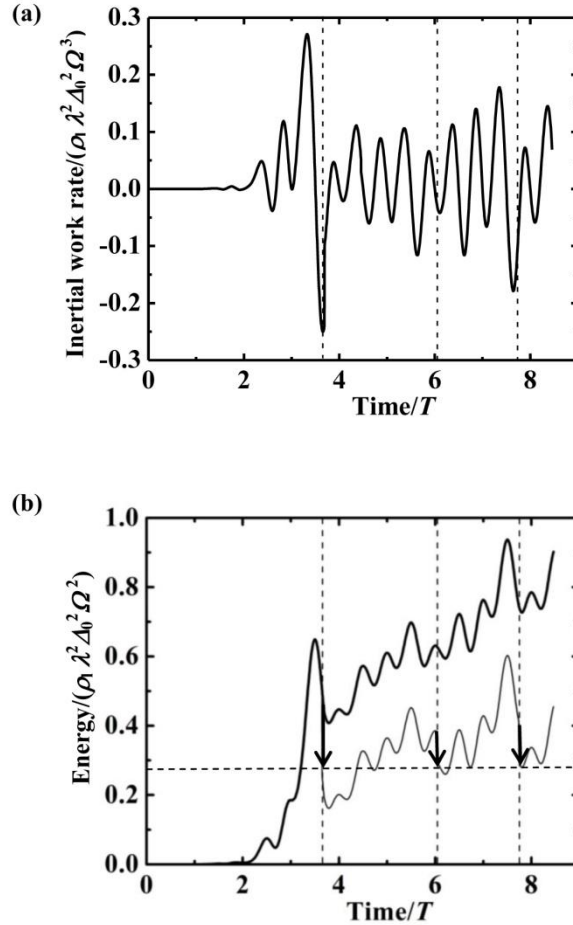


Fig. 5-8 Work performed on the liquid layer by the inertial force for the case ($X = 0.9075$, $Y = 0.3025$). (a) Temporal evolutions of the inertial work rate. (b) Temporal evolutions of the inertial work (thick solid line) and the energy possessed by the liquid layer (thin solid line) which is derived by subtracting the surface and kinetic energy possessed by the broken drops (downward arrows). The three vertical dashed lines represent three break-up instants. The arrow tips indicate the energy possessed by the liquid layer just after each break-up, which is kept almost at a constant level (the horizontal dashed line).

The Fourier decomposition of the surface deformation, conventionally used to gain insight into the higher-order waves, is indeed useful for the non-atomization case. However, we encounter some difficulties in the atomization case. This is why we detailed the ligament structure in Fig. 5-6. Fig. 5-9 (a) denotes the temporal evolutions of the first three spatial modes obtained by the Fourier decomposition of the surface deformation. The zeroth mode indicates the mean height of the surface. In principle, this should decrease discontinuously by an amount corresponding to the volume of a broken drop. The Fourier decomposition loses efficacy when a ligament with a bulbous tip is formed as shown in Fig. 5-9 (b). The surface profile, $s = s(x)$, becomes a multi-valued function. In the present Fourier decomposition of such surface profile,

the lowest point (filled circle in Fig. 5-9 (b)) is adopted as the surface point at this abscissa. Therefore, the mean height of the surface decreases before break-up. It should be noted that the amplitudes of the second and third modes, which become almost comparable with that of the first (fundamental) mode once the ligament forms, are the result of the protruding shape of the ligament used in the Fourier decomposition. As described above, the free ligament above the local maximum pressure location has no dynamic connection with the liquid layer below the local maximum pressure location; thus, simple Fourier decomposition of the surface deformation does not reflect the fundamental motion of the liquid layer. In fact, if we remove the free ligament portion (liquid region above the local maximum pressure location) from the liquid layer, the shape of the trough surface and the “new crest surface” (the top of this new crest surface is at the local maximum pressure location) can be approximated as a sinusoidal curve with the fundamental wavelength (see the dashed curve in Fig. 5-6).

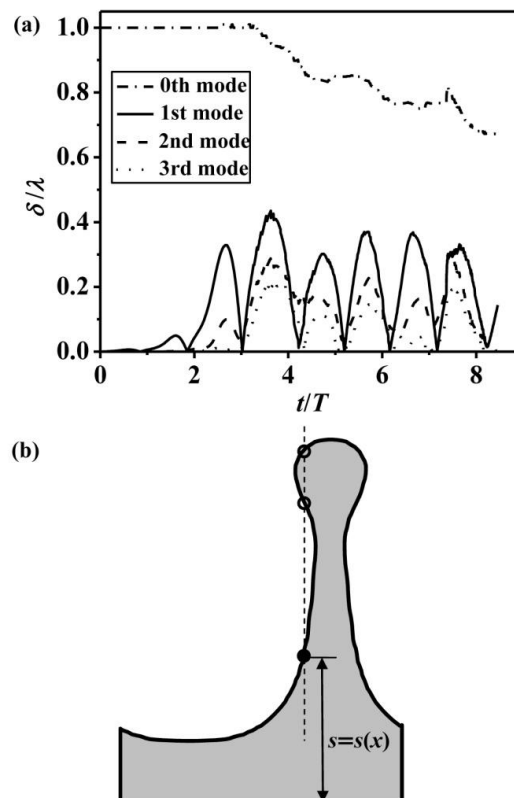


Fig. 5-9 Fourier decomposition of the surface deformation for the case ($X = 0.9075$, $Y = 0.3025$). (a) Temporal evolutions of the first three spatial modes and the zeroth mode. (b) Multi-valueness of the surface profile function due to bulbous tip.

5.3.3 Near-critical case

The critical dimensionless forcing strength for spray formation β_c should be between 0.405 and 2.471, the two cases discussed in the previous two sections. We demonstrated two other cases near the threshold condition in this section.

Fig. 5-10 shows the temporal evolution of the distance between the crest top and the trough bottom, $|y_{\text{crest}} - y_{\text{trough}}|$, for the case ($X = 0.5547, Y = 0.1849$) (filled circle in Fig. 5-1, $\beta = 0.923$). We chose this distance instead of the surface displacement at a fixed horizontal position because, in this case, the crest moved in the horizontal direction after the first break-up. Similar to the atomization case, break-ups took place in this near-critical case, but its break-up rate (1 break-up/10 forcing periods) is considerably reduced compared with the atomization case (1 break-up/2 forcing periods).

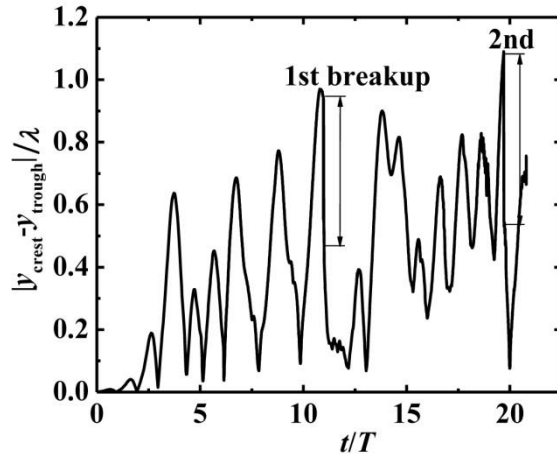


Fig. 5-10 Temporal evolution of the distance between the crest top and the trough bottom $|y_{\text{crest}} - y_{\text{trough}}|$ for the case ($X = 0.5547, Y = 0.1849$) (filled circle in Fig. 5-1, $\beta = 0.923$).

Fig. 5-11 (a) displays the vertical velocity distribution along the crest centerline at the instant when the first break-up occurs. The velocity is viewed in the laboratory reference frame. The area-averaged vertical velocity of the drop is positive, implying that the broken drop moves outward from the liquid layer.

However, the situation changes when the forcing strength is further reduced. As shown in Fig. 5-11 (b), a negative vertical velocity emerges at the top portion of the broken drop for the case ($X = 0.5043, Y = 0.1681$) (filled diamond in Fig. 5-1, $\beta =$

0.763). This may reduce the area-averaged vertical velocity in the laboratory reference frame, v_d , with which the broken drop moves outward from the liquid layer. Fig. 5-12 shows v_d as a function of the dimensionless forcing strength β . According to the criterion defined here, *i.e.*, $v_d = 0$, the onset of spray formation occurs when the dimensionless forcing strength is approximately 0.763. We therefore arrive at a threshold dimensionless forcing strength for spray formation of $\beta_c = 0.763$.

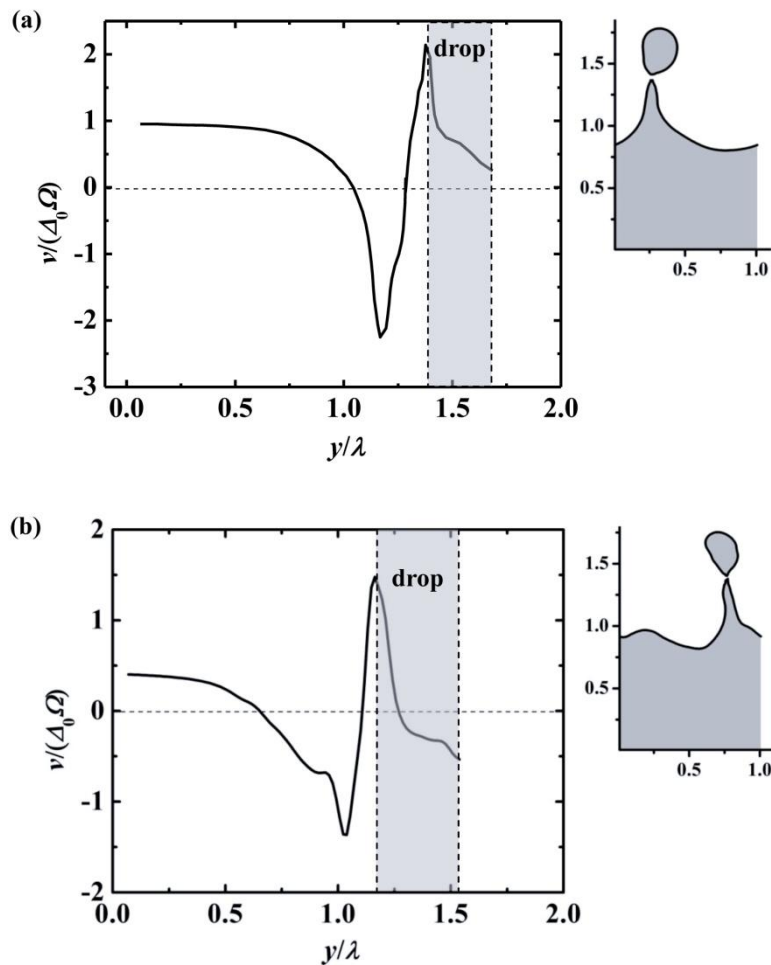


Fig. 5-11 Vertical velocity distribution along the crest centerline at the instant when the first break-up occurs for the case (a) ($X = 0.5547$, $Y = 0.1849$) at $t = 10.98T$ and (b) ($X = 0.5043$, $Y = 0.1681$) (filled diamond in Fig. 5-1, $\beta = 0.763$) at $t = 10.75T$. The velocity is viewed in the laboratory reference frame. The insets are the surface shapes at corresponding instants.

Other cases were also calculated by fixing $Y = 0.25$ and $Y = 1.0$ and changing the value of X as indicated by the cross symbols and open circles in Fig. 5-1. The cross symbols indicate cases for which no break-up occurs; the open circles correspond to

cases for which break-up occurs given the same criterion. The results show that the atomization cases are all located to the right of the dashed curve ($Y = X^3 / \beta_c$), which validates the numerical strategy adopted in the present study.

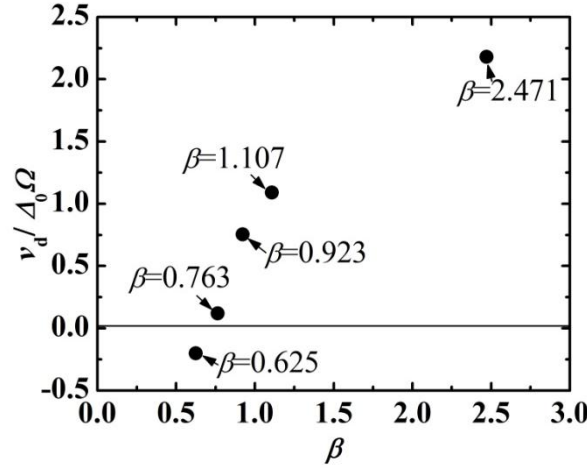


Fig. 5-12 Area-averaged vertical velocity of the broken drop at the instant of the first break-up, v_d , as a function of β . Here, v_d is viewed in the laboratory reference frame.

5.3.4 Theoretical consideration

Based on the cell model which embodies the conventional selection concept and the physics underlying the well-known Landau amplitude equation (Müller, 1994; Chen and Vinals, 1999; Aranson and Kramer, 2002), our numerical calculations starting from a small initial surface disturbance have identified the threshold forcing strength for spray formation as $\beta_c = 0.763$. The validity of this numerical result is confirmed by the following simple theoretical consideration.

As mentioned in §5.3.2, once a free ligament is formed, it may naturally disintegrate into drops. Therefore, the threshold condition primarily corresponds to the free ligament formation condition and crucially relies on the velocity enhancement of the horizontal flow oscillating at half the forcing frequency $\Omega/2$. The governing equation for u indicates that the order of magnitude of u_{\max} (maximum horizontal velocity attainable at the mid-location between the crest and trough portions in a cycle), when the convective term becomes comparable with the unsteady term, is estimated as $u_{\max} \sim \lambda \Omega / (2\pi)$ because the unsteady term and the convective term may be estimated as

$$(u_{\max} - 0)/(2\pi/(\Omega/2)/4) = u_{\max} \Omega/\pi \quad \text{and} \quad (u_{\max}/2)(u_{\max} - 0)/(\lambda/4) = 2u_{\max}^2/\lambda, \quad (5-9)$$

respectively. The order of magnitude of the vertical velocity $v_{r \max}$ (referring to the vibrating bottom substrate), produced by the impingement of this horizontal flow of depth $1/k$, takes a magnitude estimated as $v_{r \max} \sim \lambda\Omega/(\pi^2)$ using the continuity relation $(1/k)u_{\max} \sim (\lambda/4)v_{r \max}$. Therefore, we have the following expression

$$\frac{v_{r \max}}{A_0 \Omega} \sim \frac{\lambda}{\pi^2 A_0} = \frac{2}{\pi k A_0} = \frac{2}{\pi} \frac{1}{X} \quad (5-10)$$

As seen from Fig. 5-1, $X \sim 0.9$ for the atomization case $\beta = 2.471$. Therefore, Eq. (5-10) leads to $v_{r \max}/(A_0 \Omega) \sim 0.71 \sim O(1)$, which is consistent with the numerical calculation results as shown in Fig. 5-13. Note that, in the atomization case, the liquid ligament above the maximum pressure location is dynamically free from the liquid layer below the maximum pressure location. According to discussion in Chapter 4, the ligament-producing liquid velocity should be the vertical velocity $v_{r \max}$ at the maximum pressure location (dashed rectangle in Fig. 5-13), which is a direct result of the impingement of the horizontal flow satisfying the above-mentioned continuity relation. As β approaches zero, the value of Eq. (5-10) increases divergently. However, at small X , thereby, small β , the Faraday instability cannot induce the horizontal flow satisfying Eq. (5-10). Equation (5-10) is valid at X greater than a certain value, which may be estimated as follows.

An important finding from the present numerical study is that the nonlinear flow effect becomes significant when the surface deformation amplitude reaches a certain value of $\delta_{\max} = \theta\lambda = 2\pi\theta/k$ with $\theta \sim 1/8$, which corresponds to the amplitude of steady standing-wave or the distance of the maximum pressure location from the neutral surface position. The inset of Fig. 5-14 illustrates the surface displacement evolution at $x = 3\lambda/4$ for the critical stage when the crest growth in the forcing cycle under consideration results in a disintegrating liquid ligament for the first time. The origin of time $t = 0$ is taken at the maximum trough surface deformation state. The surface deformation in the previous forcing cycle is recovered in a similar way to the steady standing-wave and produces the trough surface with the amplitude of δ_{\max} due to nonlinear effects. The physics underlying the surface displacement evolution in Fig.

5-14 is easily understood by considering the opposite behavior of the neighboring interface at $x = \lambda/4$ and $5\lambda/4$. Obviously, the instant $t = 0$ must be in the stabilizing phase. $v_{r\text{ surf}}$, the vertical velocity of the surface point at $x = 3\lambda/4$, increases from zero by the action of the recovering inertial force on the neighboring crest portions in the stabilizing phase and then by the action of the inertial force on the considered crest portion in the destabilizing phase.

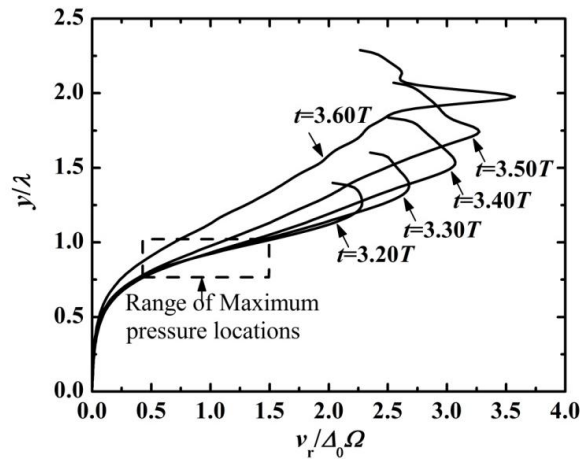


Fig. 5-13 The vertical velocity along the crest centerline ($x = 3\lambda/4$) for the atomization case $\beta = 2.471$, from the time when the maximum pressure location emerges ($t = 3.20T$) to the time when break-up are about to occur ($t = 3.60T$). The velocity refers to the vibrating bottom substrate. The maximum pressure location is present in the dashed rectangle.

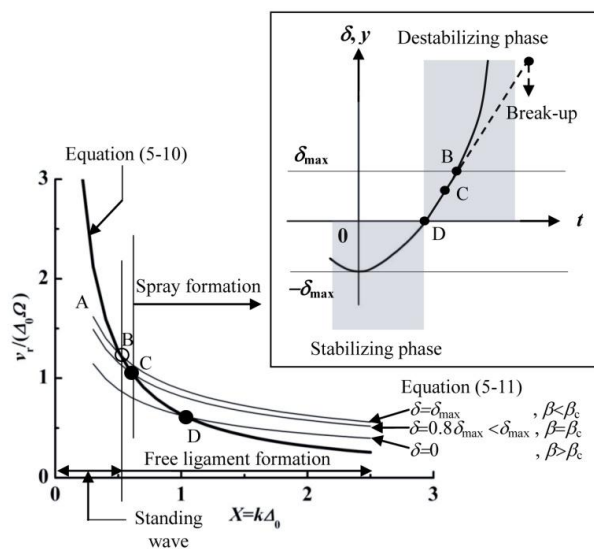


Fig. 5-14 Graphical representations of Eq. (5-10) and (5-11). The maximum vertical surface liquid velocity referring to the vibrating bottom substrate is expressed as a function of $X = k\Delta_0$. The inset expresses a temporal evolution of the surface displacement from the neutral surface plane at $x = 3\lambda/4$. The instant when the surface is at the maximum deformation is taken as $t = 0$.

For the predominant surface waves on the line $Y = X/3 < X$, the minor surface tension effect may be neglected for simplicity. Furthermore, as shown by the gray region in the inset of Fig. 5-14, we simplify the sinusoidal variation of inertial force to a rectangular wave form with uniform amplitude of $(2/\pi)\rho_1 A_0 \Omega^2$ (average value) and a positive and negative sign in the destabilizing and stabilizing phase, respectively. Since θ is small and the liquid is almost stagnant everywhere at $t = 0$, the subsequent surface displacement $\delta(t)$ obeys the Mathieu-type of equation for the simplified uniform inertial force until the convective term of the horizontal flow becomes significant. This linear equation can be easily solved analytically. Among the sub-harmonically unstable surface waves, the crest growth speed maximizes for such a specific wave number of surface wave (k) that δ becomes zero when the sign of the inertial force changes from negative to positive. Therefore, we select this wave consistent with our numerical strategy. Then, we can obtain the following relation between $v_{r \text{ surf}}$ and δ .

$$\frac{v_{r \text{ surf}}}{A_0 \Omega} = \begin{cases} \sqrt{\frac{2(2\pi\theta)^2}{\pi k A_0} \left\{ 1 + \left(\frac{\delta}{\delta_{\max}} \right)^2 \right\}} = \sqrt{\frac{\pi}{8X} \left\{ 1 + \left(\frac{\delta}{\delta_{\max}} \right)^2 \right\}} & 0 < \delta \leq \delta_{\max} \\ \sqrt{\frac{2(2\pi\theta)^2}{\pi k A_0} \left\{ 1 - \left(\frac{\delta}{\delta_{\max}} \right)^2 \right\}} = \sqrt{\frac{\pi}{8X} \left\{ 1 - \left(\frac{\delta}{\delta_{\max}} \right)^2 \right\}} & -\delta_{\max} \leq \delta \leq 0 \end{cases} \quad (5-11)$$

which is illustrated by a series of thin solid lines in Fig. 5-14. This linear solution is valid only below the thick solid line. Therefore, we are interested in the point of intersection of the thick line and each thin line, at which condition the crest has, at its root, the nonlinear stagnation point flow assumed in the derivation of Eq. (5-7) through the continuity relation and the subsequent crest development may result in a free ligament disintegrating into drops. Equating (5-11) to Eq. (5-10), we obtain the expression

$$X = \begin{cases} \frac{32}{\pi^3} \frac{1}{1 + \left(\frac{\delta}{\delta_{\max}} \right)^2} & 0 < \delta \leq \delta_{\max} \\ \frac{32}{\pi^3} \frac{1}{1 - \left(\frac{\delta}{\delta_{\max}} \right)^2} & -\delta_{\max} \leq \delta \leq 0 \end{cases} \quad (5-12)$$

Point B in Fig. 5-14 expresses the case that the linear surface displacement δ reaches the critical value δ_{\max} at an instant in the destabilizing phase and the convective effect of the horizontal flow is not negligible in the subsequent surface displacement evolution indicated by the dashed line in the inset. Thus, the crest grows to a free ligament with the maximum pressure location at $y = \delta_{\max}$. However, since the outward liquid tip velocity is reduced by the tip contraction due to surface tension, the broken drop may not have an outward velocity in the laboratory reference frame. The value of X at point B is found from Eq. (5-12) to be $X = X_B = 16/\pi^3 = 0.516$. If we apply this value to the equation $Y = X/3 = X^3/\beta$, β is evaluated as $\beta = 0.799$. These estimated values are close to the value $X = 0.5043$ for our calculation case of the critical forcing strength $\beta_c = 0.763$. At the condition $X < X_B$ ($\beta < \beta_B$), the value of Eq. (5-10) is larger than that of Eq. (5-11) and the attainable maximum horizontal velocity is determined by the maximum vertical velocity (5-11) (line AB in Fig. 5-14). In reality, the convective term in the horizontal flow is effective to a degree, even if the horizontal velocity does not reach the value of (5-10). As a result, the phase retardation caused by the convective flow results in a steady standing-wave state as described in §5.3.1. In our calculation for $\beta = 0.405$, in which the steady standing-wave is eventually realized, $X = 0.3675$. On the other hand, at $X > X_B$, the crest is influenced by the nonlinear flow at smaller δ . This means that the crest top may have a larger outward velocity in the laboratory reference frame. Correspondingly, the drop produced from the free ligament has a larger outward velocity. For example, the intersection point realized at the condition $\delta = 0$ in Eq. (5-11) yields a value of $X = 1.03$ and $\beta = 3.18$, which is consistent with our calculation result for the atomization case of $X = 0.9075$ and $\beta = 2.471$.

5.3.5 Three-dimensional modification

The problem transforms to a 3D configuration when we consider a cuboid fluid region which satisfies the cyclic condition at the two planes (faces) separated by the same distance as the width λ in the z -direction. The linear surface deformation is expressed in the form of $\delta(t)\sin(k_{3D} x)\sin(k_{3D} z)$ and δ is governed by the same Mathieu equation. The difference from the 2D case is only a slight modification of wavelength by $k = \sqrt{2}k_{3D}$. As a result, the evolution of the 3D linear flow field is the

same as the 2D case. Even at the nonlinear evolution stage, the 2D governing equation (5-8) can be transformed to the 3D governing equation by simply multiplying $1/\sqrt{2}$ by the convective term on the left-hand side and $1/2$ by the interfacial term on the right-hand side. Therefore, these modifications do not significantly affect the order of magnitude of β for the emergence of the maximum pressure point at the ligament root. Once the free liquid ligament is formed, it disintegrate into drops by the end-pinching, which is the same as the disintegration of a water jet issued from an orifice under gravity (Stone et al., 1986; Stone and Leal, 1989; Schulkes, 1994; Umemura, 2011). Importantly, the effect of circumferential surface tension lacking in 2D configuration only plays a secondary role in both free ligament formation and end-pinching processes. Therefore, although it is more accurate to consider the free ligament and end-pinching process in 3D configuration, the numerically determined threshold forcing strength β_c in 2D calculations is expected to be accurate to the same order of magnitude for the 3D case.

5.3.6 Interpretation of Lang's equation

When a standing wave is realized due to the Faraday instability in experiments, we can readily identify its frequency and wavelength. On the other side, it is difficult to identify the predominant surface wavelength in an atomizing surface state, except near the critical case. Nevertheless, it is relatively easy to measure the size distribution of broken drops. Lang's equation (5-2) correlates such experimental results, indicating that drops are mainly generated from surface waves with wavelengths close to the wavelength $\lambda = \lambda_0$ satisfying the condition $Y = 0.25$. Analytical approaches have been reported to explain this correlation; however, in most such studies, it is misunderstood in the interpretation of the Mathieu equation solution that the sub-harmonic surface deformation occurs only for those surface waves on the line $Y = 0.25$ in Fig. 5-1, although all of the surface waves in the sub-harmonic unstable region oscillate at half the forcing frequency. Therefore, results that support Lang's equation are already prepared by the misunderstanding themselves. It is also important to consider a predominant surface wave realizable in each realization of experiment and its nonlinear evolution. Based on our work, Lang's equation is interpreted as follows. On the line $Y = X/3$ in Fig. 5-1, the range of Y -values that result in the predominant sub-harmonic

surface wave is $0.1 < (2\pi)^3 \sigma / (\lambda_m^3 \rho_1 \Omega^2) < 0.6$. Thus, we have the relationship $0.75 < \lambda_m / \lambda_0 < 1.36$. This range is further narrowed around $\lambda_m / \lambda_0 = 1$ ($0.75 < \lambda_m / \lambda_0 < 1.14$) when we confine our interest to the case of spray formation ($0.168 < (2\pi)^3 \sigma / (\lambda_m^3 \rho_1 \Omega^2) < 0.6$, where the lower limit 0.168 is determined from the intersection point of $Y = X/3$ and $\beta = 0.763$ curves, and the upper limit 0.6 is determined from the intersection point of $Y = X/3$ and the upper boundary curve of the sub-harmonic instability region). Therefore, the predominant surface wavelength of the sub-harmonically oscillating surface is close to λ_0 and results in the Lang's equation (5-2) even for the spray formation case at $\beta > \beta_c$ until the harmonic mode or higher mode prevails at much higher β .

5.4 Effects of the initial disturbance

Until now, all the calculations we conducted are initiated with a small surface disturbance. A large initial disturbance is able to cause a single drop formation even at a forcing strength β much smaller than $\beta_c = 0.763$, as shown below. However, such drop formation does not occur successively, and the steady atomization is not realized.

To study the effect of the initial disturbance on the drop formation, we focused on the case ($X = 0.628$, $Y = 1$) ($\beta = 0.248 < \beta_c$). When we started the calculation with the same small initial surface disturbance as used before, the amplitude of surface deformation is limited to 0.015λ . Therefore, no drop forms.

We calculated the same case ($X = 0.628$, $Y = 1$) using a large surface deformation shown in the inset of Fig. 5-15 (a), as the initial surface shape, and setting the initial velocity and pressure to zero. The only difference between the two sets of calculations is that the initial input energy of the latter case, introduced in the form of the surface energy, is much larger than that of the former case, introduced in the form of the kinetic energy. Fig. 5-15 (a) displays the temporal evolution of the distance between the crest top and the trough bottom. From Fig. 5-15 (a), we can see that drops are indeed generated; indicating that the initially large surface deformation is capable of creating drops even under weak forcing. Fig. 5-15 (b) shows the temporal evolutions of the first three spatial modes by the Fourier decomposition of the instantaneous surface deformation. The two abrupt descents in the graph of the zeroth mode

correspond to two break-ups.

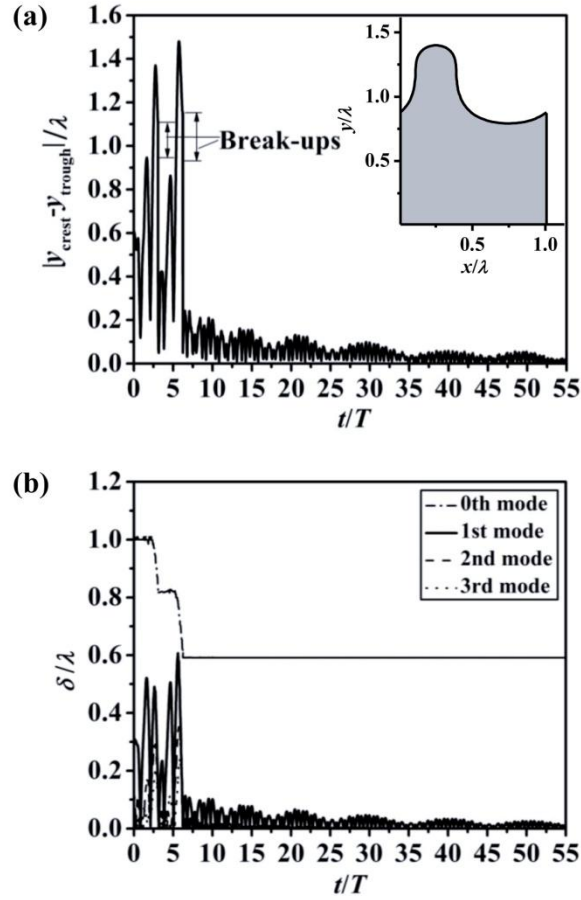


Fig. 5-15 Calculation results for the case ($X = 0.628$, $Y = 1$) with the initial surface shape shown in the inset in (a). (a) Temporal evolution of the distance between the crest top and the trough bottom $|y_{\text{crest}} - y_{\text{trough}}|$. The surface deformation is no longer enhanced sufficiently enough to trigger more break-ups after the first two break-ups due to the large initial surface deformation. (b) Temporal evolution of the first three spatial modes and the zeroth mode of the surface deformation.

However, after the first two break-ups, the surface deformation is no longer sufficiently amplified to cause more break-ups. Instead, the magnitude of surface deformation amplitude is restrained at about 0.025λ , which is on the same order ($\sim O(10^{-2})\lambda$) to the surface deformation amplitude obtained in the calculation using the small initial disturbance. This tells us that the steady atomization cannot be realized in the case ($X = 0.628$, $Y = 1$).

The important indication of this calculation is that the initial excess surface energy is removed from the liquid layer by the formation of broken drops. As a result, the surface deformation eventually settles down to the modulated standing-wave state

specified by the weak forcing, although energy cascades to higher-order waves. On one hand, if the external forcing is not strong enough, a single break-up may occur due to the large initial energy input; however, the steady atomization cannot be realized. On the other hand, even though the initial energy input is small, the steady atomization can still be realized by obtaining energy from the inertial force if the external forcing is strong enough. Whether the spray can be formed or not is independent of the initial condition.

Chapter 6

Dynamics of ligament formation due to RT instability

The RT instability can be considered as a limit case of Faraday instability when $\Delta_0 \rightarrow \infty$ and $\Omega \rightarrow 0$. In this chapter, we discuss the detailed dynamics of the ligament formation from a liquid layer due to RT instability, with the focus on the analytic expressions for the characteristic quantities that can bridge the ligament formation due to RT instability and jet emanation from an orifice injector under normal gravity conditions. First, the code is validated on capturing the major dynamics associated with the RT instability by comparing with other's work. Second, the overall dynamics associated with the RT instability are discussed. The local maximum pressure location due to the impinging flow is formed at the ligament root, which is similar to the Faraday instability. Different from the Faraday instability, the flow near the surface is a steady flow in RT instability. Then, the characteristic quantities associated with the steady flow are analyzed based on the detailed information on the velocity and pressure fields. Finally, the ligament disintegration due to RT instability is bridged to the laboratory low-speed jet experiments.

6.1 Numerical validation

To validate our calculation code, we compared the numerical results obtained by the present CLSVOF method with the results of **Baker et al. (1980)** under the same condition. Eliminating the viscosity and surface tension, they utilized the vortex sheet method to calculate the temporal evolutions of the amplitudes of the spike and the bubble for the case $a_s = 1$ with the initial surface displacement amplitude $\xi_0 = 0.1\lambda$. The results are shown as the solid lines in Fig. 6-1. The linear solution, shown as the dashed line in Fig. 6-1, is also presented for reference. To match the calculation condition of **Baker et al. (1980)**, we dropped the surface tension term \mathbf{F}_s in Eq. (3-1). In our calculation, the temporal evolutions of the amplitudes of the spike and the bubble correspond to the temporal evolutions of the absolute values of the surface

displacements $|\xi|$ at $x=\lambda/4$ and $x=3\lambda/4$, respectively, which are shown as the open circles in Fig. 6-1. Fig. 6-1 shows that the results obtained by our calculation code are in excellent agreement with the results of **Baker et al. (1980)**.

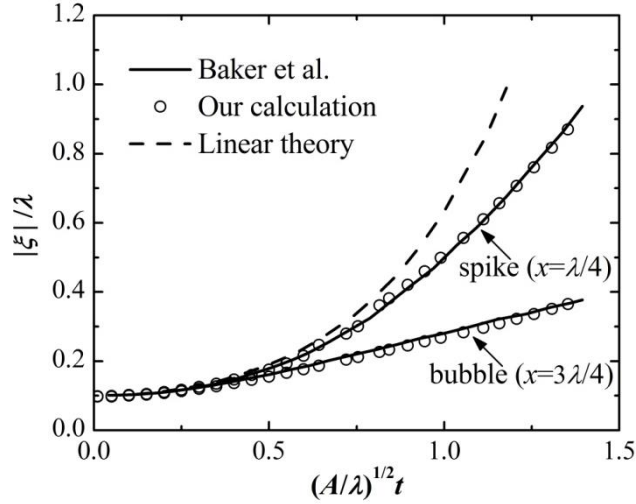


Fig. 6-1 Comparison with the numerical results of **Baker et al. (1980)**.

6.2 Overall dynamics

Two time scales existed in the RT instability considered in this dissertation: the time scale associated with inertia $t_A = \sqrt{\lambda/A}$, and that associated with capillarity $t_\sigma = \sqrt{\rho_1 \lambda^3 / \sigma}$. Because we were interested in ligament formation, in which the inertial effect overwhelms the capillary effect ($t_A < t_\sigma$), t_A was a more suitable timescale. In this case, the governing equations (Eq. (3-1)) were made dimensionless by the length scale $l_{ch} = \lambda$, the time scale $t_{ch} = \sqrt{\lambda/A}$, the velocity scale $u_{ch} = \sqrt{\lambda A}$, and the pressure scale $p_{ch} = \rho_1 A \lambda$. The dimensionless quantities are denoted with a superscript * hereafter. As such, we obtained a dimensionless parameter A^* characterizing the RT instability problem:

$$A^* = \frac{\rho_1 \lambda^2 A}{\sigma}. \quad (6-1)$$

This represents the ratio of the destabilizing inertial force to the stabilizing capillary force. To assess the effect of A^* on the characteristic quantities associated with

ligament formation due to single-mode RT instability, we carried out computations by varying the dimensionless parameter A^* over a strict range from $2.4\pi^3$ to $8.8\pi^3$ using an interval of $0.8\pi^3$. For all cases, the initial amplitude of the vertical velocity disturbances on the surface was set to be identically small ($v_{s0}^* = 0.001$). Calculation of each case was terminated when the liquid ligament tip reached the top boundary of the calculation domain.

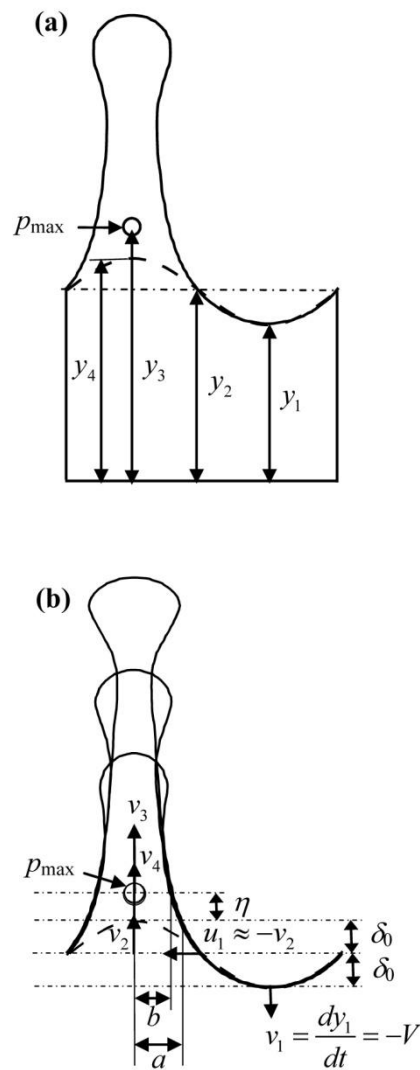


Fig. 6-2 Features of the ligament formation from a liquid layer due to single-mode RT instability. Panel (a) shows the vertical coordinates of interest to be discussed in the following text. Panel (b) is the superimposition of the trough surfaces at different instants after the local maximum pressure location is formed. The quantities to be discussed later are also shown in Panel (b).

Fig. 6-2 (a) and (b) show the features of the ligament formation from the liquid

layer at the late-time stage due to a single-mode RT instability. All interfacial profiles depicted in the figure show the one-run calculation results at different instants. A localized maximum pressure location formed at the crest root, above which a conical liquid ligament, dynamically freed from the bulk liquid layer motion, was created. This phenomenon has also been observed in the study on ligament formation from a liquid layer due to a Faraday instability in Chapter 4. For the large Atwood numbers considered in the present case, no roll-up due to a secondary Kelvin–Helmholtz (KH) instability was evident at the ligament tip (Baker et al., 1980; Ramaprabhu et al., 2012).

Several interesting phenomena occurred when we superimposed the trough bottoms at different instants after the formation of the maximum pressure location (Fig. 6-2 (b)). The shapes of the trough surface at different instants appeared to be the same and coincided perfectly with a sinusoidal trough surface of constant amplitude δ_0 , depicted by the dashed line in Fig. 6-2 (b). The counterpart of this sinusoidal trough in the crest portion, hereafter referred to as the artificial sinusoidal crest, is also shown in Fig. 6-2 (b). The maximum pressure locations at different instants, indicated by the open circles in Fig. 6-2 (b), coincided with each other, and the distance between the maximum pressure location and the artificial sinusoidal crest top η remained constant over time.

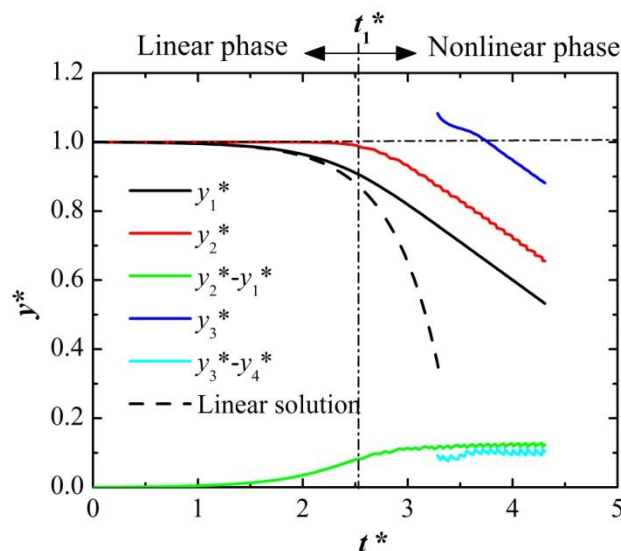


Fig. 6-3 Temporal evolution of y_1^* , y_2^* , $y_2^* - y_1^*$, y_3^* and $y_3^* - y_4^*$ which are defined in Fig. 6-2(a). The linear solution of y_1^* depicted as the dashed curve is also shown in the figure for reference.

For the case $A^* = 4.8\pi^3$, Fig. 6-3 shows the temporal evolutions of the vertical coordinates of the trough bottom: y_1^* (referred to as the bubble tip in previous literature), the neutral surface position y_2^* (the vertical coordinate of the surface at $x^* = 0.5$), and the local maximum pressure location y_3^* after it appears. The temporal evolution of y_1^* from linear theory, the distance between the neutral surface and the trough bottom $y_2^* - y_1^*$, and the distance between the maximum pressure location and the artificial crest top $y_3^* - y_4^*$ are also depicted in Fig. 6-3 for reference. These characteristic quantities exhibited similar behavior for other A^* -values as well.

In the initial stages, the surface deformation strictly followed the linear solution (dashed curve in Fig. 6-3):

$$y_1 = h_0 - \frac{v_{s0}}{\sqrt{kA - \frac{\sigma k^3}{\rho_1}}} \sinh \left(\sqrt{kA - \frac{\sigma k^3}{\rho_1}} t \right). \quad (6-2)$$

As the surface amplitude became large, nonlinearity gradually became more dominant and reduced the growth rate. Eventually, the trough bottom moved down with a constant velocity V^* . The neutral surface height y_2^* , which retains its value at the equilibrium height $h_0^* = 1$ in linear theory, began to decrease with the same velocity as y_1^* after a certain time t_1^* . This resulted in a constant amplitude for the sinusoidal surface δ_0^* , as shown in Fig. 6-2 (b). Note that the steady behavior shown in Fig. 6-3 had no relation to the effect of the bottom substrate because the distance between the lowest position of the surface and the bottom substrate was $y_1^* = y_1/\lambda \approx 0.5$; this was the case even at the end of the calculations, providing a distance still larger than the dimensionless depth associated with surface deformation $1/k^* = 1/(2\pi)$. We approximately divided the development into two phases: the linear phase for $t^* < t_1^*$ and the nonlinear phase (the late-time stage) for $t^* > t_1^*$, as shown in Fig. 6-3. Furthermore, y_3^* also decreased in accordance with y_1^* and y_2^* , which indicated that the maximum pressure location moved downward with the trough surface as a whole.

From Fig. 6-3, it is shown that $y_2^* - y_1^*$ and $y_3^* - y_4^*$ both reached constant values δ_0^* and η^* , respectively. Fig. 6-4 shows the dependence of the constant

amplitude of the sinusoidal surface δ_0^* on the dimensionless parameter A^* . δ_0^* was independent of A^* and had the same value of 0.125. Fig. 6-5 shows the dependence of the constant distance between the maximum pressure location and the artificial sinusoidal crest top, η^* , on the dimensionless parameter A^* . The coordinates are shown using a logarithmic scale. As A^* increased, η^* decreased, as follows:

$$\eta^* = \frac{c_1}{\sqrt{A^*}}, \quad (6-3)$$

where $c_1 = 1.26$ is a constant obtained by numerical results.

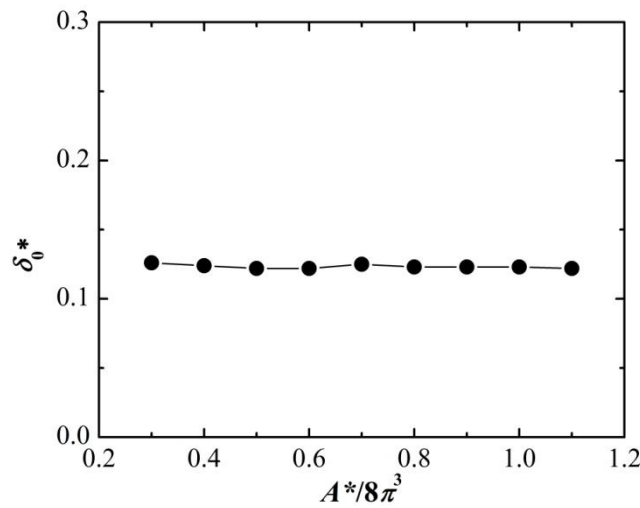


Fig. 6-4 Dimensionless amplitude of the sinusoidal surface, δ_0^* , as a function of the dimensionless parameter A^* .

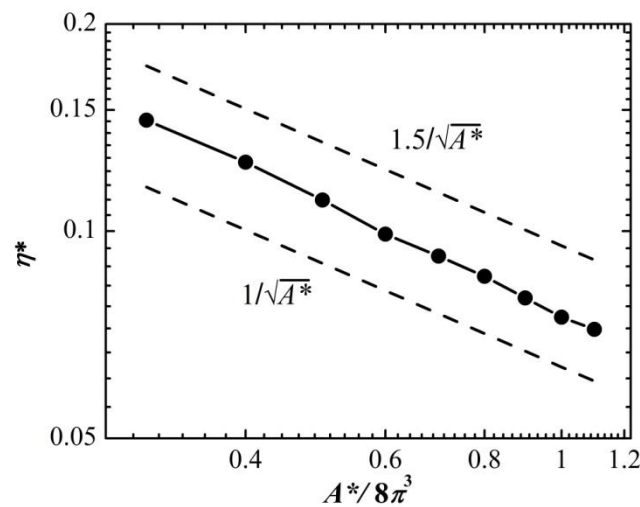


Fig. 6-5 Dimensionless distance between the maximum pressure location and the artificial sinusoidal crest top, η^* , as a function of the dimensionless parameter A^* . The dashed lines are depicted for reference. The coordinates are on logarithm scales.

6.3 Characteristic quantities associated with steady flow

6.3.1 Constant descending velocity of the trough surface V^*

The calculation results in Fig. 6-2 (b) and Fig. 6-3 indicated that not only the liquid trough bottom, but the entire trough surface, descended with a constant velocity during the late-time stage of the instability. We first examined the descent velocity by comparing it with past research. Fig. 6-6 shows the temporal evolution of the dimensionless vertical velocity of the trough bottom v_1^* (see Fig. 6-2 (b)) for the cases $A^* = 3.2\pi^3$, $4.8\pi^3$, $6.4\pi^3$, and $8.0\pi^3$. We observed that v_1^* eventually reached a constant value V^* satisfying

$$V^* = \frac{V}{\sqrt{A\lambda}} = c_2, \quad (6-4)$$

where c_2 is a constant. The constant value determined by the present numerical calculations was $c_2 = 0.225$. This value is exactly the same as that obtained numerically by **Baker et al. (1980)** using the vortex sheet method. In the case of a bubble rising under gravity in a vertical tube with parallel walls, **Birkhoff and Carter (1957)** showed that the dimensionless constant velocity of a rising bubble $V/\sqrt{gD} = 0.215 - 0.25$. The approximate potential flow model (**Goncharov, 2002**) and the drag-buoyancy model (**Oron et al., 2001**) both suggest an asymptotic velocity for the bubble tip $V/\sqrt{A\lambda} = 0.23 \pm 0.01$ given a 2D single-mode RT instability at $a_i = 1$ (see Eq. (2-3)); this is consistent with the present numerical result. As will be discussed in §6.4, the magnitude V characterizes the velocity of the liquid entering the freed liquid ligament at the maximum pressure location. In this study, we devised another approach to determine the constant velocity at the trough bottom based on detailed information about the pressure and velocity fields. This approach is described in the following.

Along the trough centerline ($x^* = 0.25$), the dimensionless governing equation of the vertical velocity in the liquid phase is

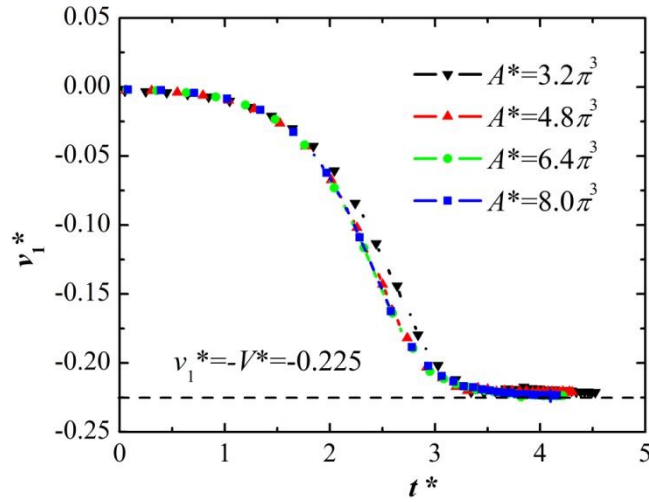


Fig. 6-6 Temporal evolutions of the dimensionless vertical velocity at the trough bottom v_1^* for the cases $A^*=3.2\pi^3$, $4.8\pi^3$, $6.4\pi^3$ and $8.0\pi^3$. v_1^* in all the cases reaches a steady value -0.225 .

$$\frac{\partial v^*}{\partial t^*} + v^* \frac{\partial v^*}{\partial y^*} = -\frac{\partial p^*}{\partial y^*} + 1, \quad (6-5)$$

because the horizontal velocity vanishes along this centerline. Fig. 6-7 (a) shows the dimensionless pressure distribution along the trough centerline ($x^*=0.75$) at $t^*=3.41$, 3.66 , 3.90 , and 4.14 in the nonlinear phase for the case $A^*=4.8\pi^3$. The dimensionless pressure increased accordingly as the trough surface descended. Transforming the vertical coordinate y^* into $\zeta^*=y^*-y_1^*$, we obtained Fig. 6-7 (b), in which all of the pressure curves are coincided; this indicated that the time-dependent pressure $p^*(x^*, y^*, t^*)$ can be expressed as $p^*(x^*, \zeta^*)$. Furthermore, from Fig. 6-2 and Fig. 6-3, we know that the sinusoidal surface as a whole (including the artificial crest) and the maximum pressure location descend with a constant velocity of magnitude V^* at the late-time stage of the instability. Sitting on the surface trough bottom, the liquid flow below the maximum pressure location is a steady flow. The vertical velocity can hence be expressed as $v^*(x^*, y^*, t^*) = v^*(x^*, \zeta^*)$, which reduces Eq. (6-5) to

$$(V^* + v^*) \frac{\partial v^*}{\partial \zeta^*} = -\frac{\partial p^*}{\partial \zeta^*} + 1. \quad (6-6)$$

Integrating Eq. (6-6) along the trough centerline with respect to ζ^* from $\zeta_0^* = -y_1^*$ (corresponding to $y^*=0$) to $\zeta_1^* = 0$ (corresponding to $y^*=y_1^*$) leads to

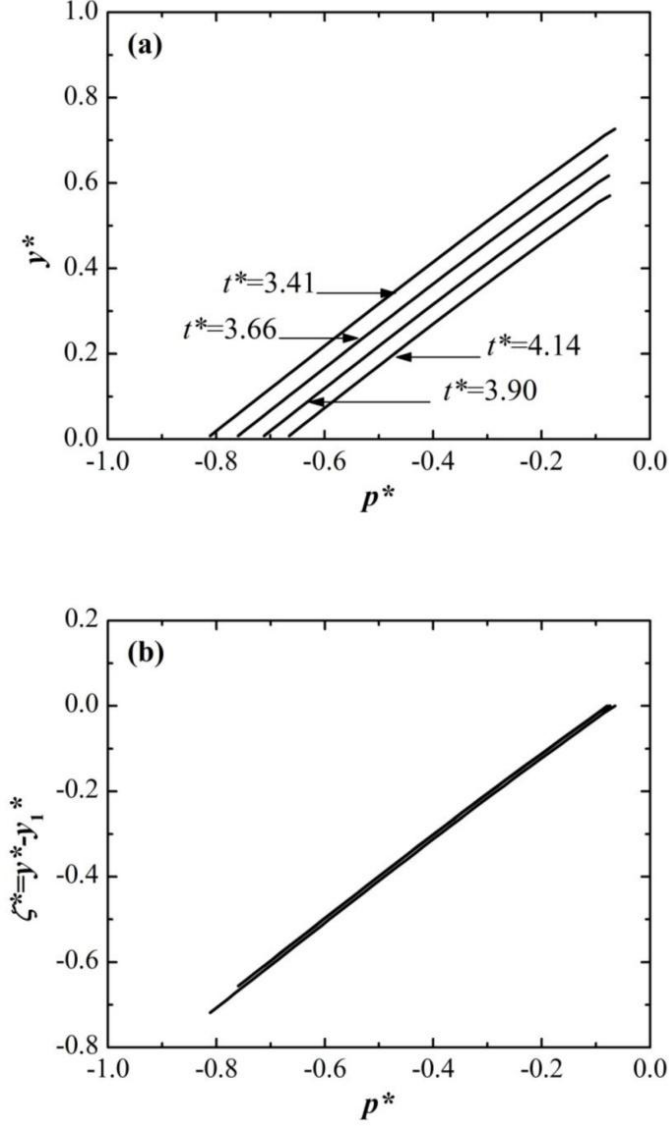


Fig. 6-7 Vertical distribution of the dimensionless pressure along the trough centerline ($x^*=0.75$) at $t^*=3.41, 3.66, 3.90$ and 4.14 in the nonlinear phase for the case $A^*=4.8\pi^3$. Panel (b) is drawn by transforming the vertical coordinate y^* in Panel (a) into $\zeta^*=y^*-y_1^*$.

$$-\frac{1}{2}V^{*2} = p^*(x^*=0.75, \zeta_0^*) - p^*(x^*=0.75, \zeta_1^*) + y_1^*. \quad (6-7)$$

Neglecting the capillary pressure on the surface trough bottom ($p^*(x^*=0.75, \zeta_1^*)=0$), we obtain

$$p^*(x^*=0.75, \zeta_0^*) = -\frac{1}{2}V^{*2} - y_1^*. \quad (6-8)$$

Fig. 6-8 shows the dimensionless pressure distribution along the crest centerline ($x^*=0.25$) at $t^*=3.41, 3.66, 3.90$, and 4.14 in the nonlinear phase for the case

$A^* = 4.8\pi^3$. The pressure in the liquid ligament region above the maximum pressure location (filled circles) relaxed to that of the surrounding gas. Thus, the pressure p^* and its vertical gradient $\partial p^*/\partial y^* (= \partial p^*/\partial \zeta^*)$ in that particular liquid ligament region both approached zero. The distribution of the pressure near the substrate along the crest centerline was identical to that along the trough centerline.

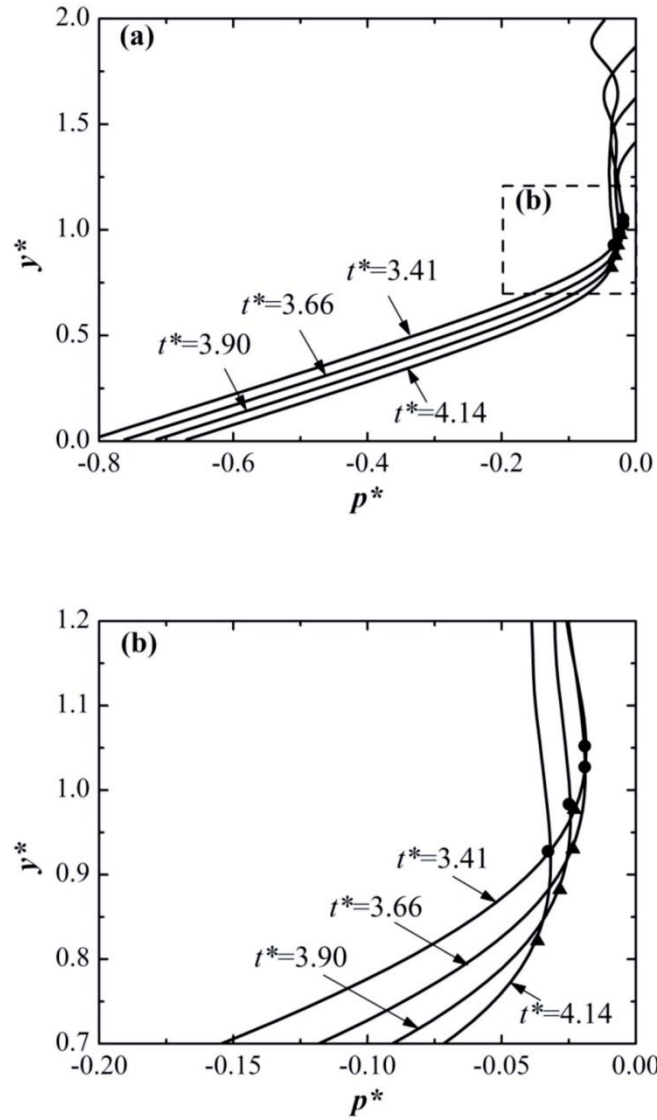


Fig. 6-8 Vertical distribution of the dimensionless pressure along the crest centerline ($x^* = 0.25$) at $t^* = 3.41, 3.66, 3.90$ and 4.14 in the nonlinear phase for the case $A^* = 4.8\pi^3$. Panel (b) is an enlarged view of the dashed square in Panel (a). The dimensionless pressure gradient $dp^*/dy^* \ll 1$ and $p^* \approx 0$ in the vicinity of the artificial crest top y_4^* (denoted by the filled triangles) and the maximum pressure location (denoted by the filled circles).

Equations (6-5) and (6-6) are also valid along the crest centerline below the maximum pressure location. Integrating Eq. (6-6) along the crest centerline with respect to ζ^* from $\zeta_0^* = -y_1^*$ (corresponding to $y^* = 0$) to $\zeta_4^* = y_4^* - y_1^*$ (corresponding to $y^* = y_4^*$) leads to

$$V^* v_4^* + \frac{1}{2} v_4^{*2} = p^*(x^* = 0.25, \zeta_0^*) - p^*(x^* = 0.25, \zeta_4^*) + y_4^*. \quad (6-9)$$

Because the steady flow associated with ligament formation was restricted within a limited distance from the surface, the pressure at the bottom of the crest centerline, as shown in Fig. 6-7 (a) and Fig. 6-8 (a), was identical to that at the bottom of the trough centerline,

$$p^*(x^* = 0.25, \zeta_0^*) = p^*(x^* = 0.75, \zeta_0^*). \quad (6-10)$$

From Fig. 6-8 (b), we can see that the pressure at the artificial crest top y_4^* denoted by the filled triangle, which is located near the maximum pressure location, was close to zero,

$$p^*(x^* = 0.25, \zeta_4^*) \approx 0. \quad (6-11)$$

Moreover, as shown in Fig. 6-9, the upward vertical velocity of the liquid element at the artificial crest top v_4^* satisfied

$$v_4^* \approx 2V^*, \quad (6-12)$$

which is a natural result of mass conservation if we consider the fact that the artificial crest surface and the trough surface moves downward as a whole. Substituting Eq. (6-8) and Eqs. (6-10)–(6-12) into Eq. (6-9) yields

$$V^* = \frac{2}{3} \sqrt{\delta_0^*}, \quad (6-13)$$

The numerical results (Fig. 6-4) show that the dimensionless amplitude δ_0^* is independent of the dimensionless parameter A^* , and retains its value at 0.125. The physical approach to determine this value of δ_0^* will be discussed in §6.3.2. The value of V^* obtained from Eq. (6-13) is 0.236, which agrees well with Eq. (6-4) and the value derived from the approximate potential flow model (**Goncharov, 2002**) and

the drag-buoyancy model (Oron et al., 2001).

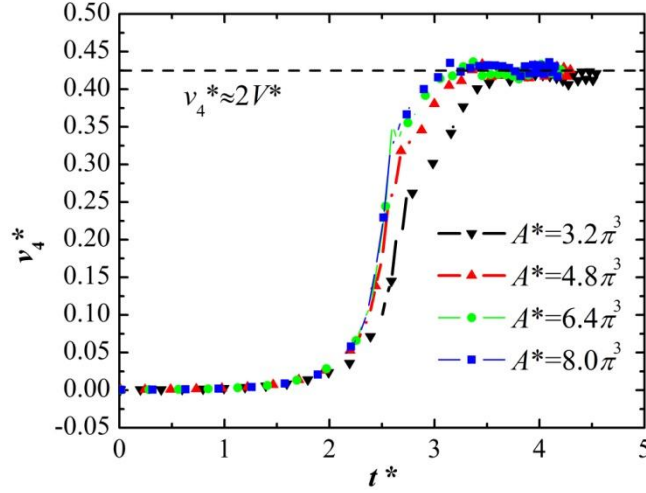


Fig. 6-9 Temporal evolutions of the dimensionless vertical velocity at the artificial sinusoidal crest top v_4^* for the cases $A^*=3.2\pi^3$, $4.8\pi^3$, $6.4\pi^3$ and $8.0\pi^3$. v_4^* in all the cases reaches a steady value $0.425 \approx 2V^*$.

Summarizing, the physics underlying the steadiness during the late-time stage of an RT instability can be understood as follows. In the linear phase, the upward inertial force causes the pressure in the crest portion of the initial disturbance to be lower than that in the trough portion, which induces liquid flow from the trough to the crest. The growth of the crest further increases the pressure difference, and thus increases the flow velocity from the trough portion. However, as the liquid velocity increases large enough such that the convective term can no longer be neglected, the impinging flow increases the pressure in the crest root region. On the other hand, the pressure in the elongated crest (ligament) region relaxes to that of the surrounding gas (except at the ligament tip due to surface tension). As a result, a maximum pressure location appears at the ligament root, and the bulk liquid layer is dynamically freed from the long liquid ligament above the maximum pressure location. This means that the upward inertial force that drives the liquid concentrated from the trough portion outward is only effective in the ligament root region. A continuous ligament with a steady flow below the artificial sinusoidal surface is realized, as the effective inertial force maintains the concentrated liquid flow against the reverse pressure gradient due to the formation of the maximum pressure location. Therefore, the key mechanism is that the range of the

upward inertial force driving the bulk liquid layer is restricted to the ligament root region by the formation of the maximum pressure location there.

6.3.2 Amplitude of the sinusoidal surface δ_0^*

Besides the constant velocity V^* , with which the sinusoidal surface and the maximum pressure location descends, another characteristic quantity associated with steady flow at the ligament root region is the A^* -independent amplitude of the sinusoidal surface δ_0^* , corresponding to the thickness of the ligament root region in which the upward inertial force is effective and a steady flow is formed. In this section, we will quantitatively determine δ_0^* based on the numerical information about the pressure and velocity fields.

The nonlinear kinetic condition on the surface is

$$v_s^* = \frac{\partial h^*}{\partial t^*} + u_s^* \frac{\partial h^*}{\partial x^*}, \quad (6-14)$$

where $h^*(x^*, t^*)$ is the surface height of the trough portion, and u_s^* and v_s^* are the horizontal and vertical components of the surface velocity vector. The second term on the right side of the equation is dropped in the linear analysis. In the linear phase of the present calculation, this approximation is reasonable because the horizontal surface velocity u_s^* and the surface gradient $\partial h^*/\partial x^*$ are small; however, it is no longer valid for the nonlinear phase, when the product of u_s^* and $\partial h^*/\partial x^*$ becomes significant.

Fig. 6-10 shows the temporal evolution of the x -coordinate where $v_s^* = 0$. The vertical surface velocity vanished at the neutral surface point ($x^* = 0.5, y^* = y_2^*$) throughout the entire process. In the nonlinear phase, as discussed above, the shape of the trough surface was approximated as a sinusoidal curve of constant amplitude δ_0^* .

Thus, the surface height of the trough portion ($x^* \geq 0.5$) can be expressed as $h^*(x^*, t^*) = y_2^*(t^*) + \delta_0^* \sin(2\pi x^*)$. At the neutral surface point ($x^* = 0.5, y^* = y_2^*$), Eq. (6-14) is reduced to

$$\frac{dy_2^*}{dt^*} = 2\pi u_1^* \delta_0^* \Rightarrow \delta_0^* = -\frac{2\pi u_1^*}{V^*}, \quad (6-15)$$

where $u_1^* = u_s^*(x^* = 0.5)$ is the horizontal surface velocity at the neutral surface point. To determine the value of δ_0^* , it is necessary to first derive the expression for u_1^* . u_1^* has the opposite sign to the vertical velocity at the same level on the crest centerline, $v_2^* = v^*(x^* = 0.25, y^* = y_2^*)$, and nearly the same magnitude as v_2^* , as shown in Fig. 6-11, which presents the temporal evolutions of $|u_1^*|$ and $|v_2^*|$ for the case $A^* = 4.8\pi^3$. This relationship between $|u_1^*|$ and $|v_2^*|$ also holds for other A^* -value cases.

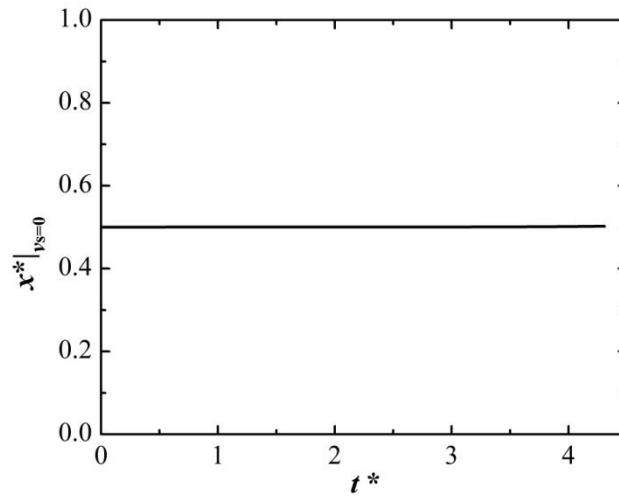


Fig. 6-10 Temporal evolution of the x^* -coordinate where the vertical velocity vanishes on the surface ($v_s^* = 0$).

In the vicinity of the artificial crest top, as depicted by the filled triangles in Fig. 6-8, the vertical pressure gradient $|\partial p^*/\partial \zeta^*| = |\partial p^*/\partial y^*| \ll 1$. Thus, the term $-\partial p^*/\partial \zeta^*$ can be dropped in Eq. (6-6) between $\zeta_2^* = y_2^* - y_1^*$ and $\zeta_4^* = y_4^* - y_1^*$ along the crest centerline ($x^* = 0.25$):

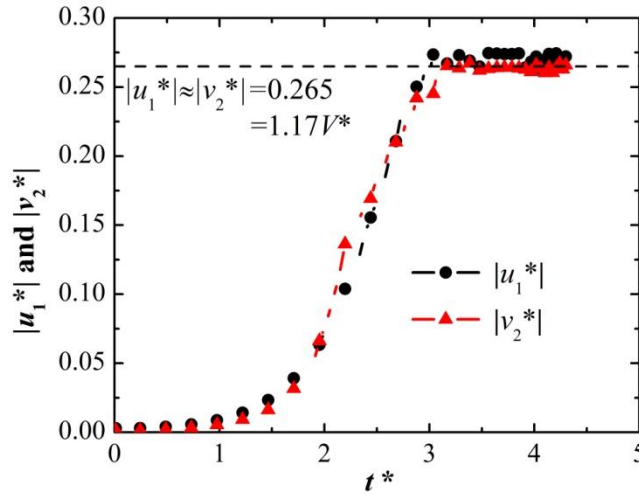


Fig. 6-11 Temporal evolutions of the magnitude of the dimensionless vertical velocity ($|v_2^*|$) at ($x^* = 0.25, y^* = y_2^*$) and the horizontal velocity ($|u_1^*|$) at ($x^* = 0.5, y^* = y_2^*$) for the case $A^* = 4.8\pi^3$.

$$(V^* + v^*) \frac{\partial v^*}{\partial \zeta^*} = 1. \quad (6-16)$$

Integrating Eq. (6-16) with respect to ζ^* from ζ_2^* to ζ_4^* leads to

$$V^*(v_4^* - v_2^*) + \frac{1}{2}(v_4^{*2} - v_2^{*2}) = \zeta_4^* - \zeta_2^* = \delta_0^*. \quad (6-17)$$

Substituting Eq. (6-12) and Eq. (6-13) into Eq. (6-17) yields

$$2v_2^{*2} + 4V^*v_2^* - 7V^{*2} = 0, \quad (6-18)$$

which has solutions

$$v_2^* = \left(\pm \frac{3}{2}\sqrt{2} - 1 \right) V^*. \quad (6-19)$$

The solution $v_2^* = (-3\sqrt{2}/2 - 1)V^*$ is dropped because v_2^* is positive. As a result, $v_2^* = (3\sqrt{2}/2 - 1)V^* = 1.12V^*$ is the physical solution to Eq. (6-18). This value agrees well with the numerical results ($v_2^* = 1.17V^*$), as shown in Fig. 6-11. Because $u_1^* \approx -v_2^*$, from Eq. (6-15), we can obtain the following expression for δ_0^* :

$$\delta_0^* = \frac{1}{2\pi(3\sqrt{2}/2 - 1)} = 0.142, \quad (6-20)$$

which is independent of A^* . The value of δ_0^* obtained from Eq. (6-20) is slightly larger than the numerical result ($\delta_0^* = 0.125$), which results from the magnitude of v_2^* being slightly smaller than that of u_1^* ($= 1.2V^*$).

6.3.3 Velocity v_3^* and liquid ligament width $2b^*$ at the maximum pressure location

To link low-speed liquid jet theory with the present RT instability, it is necessary to determine the velocity v_3^* and the liquid jet width $2b^*$ at the maximum pressure location.

In the vicinity of the artificial crest top y_4^* , as discussed in §6.3.2, the vertical pressure gradient can be neglected ($\ll 1$). Thus, the vertical gradient of the vertical velocity $\partial v^*/\partial y^*$ ($= \partial v^*/\partial \zeta^*$) at the artificial crest top ($x^* = 0.25, y^* = y_4^*$) can be evaluated from Eq. (6-16):

$$\frac{\partial v^*}{\partial y^*} = \frac{\partial v^*}{\partial \zeta^*} = \frac{1}{V^* + v_4^*} = \frac{1}{3V^*}. \quad (6-21)$$

We assumed that the vertical velocity is distributed linearly with respect to the slope β between $y^* = y_4^*$ and $y^* = y_3^*$. Then,

$$v_3^* = v_4^* + \beta \eta^* = 2V^* + \frac{\eta^*}{3V^*}. \quad (6-22)$$

Substituting Eq. (6-3) into Eq. (6-22) yields

$$v_3^* = 2V^* + \frac{0.42}{V^* \sqrt{A^*}}. \quad (6-23)$$

Fig. 6-12 shows the horizontal distribution of the vertical velocity at different sections along the liquid ligament axis for the case $A^* = 4.8\pi^3$ at $t^* = 4.31$ under the formation of a steady flow. The vertical velocity distributions were almost uniform across any section along the ligament axis. The central velocity increased with the height by the action of upward inertial force, resulting in an upward shrinking shape for the ligament.

The velocity v_3^* is analogous to the emanating velocity at the orifice injector exit, from which a liquid ligament emanates downward under gravity. Equations (6-3)

and (6-23) indicate that $y_3^* \rightarrow y_4^*$ and $v_3^* \rightarrow 2V^*$ as $A^* \rightarrow \infty$. Thus, at a relatively large acceleration, the artificial crest top of the bulk liquid layer can be considered as the orifice injector exit, at which the emanating velocity is $2V^*$.

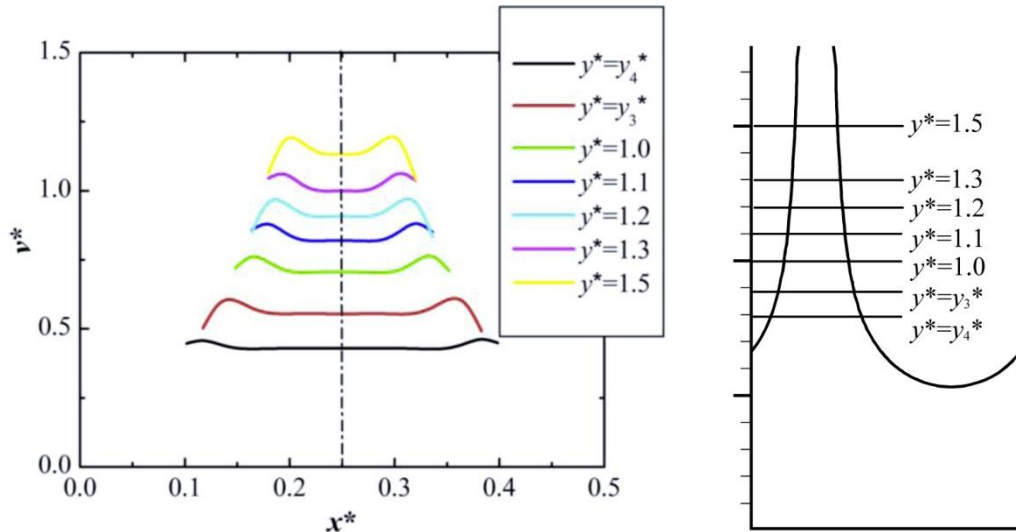


Fig. 6-12 Horizontal distribution of the vertical velocity at different sections along the liquid ligament axis for the case $A^* = 4.8\pi^3$ at $t^* = 4.31$.

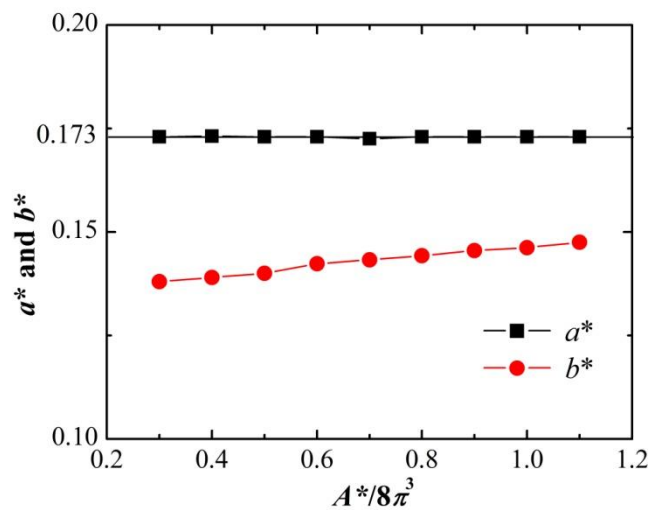


Fig. 6-13 Dependences of liquid ligament half width b^* at the maximum pressure location y_4^* and the liquid half width a^* at the artificial crest top y_3^* on the dimensionless parameter A^* .

Fig. 6-13 shows the dependences of the liquid ligament half width b^* at the maximum pressure location y_3^* and the half width a^* at the artificial crest top y_4^* on the dimensionless parameter A^* . The liquid half width a^* retained a constant value of $c_3 = 0.173$, independent of A^* . On the other hand, the liquid ligament half width b^*

increased with A^* . If A^* is sufficiently large, such that $y_3^* \rightarrow y_4^*$, then

$$b^* \rightarrow a^* = c_3 = 0.173 \quad (6-24)$$

as expected.

6.4 Laboratory low-speed jet experiments bridged to the ligament disintegration due to RT instability

Given the velocity and the ligament width at the maximum pressure location, the theory on low-speed jet development and breakup from an orifice injector can be extended to a ligament formed from a liquid layer due to a single-mode RT instability. In this section, based on the calculation results presented in §6.3, we bridged the laboratory low-speed jet experiments to the ligament disintegration due to RT instability.

From the growth rate expression Eq. (2-1), the wavelength of the surface mode of the maximum growth rate can be derived as

$$\lambda_m = 2\pi \sqrt{\frac{3\sigma}{\rho_1 A}}. \quad (6-25)$$

For a random initial disturbance containing all surface wave modes, the surface wave of wavelength λ_m is selected to grow dominantly to form a ligament from which droplets are generated. Corresponding to this surface wave of the maximum growth rate, the Weber and Bond numbers of the laboratory low-speed jet experiments (from an orifice injector) mimicking the ligament disintegration due to RT instability can be evaluated using Eqs. (6-4), (6-24), and (6-25) as

$$\text{We} = \frac{\rho_1 (2V)^2 b}{\sigma} = \frac{\rho_1 A \lambda_m^2}{\sigma} \cdot 4c_2^2 c_3 = 48\pi^2 c_2^2 c_3 = 4.149, \quad (6-26)$$

and

$$\text{Bo} = \frac{\rho_1 A b^2}{\sigma} = \frac{\rho_1 A \lambda_m^2}{\sigma} \cdot c_3^2 = 12\pi^2 c_3^2 = 3.545. \quad (6-27)$$

That is to say, in principle, the conclusions derived from the low-speed jet experiments with $\text{We} = 4.149$ and $\text{Bo} = 3.545$ can be applied to the ligament disintegration due to RT instability. The Weber number $\text{We} = 4.149$ was within the expected range

observed in laboratory low-speed jet experiments; however, the Bond number $Bo = 3.545$ was larger than typical experimental range. **Schulkes (1994)** has numerical studied the effects of Bond number (ranging up to $Bo = 10$) on the dynamics of jet disintegration from an orifice. Compared with the case for the small Bond number ($Bo < 1$), the slender liquid bridge connecting the bulbous tip and the orifice is much longer for the large Bond number ($Bo > 4$).

Chapter 7

Conclusion

In this dissertation, we numerically investigated the interfacial instability of a liquid layer arisen by a time-dependent (sinusoidal) and a constant inertial force, which are referred to as the “Faraday instability” and “Rayleigh-Taylor instability”, respectively. Either of the instability is able to form a large slender ligament on the liquid surface, which disintegrates into drops. We believe that the study in this dissertation is useful for understanding the basic mechanism of liquid atomization and constructing a physical model for more complicated turbulent atomization system. The major conclusions are as follows.

First, we studied the underlying mechanism of the ligament formation due to the Faraday instability, with the focus on how the liquid ligament connecting to the liquid layer can be dynamically free from the motion of substrate. The flow associated with the periodic surface deformation is restricted to a finite thickness ($\sim 1/k$) of liquid layer near the surface. When the surface deformation is small, its amplification is caused by the liquid flow from the trough portion to the crest portion due to the linear stagnation-point flow at the crest root formed during the destabilizing phase. Nonlinearity dominates gradually as the surface deformation increases. Correspondingly, the linear stagnation-point flow at the crest root is changed to the nonlinear stagnation-point flow. The pressure enhancement caused by the nonlinear stagnation-point flow brings about a local maximum pressure location at the root of the long ligament in which the pressure relaxes to be consistent with the surrounding uniform gas pressure. Therefore, the liquid ligament above the maximum pressure location is dynamically free from the bottom vibrating substrate in the laboratory reference frame. The liquid elements continuously passing through the maximum pressure location elongate the freed liquid region and result in a slender ligament.

Second, we proposed a numerical approach for determining the threshold condition for spray formation by a Faraday instability. To eliminate the side-wall effects and focus on the behavior of the predominant surface wave, we utilized a cell model spanning one surface wavelength horizontally, with a cyclic boundary condition imposed at left and right sides. We identified the predominant surface wave number

for each forcing strength on the instability chart for the Mathieu equation. This enabled us to determine the threshold condition for spray formation by numerically examining the nonlinear evolutions of the predominant surface waves on the straight line $Y = X/3$. Each calculation was initiated by a small disturbance imposed on the liquid surface. The criterion for spray formation is defined as the condition that a broken drop holds a null area-averaged vertical velocity in the laboratory reference frame. The findings are as follows. Consistent with the previous experimental observations, spray is formed from the sub-harmonically oscillating surface. The critical dimensionless forcing strength obtained from the present study is $\beta_c = 0.763 \sim O(1)$. In the case of $\beta < \beta_c$, no spray is formed. After the rapid amplification of the surface deformation at the early development, a standing-wave state is eventually achieved due to the phase difference between the inertial force and the surface deformation. In the case of $\beta > \beta_c$, spray is formed and the drop formation rate increases with β . The spray formation aroused by a Faraday instability is a process that the liquid layer absorbs energy from the inertial force and then releases it partially by producing drops leaving the liquid layer. Therefore, for the case of $\beta < \beta_c$, a large initial surface deformation, which provides a large amount of initial energy, may result in a single drop formation; however, no steady atomization state is realized for this case. The predominant surface wavelength of the sub-harmonically oscillating surface identified in this paper (*i.e.*, $Y = X/3$) is close to the resonant surface wavelength $2\pi(\sigma/\rho_1)^{1/3}(\Omega/2)^{-2/3}$. This is consistent with the experimental observation of the mean drop diameter in the ultrasonic atomization, which satisfies Lang's equation (**Lang, 1962**).

Third, we analyzed the single-mode RT instability for a large Atwood number, focusing on its detailed nonlinear dynamics during the late development stage of a liquid ligament emanating from a liquid layer. Driven by an inertial force, the impinging liquid flow in the ligament root region creates a localized pressure maximum that frees the bulk liquid layer from the long ligament. The impinging flow in the ligament root region eventually reaches a steady state due to the balance between the effective inertial force and the reverse pressure gradient. We studied the characteristic surface deformation quantities associated with this steady state to identify the laboratory low-speed jet experiments with the liquid ligament formed due to the RT instability. The main findings from this study are as follows. The liquid trough surface

had a sinusoidal shape of amplitude δ_0 , which was only dependent on the wavelength λ of the initial disturbance. This liquid trough surface, along with the maximum pressure location, identified as the orifice injector exit, moved downward at a constant V proportional to the square root of the product of the inertial acceleration A and the wavelength λ . The velocity and half width of the liquid entering the freed liquid ligament at the maximum pressure location, corresponding to the jet emanating velocity and orifice radius, respectively, were determined. These characteristic quantities bridge the knowledge between low-speed jet disintegration and behavior of a liquid ligament formed by an RT instability.

In the future studies, we will consider the effects of more characteristic parameters, such as the Reynolds number, capillary number, *etc.*, on the Faraday instability or RT instability. As an extension of this study, three-dimensional consideration is also an interesting problem. More importantly, if the capacity of the computer allows, simulating the entire system that includes all feasible surface wave modes is instructive for disclosing the underlying physics of liquid atomization.

Reference

- Al-Sueimani, Y., Collins, A., Yule, A., 1999. How orderly is ultrasonic atomization. Proc. of ILASS-Europe99.
- Al-Suleimani, Y., Yule, A.J., 2002. A CFD Prediction of Wave Development and Droplet Production on Surface Under Ultrasonic Excitation. Zaragoza 9, 11.
- Alon, U., Hecht, J., Ofer, D., Shvarts, D., 1995. Power laws and similarity of Rayleigh-Taylor and Richtmyer-Meshkov mixing fronts at all density ratios. Phys. Rev. Lett. 74, 534-537.
- Andrews, M.J., Dalziel, S.B., 2010. Small Atwood number Rayleigh-Taylor experiments. Philos. T. Roy. Soc. A 368, 1663-1679.
- Aranson, I.S., Kramer, L., 2002. The world of the complex Ginzburg-Landau equation. Rev. Mod. Phys. 74, 99.
- Arnett, W.D., Bahcall, J.N., Kirshner, R.P., Woosley, S.E., 1989. Supernova 1987A. Annu. Rev. Astro. Astrophys. 27, 629-700.
- Ashgriz, N., Poo, J., 1991. FLAIR: Flux line-segment model for advection and interface reconstruction. J. Comput. Phys. 93, 449-468.
- Baker, G., Verdon, C., McCrory, R., Orszag, S., 1987. Rayleigh-Taylor instability of fluid layers. J. Fluid Mech. 178, 161-175.
- Baker, G.R., Meiron, D.I., Orszag, S.A., 1980. Vortex simulations of the Rayleigh-Taylor instability. Phys. Fluids 23, 1485-1490.
- Banerjee, A., Kraft, W.N., Andrews, M.J., 2010. Detailed measurements of a statistically steady Rayleigh-Taylor mixing layer from small to high Atwood numbers. J. Fluid Mech. 659, 127-190.
- Beale, J.C., Reitz, R.D., 1999. Modeling spray atomization with the Kelvin-Helmholtz /Rayleigh-Taylor hybrid model. Atomization Sprays 9, 623-650.
- Bell, J.B., Dawson, C.N., Shubin, G.R., 1988. An unsplit, higher order Godunov method for scalar conservation laws in multiple dimensions. J. Comput. Phys. 74, 1-24.
- Bellman, R., Pennington, R.H., 1954. Effects of surface tension and viscosity on Taylor instability. Quart. J. Appl. Math. 12, 151.
- Benjamin, T.B., Ursell, F., 1954. The stability of the plane free surface of a liquid in vertical periodic motion. Proc. R. Soc. London, Ser. A 225, 505-515.
- Birkhoff, G., Carter, D., 1957. Rising plane bubbles. J. Math. Mech. 6.
- Brackbill, J., Kothe, D.B., Zemach, C., 1992. A continuum method for modeling surface tension. J. Comput. Phys. 100, 335-354.
- Chen, P., 2002. Nonlinear wave dynamics in Faraday instabilities. Phys. Rev. E 65, 036308.
- Chen, P., Viñals, J., 1997. Pattern selection in Faraday waves. Phys. Rev. Lett. 79, 2670.
- Chen, P., Vinals, J., 1999. Amplitude equation and pattern selection in Faraday waves. Phys. Rev. E 60, 559.
- Dalziel, S., Linden, P., Youngs, D., 1999. Self-similarity and internal structure of turbulence induced by Rayleigh-Taylor instability. J. Fluid Mech. 399, 1-48.
- Dimonte, G., Ramaprabhu, P., Youngs, D., Andrews, M., Rosner, R., 2005. Recent advances in the turbulent Rayleigh-Taylor instability. Phys. Plasmas 12, 056301.
- Donnelly, T., Hogan, J., Mugler, A., Schommer, N., Schubmehl, M., Bernoff, A.J., Forrest, B., 2004.

An experimental study of micron-scale droplet aerosols produced via ultrasonic atomization. *Phys. Fluids* 16, 2843.

Eggers, J., 1997. Nonlinear dynamics and breakup of free-surface flows. *Rev. Mod. Phys.* 69, 865.

Eggers, J., Villermaux, E., 2008. Physics of liquid jets. *Rep. Prog. Phys.* 71, 036601.

Eisenmenger, W., 1959. Dynamic properties of the surface tension of water and aqueous solutions of surface active agents with standing capillary waves in the frequency range from 10 kc/s to 1.5 Mc/s. *Acustica* 9, 327-340.

Evans, R., Bennett, A., Pert, G., 1982. Rayleigh-Taylor instabilities in laser-accelerated targets. *Phys. Rev. Lett.* 49, 1639-1642.

Faraday, M., 1831. On a peculiar class of acoustical figures; and on certain forms assumed by groups of particles upon vibrating elastic surfaces. *Philos. Trans. R. Soc. London* 121, 299-340.

Garabedian, P., 1957. On steady-state bubbles generated by Taylor instability. *Proc. R. Soc. Lon. Ser. A* 241, 423-431.

Garrioch, S., Baliga, B., 2006. A PLIC volume tracking method for the simulation of two - fluid flows. *Int. J. Numer. Meth. Fl.* 52, 1093-1134.

Glimm, J., McBryan, O., Menikoff, R., Sharp, D., 1986. Front tracking applied to Rayleigh-Taylor instability. *SIAM J. Sci. Stat. Comp.* 7, 230-251.

Goncharov, V., 2002. Analytical model of nonlinear, single-mode, classical Rayleigh-Taylor instability at arbitrary Atwood numbers. *Phys. Revi. Lett.* 88, 134502.

Goodridge, C., Hentschel, H., Lathrop, D., 1999. Breaking Faraday waves: critical slowing of droplet ejection rates. *Phys. Rev. Lett.* 82, 3062-3065.

Goodridge, C.L., Shi, W.T., Hentschel, H., Lathrop, D.P., 1997. Viscous effects in droplet-ejecting capillary waves. *Phys. Rev. E* 56, 472.

Goodridge, C.L., Shi, W.T., Lathrop, D.P., 1996. Threshold dynamics of singular gravity-capillary waves. *Phys. Rev. Lett.* 76, 1824-1827.

Harlow, F.H., Welch, J.E., 1965. Numerical Calculation of Time - Dependent Viscous Incompressible Flow of Fluid with Free Surface. *Phys. Fluids* 8, 2182-2189.

Hirt, C.W., Nichols, B.D., 1981. Volume of fluid (VOF) method for the dynamics of free boundaries. *J. Comput. Phys.* 39, 201-225.

James, A., Vukasinovic, B., Smith, M.K., Glezer, A., 2003a. Vibration-induced drop atomization and bursting. *J. Fluid Mech.* 476, 1-28.

James, A.J., Smith, M.K., Glezer, A., 2003b. Vibration-induced drop atomization and the numerical simulation of low-frequency single-droplet ejection. *J. Fluid Mech.* 476, 29-62.

Josserand, C., Zaleski, S., 2003. Droplet splashing on a thin liquid film. *Phys. Fluids* 15, 1650.

Kelvin, L., 1871. XLVI. Hydrokinetic solutions and observations. *Phil. Mag.* 42, 362-377.

Kityk, A., Embs, J., Mekhonoshin, V., Wagner, C., 2005. Spatiotemporal characterization of interfacial Faraday waves by means of a light absorption technique. *Phys. Rev. E* 72, 036209.

Kong, S., Senecal, P., Reitz, R., 1999. Developments in spray modeling in diesel and direct-injection gasoline engines. *Oil Gas Sci. Technol.* 54, 197-204.

Kudrolli, A., Gollub, J., 1996. Patterns and spatiotemporal chaos in parametrically forced surface waves: a systematic survey at large aspect ratio. *Physica D* 97, 133-154.

Kumar, K., 1996. Linear theory of Faraday instability in viscous liquids. *Proc. R. Soc. London, Ser. A* 452, 1113-1126.

Kumar, K., Tuckerman, L.S., 1994. Parametric instability of the interface between two fluids. *J.*

- Fluid Mech. 279, 49-68.
- Kumar, S., Matar, O.K., 2004. On the Faraday instability in a surfactant-covered liquid. *Phys. Fluids* 16, 39.
- Lang, R.J., 1962. Ultrasonic atomization of liquids. *J. Acoust. Soc. Am.* 34, 6.
- Layzer, D., 1955. On the Instability of Superposed Fluids in a Gravitational Field. *Astrophys. J.* 122, 1-12.
- Lewis, D., 1950. The instability of liquid surfaces when accelerated in a direction perpendicular to their planes. II. *Proc. R. Soc. Lon. Ser. A* 202, 81-96.
- Lin, S.-P., 2003. Breakup of liquid sheets and jets. Cambridge University Press New York.
- Lindl, J.D., McCrory, R.L., Campbell, E.M., 1992. Progress toward ignition and burn propagation in inertial confinement fusion. *Phys. Today* 45, 32-40.
- Müller, H.W., 1994. Model equations for two-dimensional quasipatterns. *Phys. Rev. E* 49, 1273-1277.
- Ménard, T., Tanguy, S., Berlemont, A., 2007. Coupling level set/VOF/ghost fluid methods: Validation and application to 3D simulation of the primary break-up of a liquid jet. *Int. J. Multiphase Flow* 33, 510-524.
- Mancebo, F.J., Vega, J.M., 2006. Viscous Faraday waves in two-dimensional large-aspect-ratio containers. *J. Fluid Mech.* 560, 369-393.
- Miles, J., Henderson, D., 1990. Parametrically forced surface waves. *Annu. Rev. Fluid Mech.* 22, 143-165.
- Miles, J.W., 1967. Surface-wave damping in closed basins. *Proc. R. Soc. London, Ser. A* 297, 459-475.
- Murakami, Y., Chikano, M., 2001. Two-dimensional direct numerical simulation of parametrically excited surface waves in viscous fluid. *Phys. Fluids* 13, 65.
- Nichols, B., Hirt, C., Hotchkiss, R., 1980. SOLA-VOF: A solution algorithm for transient fluid flow with multiple free boundaries. Los Alamos Scientific Lab., NM (USA).
- Norman, M., Smarr, L., Smith, M., Wilson, J., 1981. Hydrodynamic formation of twin-exhaust jets. *Astrophys. J.* 247, 52-58.
- Oron, D., Arazi, L., Kartoon, D., Rikanati, A., Alon, U., Shvarts, D., 2001. Dimensionality dependence of the Rayleigh–Taylor and Richtmyer–Meshkov instability late-time scaling laws. *Phys. Plasmas* 8, 2883.
- Perinet, N., Juric, D., Tuckerman, L.S., 2009. Numerical simulation of Faraday waves. *J. Fluid Mech.* 635, 1-26.
- Pietschmann, D., Stannarius, R., Wagner, C., John, T., 2013. Faraday Waves under Time-Reversed Excitation. *Phys. Rev. Lett.* 110, 094503.
- Pilliod Jr, J.E., Puckett, E.G., 2004. Second-order accurate volume-of-fluid algorithms for tracking material interfaces. *J. Comput. Phys.* 199, 465-502.
- Piriz, A., Cortazar, O., Cela, J.L., Tahir, N., 2006. The rayleigh-taylor instability. *Am. J. phys.* 74, 1095-1098.
- Puthenveetil, B.A., Hopfinger, E., 2009. Evolution and breaking of parametrically forced capillary waves in a circular cylinder. *J. Fluid Mech.* 633, 355.
- Qi, A., Yeo, L.Y., Friend, J.R., 2008. Interfacial destabilization and atomization driven by surface acoustic waves. *Phys. Fluids* 20, 074103.
- Rajan, R., Pandit, A., 2001. Correlations to predict droplet size in ultrasonic atomisation.

Ultrasonics 39, 235-255.

Ramaprabhu, P., Andrews, M., 2004. Experimental investigation of Rayleigh-Taylor mixing at small Atwood numbers. *J. Fluid Mech.* 502, 233-271.

Ramaprabhu, P., Dimonte, G., 2005. Single-mode dynamics of the Rayleigh-Taylor instability at any density ratio. *Phys. Rev. E* 71, 036314.

Ramaprabhu, P., Dimonte, G., Andrews, M., 2005. A numerical study of the influence of initial perturbations on the turbulent Rayleigh-Taylor instability. *J. Fluid Mech.* 536, 285-320.

Ramaprabhu, P., Dimonte, G., Woodward, P., Fryer, C., Rockefeller, G., Muthuraman, K., Lin, P., Jayaraj, J., 2012. The late-time dynamics of the single-mode Rayleigh-Taylor instability. *Phys. Fluids* 24, 074107.

Ramaprabhu, P., Dimonte, G., Young, Y.-N., Calder, A., Fryxell, B., 2006. Limits of the potential flow approach to the single-mode Rayleigh-Taylor problem. *Phys. Rev. E* 74, 066308.

Rayleigh, L., 1883. Investigation of the character of the equilibrium of an incompressible heavy fluid of variable density. *Proc. London Math. Soc.* 14, 170-177.

Read, K., 1984. Experimental investigation of turbulent mixing by Rayleigh-Taylor instability. *Physica D* 12, 45-58.

Rider, W.J., Kothe, D.B., 1998. Reconstructing volume tracking. *J. Comput. Phys.* 141, 112-152.

Scardovelli, R., Zaleski, S., 1999. Direct numerical simulation of free-surface and interfacial flow. *Annu. Rev. Fluid Mech.* 31, 567-603.

Schulkes, R., 1994. The evolution and bifurcation of a pendant drop. *J. Fluid Mech.* 278, 83-100.

Sharp, D.H., 1984. An overview of Rayleigh-Taylor instability. *Physica D* 12, 3-18.

Shinjo, J., Umemura, A., 2010. Simulation of liquid jet primary breakup: Dynamics of ligament and droplet formation. *Int. J. Multiphase Flow* 36, 513-532.

Sohn, S.-I., 2003. Simple potential-flow model of Rayleigh-Taylor and Richtmyer-Meshkov instabilities for all density ratios. *Phys. Rev. E* 67, 026301.

Son, G., Hur, N., 2002. A coupled level set and volume-of-fluid method for the buoyancy-driven motion of fluid particles. *Numer. Heat Tr B-Fund.* 42, 523-542.

Stone, H.A., Bentley, B., Leal, L., 1986. An experimental study of transient effects in the breakup of viscous drops. *J. Fluid Mech.* 173, 131-158.

Stone, H.A., Leal, L., 1989. Relaxation and breakup of an initially extended drop in an otherwise quiescent fluid. *J. Fluid Mech.* 198, C55.

Sun, D., Tao, W., 2010. A coupled volume-of-fluid and level set (VOSET) method for computing incompressible two-phase flows. *Int. J. Heat Mass Tran.* 53, 645-655.

Sussman, M., 2003. A second order coupled level set and volume-of-fluid method for computing growth and collapse of vapor bubbles. *J. Comput. Phys.* 187, 110-136.

Sussman, M., Fatemi, E., 1999. An efficient, interface-preserving level set redistancing algorithm and its application to interfacial incompressible fluid flow. *SIAM J. Sci. Comput.* 20, 1165-1191.

Sussman, M., Puckett, E.G., 2000. A coupled level set and volume-of-fluid method for computing 3D and axisymmetric incompressible two-phase flows. *J. Comput. Phys.* 162, 301-337.

Sussman, M., Smereka, P., Osher, S., 1994. A level set approach for computing solutions to incompressible two-phase flow. Department of Mathematics, University of California, Los Angeles.

Takagi, K., Matsumoto, T., 2011. Numerical simulation of two-dimensional Faraday waves with phase-field modelling. *J. Fluid Mech.* 686, 409-425.

Tan, M.K., Friend, J.R., Matar, O.K., Yeo, L.Y., 2010. Capillary wave motion excited by high

frequency surface acoustic waves. *Phys. Fluids* 22, 112112.

Taylor, G.I., 1950. The instability of liquid surfaces when accelerated in a direction perpendicular to their planes. I. *Proc. R. Soc. London. Ser. A* 201, 192-196.

Tryggvason, G., Unverdi, S.O., 1990. Computations of three - dimensional Rayleigh–Taylor instability. *Phys. Fluids* 2, 656-659.

Tsai, S.C., Childs, P., Luu, P., 1996. Ultrasound - modulated two - fluid atomization of a water jet. *AIChE J.* 42, 3340-3350.

Tsai, S.C., Luu, P., Childs, P., Teshome, A., Tsai, C.S., 1997. The role of capillary waves in two-fluid atomization. *Phys. Fluids* 9, 2909-2918.

Ubal, S., Giavedoni, M., Saita, F., 2003. A numerical analysis of the influence of the liquid depth on two-dimensional Faraday waves. *Phys. Fluids* 15, 3099.

Umemura, A., 2011. Self-destabilizing mechanism of a laminar inviscid liquid jet issuing from a circular nozzle. *Phys. Rev. E* 83, 046307.

Van der Pijl, S., Segal, A., Vuik, C., Wesseling, P., 2005. A mass - conserving Level - Set method for modelling of multi - phase flows. *Int. J. Numer. Methods Fluids* 47, 339-361.

Vukasinovic, B., Smith, M.K., Glezer, A., 2004. Spray characterization during vibration-induced drop atomization. *Phys. Fluids* 16, 306.

Vukasinovic, B., Smith, M.K., Glezer, A., 2007. Mechanisms of free-surface breakup in vibration-induced liquid atomization. *Phys. Fluids* 19, 012104.

Waddell, J., Niederhaus, C., Jacobs, J., 2001. Experimental study of Rayleigh–Taylor instability: low Atwood number liquid systems with single-mode initial perturbations. *Phys. Fluids* 13, 1263-1273.

Westra, M.-T., Binks, D.J., Van De Water, W., 2003. Patterns of Faraday waves. *J. Fluid Mech.* 496, 1-32.

Wilkinson, J., Jacobs, J., 2007. Experimental study of the single-mode three-dimensional Rayleigh–Taylor instability. *Phys. Fluids* 19, 124102.

Wood, E., Loomis, A.L., 1927. XXXVIII. The physical and biological effects of high-frequency sound-waves of great intensity. *Phil. Mag.* 4, 417-436.

Wright, J., Yon, S., Pozrikidis, C., 2000. Numerical studies of two-dimensional Faraday oscillations of inviscid fluids. *J. Fluid Mech.* 402, 1-32.

Youngs, D.L., 1984. Numerical simulation of turbulent mixing by Rayleigh–Taylor instability. *Physica D* 12, 32-44.

Yule, A., Al–Suleimani, Y., 2000. On droplet formation from capillary waves on a vibrating surface. *Proc. R. Soc. London, Ser. A* 456, 1069-1085.

Zhang, W., Viñals, J., 1996. Square patterns and quasipatterns in weakly damped Faraday waves. *Phys. Rev. E* 53, R4283.

Zhang, W., Viñals, J., 1997a. Pattern formation in weakly damped parametric surface waves. *J. Fluid Mech.* 336, 301-330.

Zhang, W., Viñals, J., 1997b. Pattern formation in weakly damped parametric surface waves driven by two frequency components. *J. Fluid Mech.* 341, 225-244.

Zhang, W., Viñals, J., 1998. Numerical study of pattern formation in weakly damped parametric surface waves. *Physica D* 116, 225-243.

List of publications

Journal papers:

1. **Li, Y.***, Umemura, A., 2014. Two-dimensional numerical investigation on the dynamics of ligament formation by Faraday instability. *International Journal of Multiphase Flow* 60, 64-75.
2. **Li, Y.***, Umemura, A., 2014. Numerical study on the jet formation due to Rayleigh–Taylor instability. *Japanese Journal of Applied Physics* 53, 110302.
3. **Li, Y.***, Umemura, A., Mechanism of the large surface deformation caused by Rayleigh-Taylor instability at large Atwood number. *Journal of Applied Mathematics and Physics*. (**accepted**)
4. **Li, Y.***, Umemura, A., 2014. Threshold condition for spray formation by Faraday instability. *Journal of Fluid Mechanics* 759, 73-103.

International conference papers:

1. **Li, Y.***, Umemura, A., 2013. Pre-investigation on the spray combustion: numerical simulations of the atomization from the vertically vibrating liquid layer. 9th Asia-Pacific Conference on Combustion, Gyeongju, Korea.
2. **Li, Y.***, Umemura, A., 2011. Two-dimensional numerical simulation on jet surface capillary waves arising from downstream oscillation and bottom disturbance. ICAMAME 2011, Paris, France.